Applications of Nondestructive Testing in Civil Engineering

by

Paul Groves

A thesis
presented to the University of Waterloo
in fulfillment of the
thesis requirement for the degree of
Master of Applied Science
in
Civil Engineering

Waterloo, Ontario, Canada, 2010

ABSTRACT

Presented in this thesis are two studies that apply nondestructive testing methods to civil engineering problems. The first study examines the relationship between the small-strain and large-strain properties of exhumed cast iron water pipes. Nondestructive and destructive testing programs were performed on eight pipes varying in age from 40 to 130 years. The experimental program included microstructure evaluation and ultrasonic, tensile, and flexural testing. Correlations between small strain and large strain properties of the tested cast iron pipes are examined. New applications of frequency domain analysis techniques including Fourier and wavelet transforms of ultrasonic pulse velocity measurements are presented. The effects of Lamb wave propagation on the ultrasonic testing results are investigated.

Microstructure evaluation revealed two different types of cast iron within the pipes sampled: grey cast iron and ductile iron. A low correlation between wave propagation and large-strain measurements was observed. However, the wave velocities were consistently different between ductile and grey cast iron pipes (14% to 18% difference); the ductile iron pipes showed the smaller variation in wave velocities. Thus, the variation of elastic properties for ductile iron was not sufficient to define a linear correlation because all the measurements which were practically concentrated in single cluster of points. The cross-sectional areas of the specimens tested varied as a result of minor manufacturing defects and different levels of corrosion. These variations affect the large strain testing results but surface defects have limited effect on wave velocities and may also contribute to the low correlations observed. Lamb waves were found to contribute significantly to the frequency content of the ultrasonic signals possibly resulting in the poor correlations observed. Therefore, correlations between wave velocities and large strain properties obtained using samples from exhumed water pipes must be used with caution in the condition assessment of aged water pipes especially for grey cast iron pipes.

The second study presented in this thesis was performed to evaluate the effectiveness of three geophysical methods for geotechnical site characterization in swamps and environmentally sensitive wetland areas. The geophysical methods evaluated were electrical resistivity imaging (ERI), seismic refraction (SR), and multiple-channel analysis of surface waves (MASW). The geophysical test results were verified against the results from borehole and CPT logs. Available geotechnical studies for the test area suggested the presence of soft compressible soils underlain by hard glacial till. The boreholes advanced after the geophysical investigation revealed three soil layers overlying a refusal layer of glacial till. A layer stiffness reversal was observed in the strata overlying the till in that a more competent sand layer was found overlying a less competent clay layer.

The ERI results were best for determining the depth to the glacial till. However, the resolution of the ERI survey was not sufficient to accurately predict the upper lithologies. The electrode spacing (4-m) was instead selected to reliably predict the depth to the till which in this case varied between 4.6 and 10.7 m. The SR results overestimated the depth to the till because of the presence of a stiffness reversal. The MASW results predicted the depth to the refusal till layer less accurately than the ERI method. However, this method was able to detect the three distinct layers above the till, even though the layer thicknesses were consistently underestimated. The complementary use of geophysical techniques was a successful approach in determining the main soil units and the depth to the competent layer (till) at the site. These methods can be used as a basis for further development to optimize a procedure to reduce the number of boreholes required for conventional site investigations in areas that are environmentally sensitive or where access is restricted.

ACKNOWLEDGEMENTS

First and foremost I would like to thank Dr. Giovanni Cascante for his continuous guidance, support, valuable insights, and encouragement. The time and effort he spent throughout this project's entirety have contributed significantly to its success and completion and will be forever appreciated.

With specific reference to the ultrasonic study, I would like to thank Dr. Mark Knight for his assistance in preparing samples and guidance during the mechanical testing of the cast iron pipes. I would like to acknowledge the contribution of the City of Hamilton for providing the pipe and historical records of these pipes; Prof. Tim Topper for thoughtful discussions on the evaluation of the large strain testing; Douglas Hirst, Richard Morrison, Atif Nazir, Awais Rauf and Antonin Du Tertre for their help with the experimental program. Gratitude also goes to Natural Sciences and Engineering Research Council of Canada (NSERC), and the Centre for Advancement of Trenchless Technologies (CATT) at the University of Waterloo for the funding and in-kind contributions for this research.

In reference to the geophysical study, I would like to thank Dave Dundas of the Ministry of Transport Ontario and P. K. Chatterji of Thurber Engineering for their help with revisions of the geophysics study presented in Chapter 6. I would like to acknowledge the contribution of the Ministry of Transportation of Ontario (MTO) for the permission to perform the geophysical tests, Zahid Khan for the revision and evaluation of the results, Thurber Engineering Ltd. And Soheil Moayerian for the field support during the measurements, Geostudi Astier S.r.l. for the permission to use the program SWAN for the inversion of surface waves, and Fernando Tallavo, Yanjun Yang, Soheil Moayerian, Peter Pehme, and Chris Phillips for their help with the experimental program and data processing. Our gratitude also goes to Natural Sciences and Engineering Research Council of Canada (NSERC), OCE-Centre for Earth and Environmental Technologies, and Waterloo-Geophysics Inc. for the funding and in-kind contributions for this research.

I would also like to thank Dr. Mahesh Pandey and Dr. Lei Xu for taking time to review my work and providing insightful comments and suggesting revisions that helped improve the quality of the final version of this thesis.

TABLE OF CONTENTS

LIST OF TABLES

LIST OF FIGURES

CHAPTER 1: INTRODUCTION

1.1 Background

Nondestructive testing uses the propagation behaviour of different types of waves in the evaluation of the internal structure of materials. For example, ultrasonic waves can be used for the condition assessment of cast iron and electromagnetic, electric, and seismic waves can be used for geotechnical investigation of subsurface soils. The scale of such tests depends on the wavelength of the applied energy; ultrasonic testing uses high frequency elastic waves with millimeter wavelengths while large scale seismic studies used in oil exploration uses waves with kilometer lengths. Continuing technological developments in data collection and acquisition equipment and interpretation techniques have provided useful applications of nondestructive methods in many engineering fields. This thesis examines two separate applications of nondestructive testing in civil engineering: the ultrasonic characterization of exhumed cast iron water pipes and the use of geophysical methods for soil profile evaluation.

Cast iron pipe has been used as a water distribution technology in North America since the early nineteenth century. The first cast iron pipes were made of grey cast iron which was succeeded by ductile iron as a pipe material in the 1940s (Bilgin and Stewart 2009). These different iron alloys have significantly different microstructures which give rise to distinct mechanical properties. Insight into the nondestructive structural condition assessment of aging pipes can be advantageous in developing mitigation strategies for pipe failures. The first study presented in this thesis examines the relationship between the small-strain and large-strain properties of exhumed cast iron water pipes through ultrasonic, tensile, and flexural testing.

Geophysical methods are nondestructive techniques that use the physical properties of earth materials to infer subsurface structure. Changes in stratigraphy and lithology are mapped through measurements from the surface. Not only can geophysical methods reduce the number of expensive boreholes required for site investigations, but they can provide detailed information of the subsurface between boreholes. The second study presented in this thesis involved a geophysical investigation performed to evaluate the effectiveness of three geophysical methods for geotechnical site characterization of shallow soils in swamps and environmentally sensitive wetland areas. The geophysical methods evaluated were electrical resistivity imaging (ERI), seismic refraction (SR), and multiple-channel analysis of surface waves (MASW).

1.2 Objectives and Scope

The overall goal of this thesis research is to investigate two potential applications of nondestructive testing in the practice of Civil Engineering. The primary objective of the cast iron water pipe study was to evaluate relationship between the small-strain and large-strain mechanical properties of cast iron water pipes. Although previous studies of exhumed cast iron pipes exist in the literature, these studies do not use ultrasonic testing as one of their principal investigation tools. Nondestructive and destructive testing programs were performed on eight exhumed pipes varying in age from 40 to 130 years. The experimental program included microstructure evaluation and ultrasonic, tensile, and flexural testing. New applications of frequency domain analysis techniques including Fourier and wavelet transforms of ultrasonic pulse velocity measurements are presented. Furthermore, the effects of Lamb wave propagation on the ultrasonic testing results are investigated.

The primary objective of the geophysical investigation was to evaluate the effectiveness of three geophysical methods for geotechnical site characterization in a unique environment. The study-site was located in a wetland area with difficult access for conventional drilling equipment because of soft, clay-rich soils. Available geotechnical studies for the test area suggested the presence of soft compressible soils underlain by hard glacial till. Furthermore, a layer stiffness reversal was observed in the strata providing a unique setting to evaluate the complementary use of these methods. ERI, SR, and MASW surveys were performed on two lines. The data gathered from each method were analyzed and interpreted independently. The geophysical test results were verified against the results from borehole and cone penetrometer test logs advanced after the geophysical surveys.

1.3 Thesis Organization

The opening chapter of this thesis provides an introduction to the studies presented in this thesis. Chapter 2 gives an introduction to waves in elastic media and provides basic theory upon which some of the nondestructive testing methods used in this study are founded. Chapter 3 introduces the four nondestructive testing methods used in this study. Detailed explanations of the application, interpretation of results, and limitations of these methods are discussed. Chapter 4 provides a review of the literature including summaries of studies that present information applicable to the investigations completed for this thesis. Chapter 5 presents the first study performed for this thesis: Ultrasonic Characterization of Exhumed Cast Iron Water Pipes. Chapter 6 presents the second study performed for this thesis: Use of Geophysical Methods for Soil Profile Evaluation. Finally, Chapter 7 provides conclusions drawn from both studies and an outline of future work.

CHAPTER 2: INTRODUCTION TO ELASTIC WAVES

2.1 Background

Elastic waves are used in numerous nondestructive testing methods. Some of these include ultrasonic testing, seismic refraction and reflection surveying, and multiple channel analysis of surface waves. Such techniques use the analysis of different elastic wave properties to provide information on the internal characteristics of the medium through measurements at the surface of the material.

When an impact occurs on an elastic medium, a wave train of different elastic waves is generated that propagates outwards from this source. Characteristics of wave propagation depend on the specific type of wave and the properties of the medium through which it travels. One of the most commonly used elastic wave properties is velocity. The velocity (V), frequency (f), and wavelength (λ) of any wave are related according to

$$V = f\,\lambda \qquad [2.1]$$

Velocity is constant in a homogeneous medium. Wave velocity is generally greater in relatively stiffer materials. Eq. 2.1 indicates that frequency is inversely proportional to wavelength; within the same material, high frequency waves have smaller wavelengths than low frequency waves. High frequencies waves have less energy than lower frequency waves and therefore do not travel as far in a medium because they attenuate faster. In general, high frequencies travel further in relatively stiffer materials because such materials have lesser damping effects than softer materials.

There are two principal groups of elastic waves: body waves and surface waves.

2.2 Body Waves

Body waves travel through the internal volume of an elastic medium. These waves propagate outwards from a source in a semi-spherical wavefront. The general wave velocity (V) formula for body waves in a homogeneous, isotropic material is given by

$$V = \sqrt{\frac{\text{applicable elastic modulus of material}}{\text{mass density of material}}} \qquad [2.2]$$

Body waves are non-dispersive, meaning that all frequency components of body waves travel through a homogeneous medium with the same velocity depending only on the properties of the medium (Keary et al. 2002).

There are two types of body waves: p-waves (also known as primary, compressional, or longitudinal waves) and s-waves (also known as secondary, shear, or transverse waves). These types are distinguished primarily by the different nature of particle motion they induce.

2.2.1 Primary Waves

P-waves propagate through the uniaxial compression and dilation of a medium resulting in changes in volume with no rotation. The resulting particle motion is oscillatory and in the same direction as the wave propagation as shown in Figure 2.1. P-wave velocity (V_P) in a homogeneous medium is given by (Graph 1991)

$$V_P = \sqrt{\frac{M}{\rho}} \qquad [2.3]$$

where M is the constrained modulus and ρ is the mass density. The constrained modulus is related to elastic modulus (E) according to (Graph 1991)

$$M = E\left[\frac{1-\nu}{(1+\nu)(1-2\nu)}\right] \qquad [2.4]$$

where υ is the Poisson’s ratio. P-waves are the fastest elastic waves and are therefore the first detected in applications such as ultrasonic testing and seismic reflection or refraction surveying. It has been estimated that about 7 % of the energy in a wavefront generated by a point source in a solid material is p-wave energy (Miller and Pursey 1955).

2.2.2 Secondary Waves

S-waves propagation consists of pure shear strain with no change in volume. The resulting particle motion is oscillatory in a direction perpendicular (transverse) to that of the wave propagation as shown in Figure 2.1. S-wave velocity (V_S) in a homogeneous medium is given by (Graph 1991)

$$V_S = \sqrt{\frac{G}{\rho}} \qquad [2.5]$$

where G is the shear modulus. S-waves do no propagate through liquids and gasses because these materials have no shear strength. The ratio of p-wave velocity to s-wave velocity is given by (Keary et al. 2002)

$$V_P / V_S = \sqrt{\frac{2(1-\nu)}{(1-2\nu)}} \qquad [2.6]$$

Considering a Poisson's ratio of 0.25, V_S is approximately $0.59V_P$ in a homogeneous medium. As a result, s-waves generally have smaller wavelengths than p-waves. Approximately 26 % of the energy in a wavefront travelling through a semi-infinite medium is s-wave energy (Miller and Pursey 1955).

2.3 Surface Waves

Surface waves are confined to the surface of an elastic medium. In a material with vertical velocity variation, individual frequency components making up a surface wave have different velocities called phase velocities. The result is a different wavelength for each frequency component making up the surface wave. This phenomenon is called dispersion (Penumada and Park 2005). The most commonly discussed surface waves are Rayleigh waves (R-waves). Another type of surface wave specific to media with two free surfaces is the Lamb wave.

2.3.1 Rayleigh Waves

R-waves are formed by the interaction of body waves at the free surface of a half space (Yang et al. 2009). These waves propagate outwards from a source in a cylindrical wavefront with a central axis passing through the source location and oriented perpendicular to the surface. The near surface particle motion associated with R-waves is a retrograde elliptical orbit in a plane perpendicular to the free surface as shown in Figure 2.1. The effective depth of penetration is commonly taken as one wavelength, with most of the energy concentrated between the surface and a depth of 1/3 λ (Lai and Wilmanski 2005).

The R-wave horizontal (u_x) and vertical (u_z) particle displacements are given by (Victorov, I. A. 1967)

$$u_x(x,z,t,\omega,k) = Ai\left(ke^{-\alpha z} - \frac{\beta^2 + k^2}{2k}e^{-\beta z}\right)e^{i(kx-\omega t)}$$

$$u_z(x,z,t,\omega,k) = A\left(-\alpha e^{-\alpha z} + \frac{\beta^2 + k^2}{2\beta}e^{-\beta z}\right)e^{i(kx-\omega t)} \qquad [2.7]$$

where $\alpha = \sqrt{k^2 - (\omega/V_P)^2}$, $\beta = \sqrt{k^2 - (\omega/V_S)^2}$, A is a constant, i is the imaginary unit, x is the horizontal distance from source, z is vertical distance from source, t is time, ω is the angular frequency ($\omega = 2\pi f$) and k is the angular wave number ($k = 2\pi/\lambda$). Figure 2.2 illustrates the change in horizontal and vertical displacements with depth according to Eq. 2.7 for different Poission's ratios. Positive vertical displacements and negative horizontal displacements near the surface result in retrograde elliptical particle motion. The motion is reversed as the horizontal displacements become positive with depth.

R-waves are non-dispersive in homogeneous media. The velocity of R-waves (V_R) in a homogeneous medium can be approximated as a function of V_S and the Poisson's ratio (ν) of the material by (Graff 1991)

$$V_R \approx \frac{0.874 + 1.117\nu}{1+\nu} V_S \qquad [2.8]$$

For ν ranging from 0 to 0.5, equation 5 indicates that V_R is approximately 0.87 to 0.96 times V_S. Approximately two thirds of the energy composing an elastic wavefront following a surface occurs as R-waves (Penumadu and Park 2005).

R-waves are dispersive in layered media. High frequencies (short λ) have limited penetration and propagate at the velocity of upper layers, whereas lower frequencies (larger λ) penetrate deeper and propagate at velocities determined by the characteristics of subsequently deeper soil layers (Lai and Wilmanski 2005) as seen in Figure 2.3. The different velocities of the varying frequency components of surface wave energy are called phase velocities. A dispersion curve shows phase velocity as a function of frequency as shown in Figure 2.4. The solution of fundamental R-wave propagation equations for layered media has no closed-from solution; evaluation of integrals is necessary to establish the theoretical dispersion curve for a specific layered material.

Surface waves have multiple modes of propagation. The fundamental mode is important because its maximum particle displacement occurs near-surface and can therefore be measured with transducers at the ground level. Higher modes could have maximum particle displacements in deeper layers. A sketch of the variation of the particle displacement with depth for the fundamental and first mode is presented in Figure 2.5. The shape of the second mode is given for illustration purposes only because its actual shape is a function of the specific soil profile. Higher modes have greater velocities of propagation than lower modes.

2.3.2 Lamb Waves

In a medium with two free surfaces (a plate) thin enough to allow penetration to the second surface (H ~ 1λ, where H is thickness), R-waves degenerate to Lamb waves. These waves have symmetrical and anti-symmetrical mode shapes of propagation as shown in Figure 2.6; with respect to a plane at the middle thickness of a plate, symmetric Lamb modes generate waves with symmetric thickness variation, and anti-symmetric

Lamb modes generate waves with anti-symmetric thickness variation (Yang et. al 2009). The fundamental mode is the most important because it spans all frequencies and carries more energy than higher modes (Blitz and Simpson 1996). Being surface waves, Lamb waves are dispersive. The wave propagation of Lamb modes is governed by the Rayleigh-Lamb-frequency equation (Graff 1991):

$$\frac{\tanh(\beta h)}{\tanh(\alpha h)}+\left[\frac{4\alpha\beta k^2}{\left(\beta^2-k^2\right)^2}\right]^{\pm 1}=0 \qquad [2.9]$$

$$\alpha^2=k^2-\frac{\omega^2}{V_P{}^2} \quad \beta^2=k^2-\frac{\omega^2}{V_S{}^2} \quad k=\frac{\omega}{V_{ph}}$$

where V_P and V_S are the p-wave and s-wave velocities, respectively; ω is the angular frequency; k is the wave number; V_{ph} is the phase velocity; h is half the thickness of a plate. The exponent +1 and -1 represent the solutions for the symmetric Lamb modes and anti-symmetric Lamb modes, respectively (Yang et. al 2009).

Unlike body waves and R-waves whose velocities are only functions of elastic constants of material properties, Lamb waves are dispersive in homogeneous media. For a typical cast iron plate (V_P = 5550 m/s, V_S = 3090 m/s, V_R = 2850 m/s and h = 4 mm) the dispersion curves for Lamb modes are calculated in Figure 2.7 using Eq. 2.9. Fundamental modes S0 and A0 show dispersion at low frequencies. Their phase velocities converge to the V_R at higher frequencies where $\lambda \sim h$. R-waves exist at high frequencies where the plate half-thickness is large relative to the wavelength; the slab in this case behaves like a half-space for R-wave propagation because the surface waves can travel independently on one surface without interference from the other surface. Higher Lamb modes appear at sequentially higher resonant frequencies. The fundamental mode creates significantly larger movements at the surface of a medium than p-waves and can therefore mask the p-wave energy arriving at a specific point. Both changes in material velocities and changes in plate thickness affect Lamb wave dispersion curves.

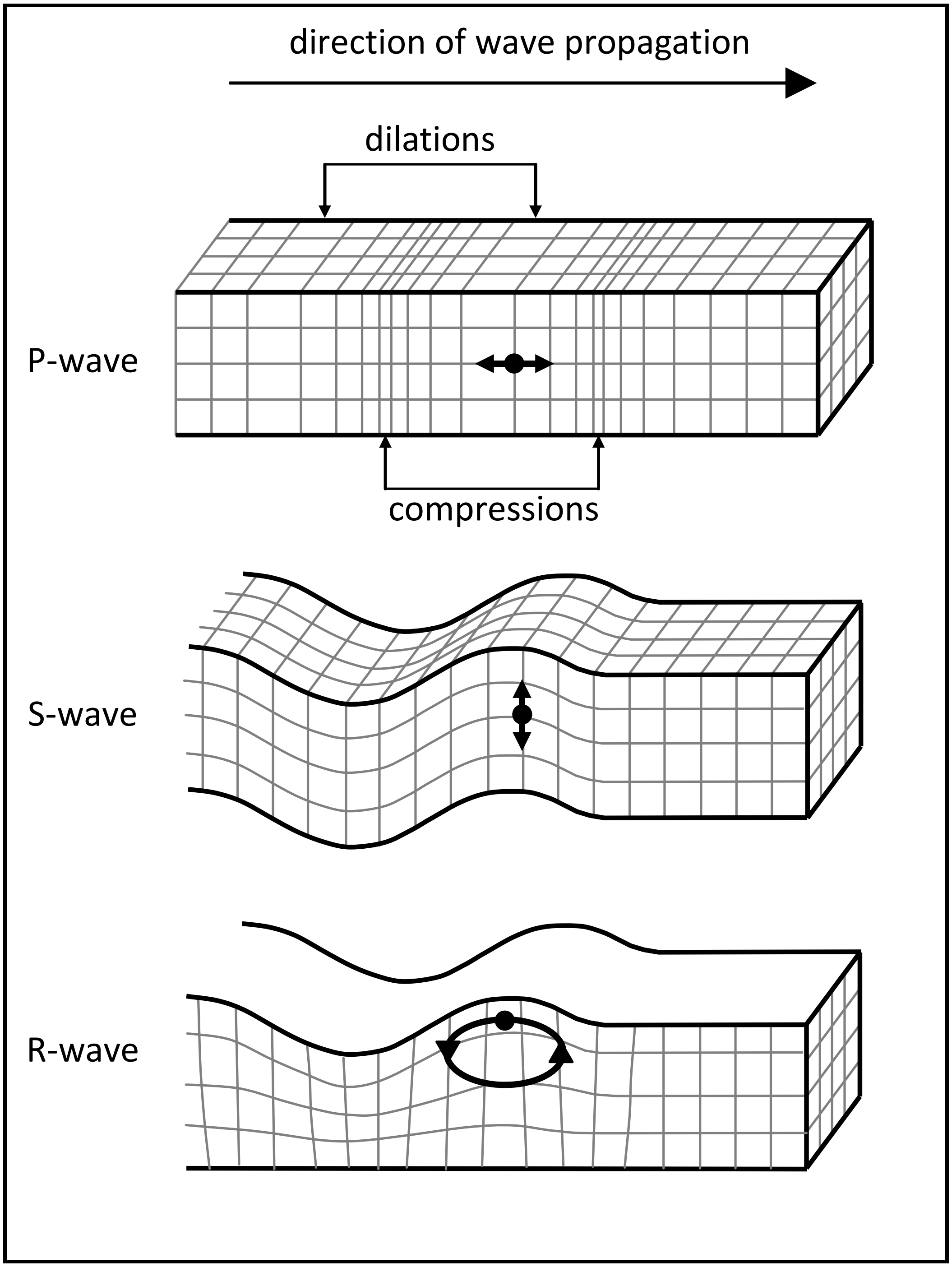

Figure 2.1: Particle motions of different wave types (Keary et al. 2002)

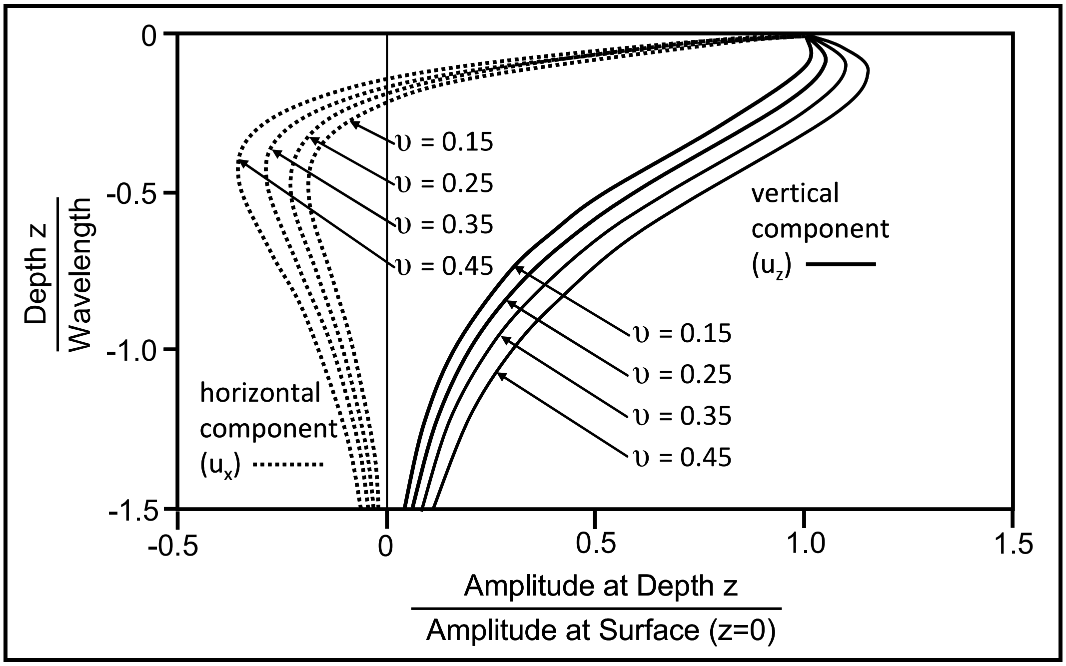

Figure 2.2: Change in magnitude of R-Wave particle motion with depth

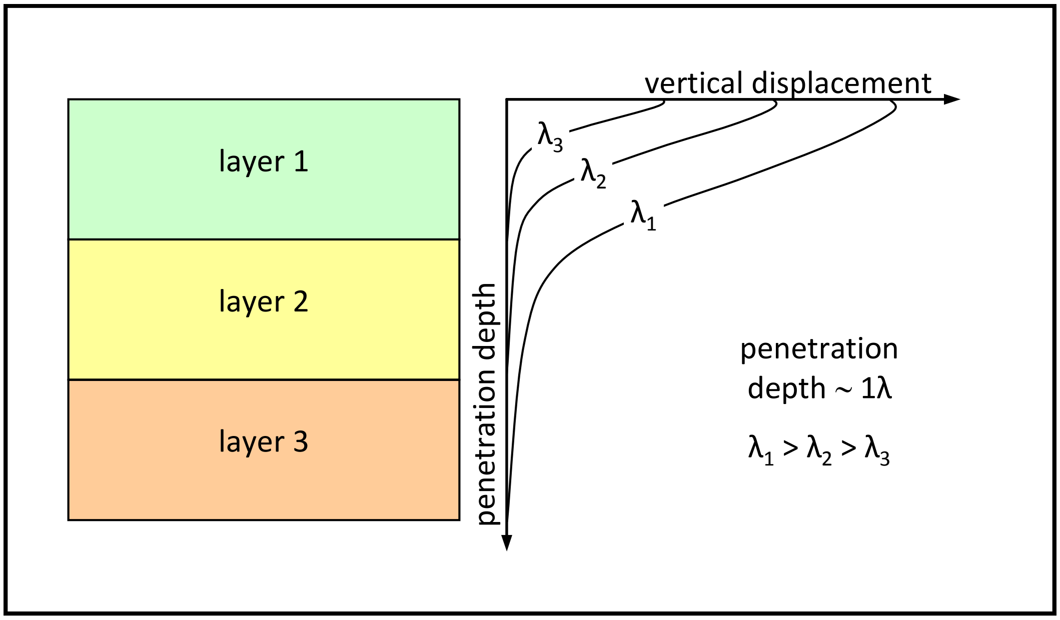

Figure 2.3: Penetration depth of surface waves

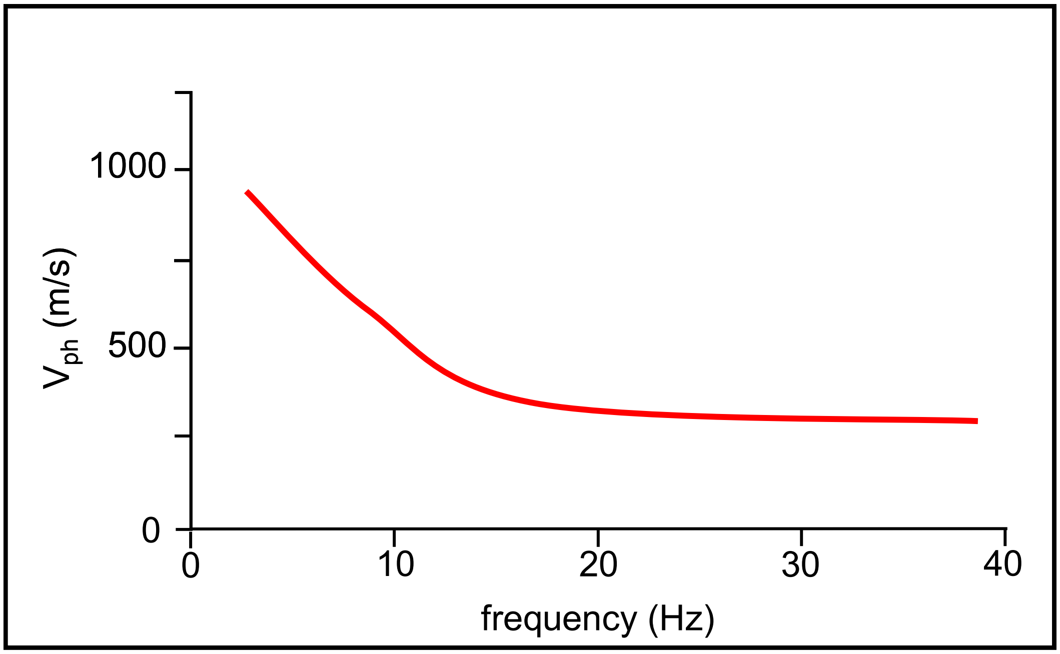

Figure 2.4: Illustration of R-wave dispersion curve

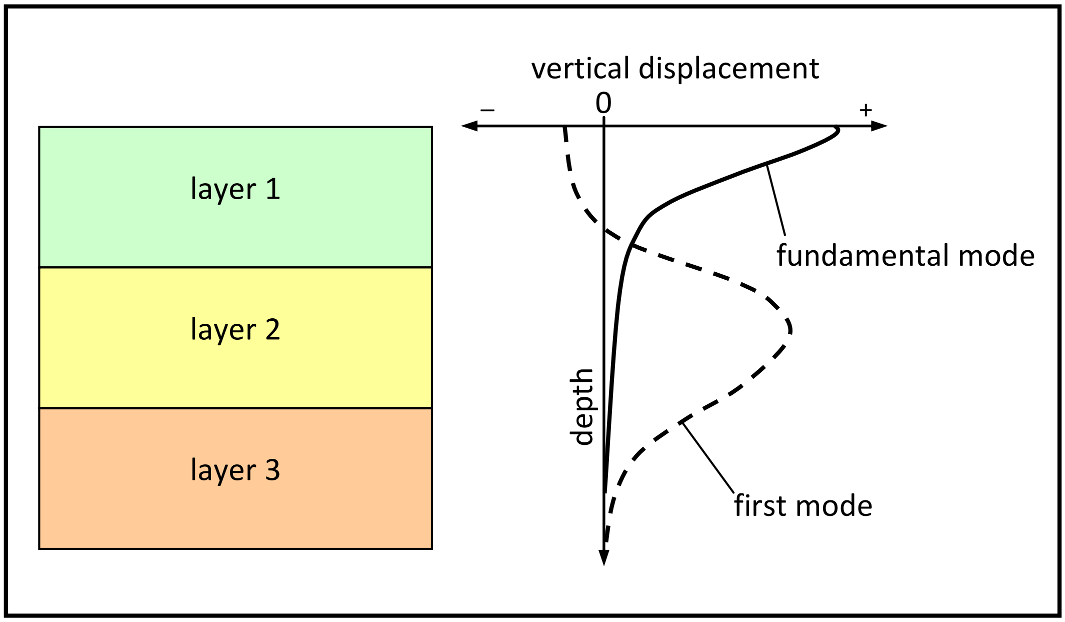

Figure 2.5: Possible shapes for surface wave modes

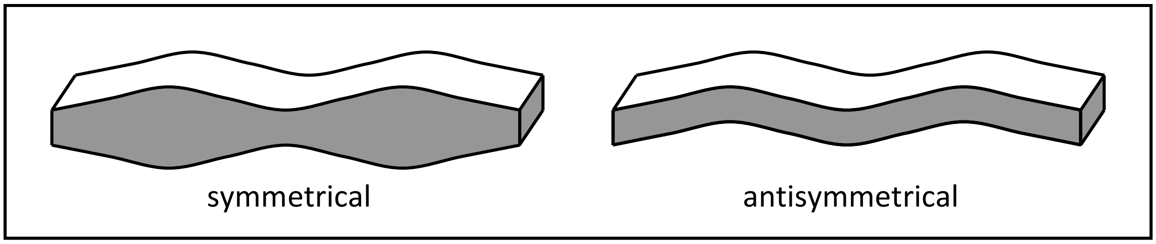

Figure 2.6: Lamb wave mode shapes (Blitz and Simpson 1996)

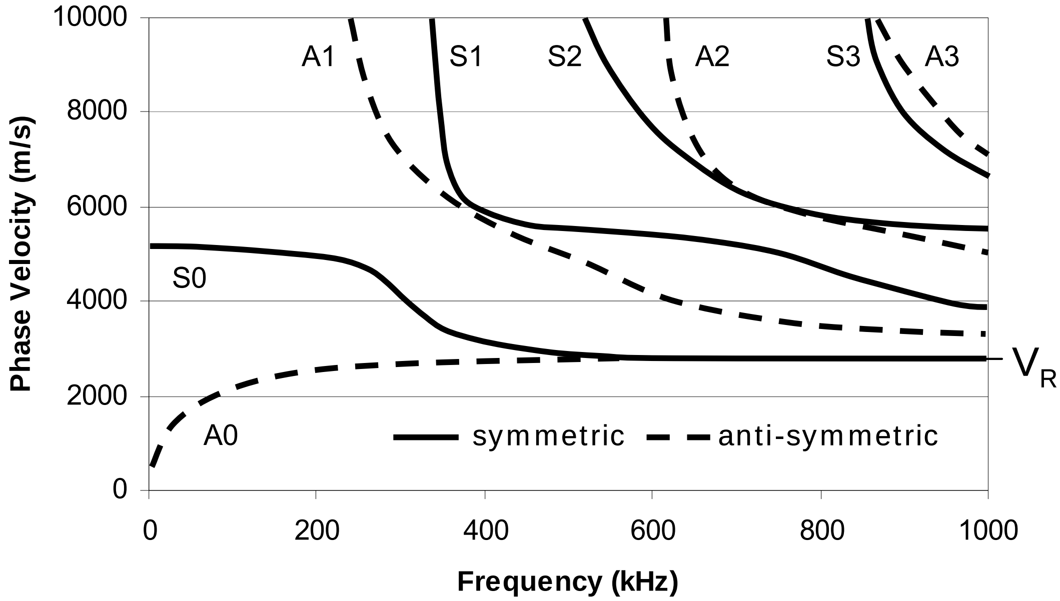

Figure 2.7: Theoretical Lamb wave dispersion curves for a typical cast iron plate (V_P = 5550 m/s, V_S = 3090 m/s, V_R = 2850 m/s and h = 4 mm)

CHAPTER 3: SPECIFIC APPLICATIONS OF NONDESTRUCTIVE TESTING

3.1 Ultrasonic Pulse Velocity Testing

Ultrasonic testing uses the characteristics of the propagation of high frequency body waves ($f > 20$ kHz) through a media to evaluate its internal structure. This non-destructive technique is widely used in the automotive and aerospace sectors for detecting flaws and defects in manufactured materials. Ultrasonic pulse velocity (UPV) testing is used to directly measure the body wave velocity (generally V_P) in different materials.

3.1.1 Fundamentals of UPV

In this method, a mechanical pulse is emitted by a transmitter, the pulse travels through the medium, and finally is detected by a receiver as shown in Figure 3.1. The travel time of the first arrival is precisely measured with electronic equipment. Typically, the transmitter and the receiver are placed on the opposite faces of the test object. The first arrival time divided by the length of the sample gives a measure of the compressional wave velocity (V_p in Eq. 2.3). P-waves are the fastest elastic waves and therefore are the first to be detected at the receiver. Generally high wave velocities are attributed to stiff materials with high elastic moduli.

Generally ultrasonic tests are able to resolve features of one wavelength and greater in size. If the wavelengths are large in comparison with the length of the specimen, the measured velocity is incorrect; the wavelengths should be at least half the length of the specimen to avoid near-field effects (Graff 1991). Thus, the evaluation of the wavelengths generated is critical to ensure the validity of the results. Waveform energy is inversely proportional to frequency. As a result, high frequencies attenuate faster than low frequencies as a wave travels through a medium. Different materials have different damping properties and will therefore attenuate elastic energy to greater or lesser extents. Materials with more defects generally have greater attenuating effects than sound materials. This relationship between pulse energy and frequency influences the selection of source frequency content and consequently also the resolution of the test. A high-frequency source may not be practical in a high-attenuating material. The energy of the source pulse may be dissipated before it reaches the receiver depending on the source-receiver separation distance (Khan et al. 2010).

3.1.2 Interpretation of UPV

The sample length and arrival time are used to calculate the transmission velocity of the material. Commonly, only the arrival time is analyzed in the pulse velocity test which represents a single data point in the time domain. Conversely, Fourier analysis can be used to access information contained within the frequency content of the entire signal. The discrete Fourier transform, X(f), of the time domain signal, x(t), is given by (Bracewell 2007)

$$X(f) = \sum_{t} x(t) \cdot e^{-i(2\pi f)t} \qquad [3.1]$$

where t is time ($t = j\ \Delta t$), f is frequency ($f = k\ \Delta f$), Δt and Δf are the discrete steps in time and frequency, j and k are integer indices or counters, and i is the imaginary unit($i^2 = -1$). Each component of the frequency spectrum X(f) represents the relative participation of a sinusoidal function with frequency f in the measured signal. For example, Figure 3.2 illustrates the discrete Fast Fourier Transform (FFT) performed on two periodic time signals. The first signal is composed of a single sin function with a frequency of 2000 Hz ($f_1 = \sin(2\pi \cdot 2000t)$). The Fourier magnitude (|FFT|) spectrum for f_1 shows only one peak corresponding to the function's only frequency of 2000 Hz. The second function is composed of the addition of two sin functions with different frequencies and amplitudes ($f_2 = \sin(2\pi \cdot 2000t) + 0.5 \sin(2\pi \cdot 4000t)$).The |FFT| spectrum for f_2 shows two peaks at the two frequencies making up the signal and also the relative magnitude of their contributions to the signal (the peak at 2000 Hz is twice that of the peak at 4000 Hz because of the different amplitudes of the two sin functions making up f_2). Frequency content analysis and the wave velocity of an ultrasonic signal allow the calculation of the wavelengths generated during testing ($V = f\ \lambda$). The area of the frequency spectrum is an indication of the energy of the signal and can therefore be used as a measure of the damping properties of the tested material.

The wavelet transform (WT) provides a significant advantage over Fourier transforms: the ability to see changes in frequency content with time. These functions decompose the original signal into its different frequency components. Daubechies' Wavelets are one of the most commonly used discrete WTs. This WT decomposes the original signal into coefficients representing the energy within the signal at different frequencies. The coefficients within different levels of frequency bandwidth are used to reconstruct time signals at these different levels (eg. 0 to 1 kHz, 1 to 3 kHz, …, 500 to 1000 kHz). The number of levels and their frequency bandwidth is dictated by the sampling rate and the length of the signal. These new time signals describe the changes within the original time signal at specific frequency levels.

3.1.3 Problems and Limitations

The damping characteristics of different materials can limit the resolution of a UPV test. A high frequency source may not have enough energy to penetrate the desired material. For example, one MHz waves can penetrate a sample of cast iron pipe that is many metres long but are fully attenuated by a 20 cm long sample of asphalt. Furthermore, the energy of p-waves is relatively less than s-waves and surface waves (R-waves or Lamb waves). If adequate resolution in the data acquisition is not used, the arrival of the slower s-waves or surface waves can be mistaken for the lower amplitude p-waves resulting in errors in reported velocities.

3.2 Electric Resistivity Imaging

Electrical resistivity imaging (ERI) is a geophysical method used to infer subsurface structure based on the variation in electrical resistivities of different geological materials. The test is accomplished by generating a current through the ground and measuring the resulting potential differences at the surface. Measured deviations from normal potentials are used as an indication of subsurface variations in electrical conductivity resulting from changes in lithology or the presence of water. The following summary was prepared with reference to Keary et al. (2002).

3.2.1 Fundamentals of ERI

The fundamentals of electric current flow through the ground are illustrated by considering a homogeneous cylinder of length (δL), resistance (δR), and with a cross-sectional area (δA) (Figure 3.3). The potential drop (-δV) across the cylinder created by an induced current (I) is given by Ohm's law

$$-\delta V = \delta R I \qquad [3.2]$$

The resistivity (ρ) of a material is described as its resistance per unit length to electric current. It is given by

$$\rho = \frac{\partial R \partial A}{\partial L} \qquad [3.3]$$

substituting for δR into Eq. 3.2 gives

$$\frac{\delta V}{\partial L} = -\frac{\rho I}{\delta A} \qquad [3.4]$$

For a single electrode on the surface inducing a current, the current flows radially away from the electrode as shown in Figure 3.4. As the current reaches a distance (r) from the source, it is evenly distributed over a hemispherical surface-area of $2\pi\ r^2$. Substituting for δA in Eq. 3.4, the potential gradient with respect to r is given by

$$\frac{\delta V}{\delta r} = -\frac{\rho I}{2\pi r^2} \qquad [3.5]$$

Integrating Eq 3.5 gives a formula that can be used to calculate the potential (V_r) at any distance r from the electrode:

$$V_r = \int \partial V = -\int \frac{\rho I \delta r}{2\pi r^2} = \frac{\rho I}{2\pi r} \qquad [3.6]$$

Finally, for the case where the circuit is completed with a current source electrode at point A and a sink electrode at point B (Figure 3.5), the potential V_C at point C is given by adding the potential contributions from the source and sink electrodes (V_A and V_B respectively):

$$V_C = V_A + V_B \qquad [3.7]$$

From Eq. 3.6

$$V_C = \frac{\rho I}{2\pi}\left(\frac{1}{r_A} - \frac{1}{r_B}\right) \text{ and } V_D = \frac{\rho I}{2\pi}\left(\frac{1}{R_A} - \frac{1}{R_B}\right) \qquad [3.8]$$

The potential difference ΔV between C and D is given by

$$\Delta V = V_C - V_D = \frac{\rho I}{2\pi}\left\{\left(\frac{1}{r_A} - \frac{1}{r_B}\right) - \left(\frac{1}{R_A} - \frac{1}{R_B}\right)\right\} \qquad [3.9]$$

Therefore

$$\rho = \frac{2\pi \Delta V}{I\left\{\left(\frac{1}{r_A} - \frac{1}{r_B}\right) - \left(\frac{1}{R_A} - \frac{1}{R_B}\right)\right\}} \qquad [3.10]$$

In summary, the resistivity of a material can be obtained by measuring the potential difference across two electrodes placed between an additional two electrodes that are generating a current through the material.

The depth of current penetration in a resistivity survey increases as the spacing between the electrodes increases; resolution at shallower depths is lost with increased penetration depth. In a homogeneous subsurface, the calculated resistivity should be constant throughout and independent of surface location and electrode spacing. When inhomogeneities are present, the resistivity is dependant on the relative positions and spacing of the electrodes. Any calculated value for resistivity is called the apparent resistivity (ρ_a) and is dependant on the geometry and size of the inhomogeneity.

Many different electrode configurations have been designed for electrical resistivity imaging. One of the most commonly used arrays is the Wenner configuration. This technique uses equal spacing (a) between the current and potential electrodes (Figure 3.6). Substituting a for the electrode spacing into the Eq. 3.10 gives

$$\rho = \frac{2\pi\,\mathrm{a}\Delta\mathrm{V}}{\mathrm{I}} \qquad [3.11]$$

During a survey, the electrode array is sequentially moved down the desired line with a fixed spacing.

3.2.2 Interpretation of ERI

Inversion software (e.g. Geotomo Res2dinv) is commonly used to interpret resistivity data and generate a two-dimensional electrical resistivity structure of the ground below the survey line. The term inversion is used here in reference to the solution of a non-squared system of equations by minimizing the error between predicted and measured values. Such programs divide the subsurface below the survey line into a simplified model of rectangular blocks. In order to obtain a resistivity model of the subsurface, the apparent resistivity of each block is adjusted iteratively until the differences between the calculated and field-measured resistivities converge (Geotomo Software 2009).

3.2.3 Problems and Limitations

The results of a resistivity data inversion can be ambiguous in that multiple models can generate the same electric potentials as measured in the field. As a result, this geophysical method is commonly completed in tandem with exploration boreholes. Furthermore, interpretations are limited to simple subsurface conditions (e.g. gradual changes in thickness and depth of layers). Finally, topography and near-surface resistivity variations can interfere with detection of effects resulting from deeper variations.

3.3 Seismic Refraction Surveying

Seismic investigations make use of the fact that seismic waves travel through different media at different velocities. By generating seismic waves and recording their arrival times at numerous points on the ground surface, subsurface interfaces between different geological materials can be located where the waves are reflected or refracted (Sharma 1997). Seismic refraction surveying specifically was the first major geophysical method to be used in oil exploration. This method has become increasingly popular for use in site investigations for civil engineering applications. It is most useful for shallow subsurface studies, in particular when used in tandem with borehole drilling (Redpath 1973).

This technique involves producing seismic energy and measuring the travel times of the refracted waves at different points along the ground surface. The resulting data consists of travel times and distances. A representation of the subsurface is obtained through interpretation of these data based on laws of energy propagation. The following summary was prepared with reference to Redpath (1973).

3.3.1 Fundamentals of SR

The propagation of seismic energy through a layered medium is governed by two main principles: Snell's Law and critical incidence (Figure 3.7). Snell's Law describes the relationship between the angular deviation a seismic pulse exhibits when crossing an interface between two different materials (refraction) and the ratio of the seismic velocities of the two materials. This law only applies when the velocity of the second medium is greater than that of the first. In most cases, this condition is met in the field as transmission velocities increase with successively deeper more compacted materials. Critical incidence is the specific case where the refracted pulse is parallel to the layer interface (β = 90° as shown in Figure 3.7). This phenomenon occurs at a critical angle of incidence, when the sin of this incident angle equals the ratio of the first and second layer transmission velocities ($\sin\alpha = V_1/V_2$).

Figure 3.8 illustrates a general seismic survey setup and raypaths in a simple two-layer case. When a seismic pulse reaches the interface between layers at the critical angle of incidence (B), it is acceptable to assume that the wave will propagate along the boundary (BC) at the higher velocity of the lower layer. As the refracted pulse follows the interface, it generates waves that depart at the critical incident angle (C) into the upper layer at the lower velocity.

At relatively short distances from the source (less than AD), the first waves to arrive at the surface are those travelling directly from the source to the surface through the upper layer. At a certain distance from the source (D), the arrival of these shallow waves is overtaken at by waves refracted at the interface. The refracted energy follows a longer ray path (ABCD) but travels at a higher velocity along the layer boundary. It is able to overcome the lateral movement of the slower waves in the upper layer given enough distance. In a scenario with multiple layer interfaces, the arrival of waves refracted from one boundary will eventually be overtaken by energy refracted by any subsequently deeper interface with a layer of higher velocity. This behavior of seismic energy is fundamental to the interpretation of seismic refraction data.

3.3.2 Interpretation of SR

There are a variety of methods used to interpret seismic refraction data. Each has its own benefits and drawbacks depending on specific site conditions and the data set at hand. This section will provide a brief overview of some commonly used interpretation techniques. More detailed explanations can be found in a number of geophysical references.

3.3.2.1 Time-Intercept Method

The time-intercept method is the simplest method used for analyzing seismic refraction data. The simple two layer case is again used to illustrate this method. First, a time distance-plot is generated by plotting the first arrival times against the corresponding distance-from-source at each detector as shown in Figure 3.9.

The initial arrivals are those from direct pulses through the first layer. The slope of the line through these early data points ($\Delta T/\Delta X$) is the reciprocal of the transmission velocity of the first layer ($1/V_1$). Where the direct arrivals are overtaken by the refracted wave arrivals, a decrease in the slope through the data points is observed. The location where the break in slope is observed is known as the critical distance (X_C). The decreased slope through the points beyond the critical distance represents the reciprocal of the velocity of the second layer ($1/V_2$). Projecting a line through the refracted points back to the time axis gives the intercept time (T_i).

The depth of the refracting boundary (Z_1) is given by

$$Z_1 = \frac{\Delta T_i V_1}{2\cos\left(\sin^{-1}\left(V_1/V_2\right)\right)} \qquad [3.12]$$

This formula is derived by solving for the travel time of the refracted wave using the geometry of the raypath and rearranging to solve for Z_1. The complete derivations of all referenced formulas are given by Redpath (1973).

The time-intercept method can be modified for cases with multiple layers and dipping layers. However, one significant disadvantage of this method is that it is only applicable to planar and parallel layer interfaces. This presents a problem as many geological boundaries are irregular and not always parallel. In addition, the depth computed using this method is actually a depth projected back to the location of the seismic source. If the survey consists of only one shot, only one depth to the refracting surface can be obtained.

3.3.2.2 Reciprocal Method

The reciprocal method can be used to provide greater detail than a time-intercept interpretation. This technique uses the concept of delay times to calculate refractor depths below individual detectors in the survey line. The definition of delay time is illustrated in Figure 3.10; it is the difference between the time spent by the seismic wave travelling up or down through the upper layer, and the time it would have spent travelling along the layer interface at the refractor velocity.

The depth to the refractor below the detector (Z_D) according to the delay time at that specific detector (ΔT_D) is given by

$$Z_D = \frac{\Delta T_D V_1}{\cos\left(\sin^{-1}\left(V_1 / V_2\right)\right)} \qquad [3.13]$$

Delay times can be determined from a seismic refraction survey by capturing shots from both ends of the line. From the reversed shots, the total travel time (T_t, - which is the arrival time recorded at the detector furthest from the source) and the arrival times at a detector from the forward and reverse shots (T_{D1} and T_{D2} respectively) can be used to calculate ΔT_D:

$$\Delta T_D = \frac{1}{2}\left(T_{D1} + T_{D2} - T_t\right) \qquad [3.14]$$

It is important to note that the delay time at a specific geophone can only be calculated when the arrivals from the forward and reverse shots are from the same refracting surface. Shots can be fired beyond the ends of the survey line to increase the overlap in reversed arrival times.

The reciprocal method can also be expanded for a multiple layer case. This technique allows detection of dipping and irregular layer interfaces as depths below each individual geophone in the survey line can be determined. However multiple shots are required to provide sufficient overlap in the arrival times. In addition, the data interpretation is much more involved than a simple time intercept-interpretation.

3.3.2.3 Tomographic Inversion

Tomographic inversion generally requires specialized software packages such as Geometric's SeisImager/2D. This method begins with an initial velocity model of multiple layers with a range of velocities specified by the user. The time-intercept or the reciprocal methods can be used to determine an applicable velocity range for the initial model. This initial model consists of many individual constant velocity cells. The size of cells can be adjusted by the user.

A tomographic inversion involves iteratively tracing rays through different source and receiver combinations in the model. The velocities in each cell are adjusted following each iteration to minimize the difference between the calculated and measured arrival times. The math is very involved, but in general the raypath through each cell is governed by the fundamental principles of seismic wave propagation discussed above. The result is a model illustrating contours of cells with the same refraction velocity as an alternative to continuous constant velocity layers. Although tomographic inversion requires expensive software packages, it can model gradual changes in refraction velocity and localized anomalies.

3.3.3 Problems and Limitations

A significant problem that can limit the success of a seismic refraction survey is a velocity reversal. A velocity reversal occurs when a low-velocity layer underlies a higher-velocity layer. In this case the seismic wave is actually refracted downwards, away from the layer interface as show in Figure 3.11. Refractions from this low-velocity layer are not detected at the surface. The effect on the analysis is computing depths greater than actual because arrival times are larger than they would be if the waves did not pass through the low-velocity layer. In addition, gradual variations in velocity, both vertical and lateral, can dramatically affect the success of time-intercept and delay time analyses. Both of these methods assume layers of constant velocity. However, a tomographic inversion can successfully identify such gradual variations.

3.4 Multiple-Channel Analysis of Surface Waves

Multiple-channel analysis of surface waves (MASW) is another seismic surveying technique. This method has become a useful tool for shallow soil geotechnical investigations due to technical advancements in data acquisition equipment and development of processing software over the past ten years. Like SR surveying, MASW data collection involves generation of a seismic wave and measurement of surface movements with an array of transducers. However, instead of using a single arrival time from each recorded time signal as in SR interpretation, the entire time signals are analyzed in MASW processing. The dispersive nature of surface waves provides a scanning downwards investigation from measurements taken at the surface. A model representing the variation in shear-wave velocity with depth is obtained through inversion of the data.

3.4.1 Fundamentals of MASW

The MASW method uses the dispersive nature of surface waves to interpret multi-layered stratigraphy. When a seismic pulse is created on the ground surface, about two thirds of the seismic energy at the surface travels in the form of R-waves. In the presence of different soil layers, the surface wave velocity depends not only on the properties of the soil layers but also on the frequency content of the excitation (Nazarian and Stokoe 1984). The depth of penetration into the soil is a function of the wavelength (λ), with longer wavelengths penetrating deeper into the soil. The effective depth of penetration of a surface wave is commonly taken as one wavelength, with most of the energy concentrated between the surface and a depth of 1/3 λ. Consequently, high frequencies (short λ) propagate at the velocity of the upper layer, whereas lower frequencies (larger λ) propagate at velocities determined by the characteristics of subsequently deeper soil layers (Lai and Wilmanski 2005). Surface waves have multiple modes of propagation. The fundamental mode is very important in MASW analysis because its maximum particle displacement occurs near-surface and can therefore be measured with transducers at the ground level.

The MASW method utilizes an array of geophones and a seismic source. Complete time traces of the seismic event are recorded at each geophone to produce a seismograph. The phase difference as a function of frequency ($\Delta\phi(f)$) between two adjacent geophones is computed according to

$$\Delta\phi(f) = \text{phase}\left(G(f) \cdot F^*(f)\right) \qquad [3.15]$$

where G(f) and F(f) are the Fourier transforms of the time signals from the second and first geophones, respectively, and * denotes the complex conjugate. The phase shift ($\Delta\phi(f)$) and the geophone spacing (Δx) are used to calculate the phase velocity at a given frequency ($V_{ph}(f)$) by

$$V_{ph}(f) = 2\pi f \frac{\Delta x}{\Delta\phi(f)} \qquad [3.16]$$

The calculated V_{ph} is an average velocity of the medium between two receivers. A dispersion curve is generated by plotting the variation in phase velocity with frequency. This curve shows how different frequencies penetrating to different depths propagate at different velocities through the soil layers.

Dispersion curves can be obtained through the application of the Two-Dimensional Fast Fourier Transform (2DFT). A seismograph contains both time and spatial information. The discrete 2DFT ($F(\omega,k)$) of a seismograph ($f(x,t)$) representing a signal in time and spatial domains is given by (Bracewell 2007)

$$F(f,k) = \sum_x \sum_t f(x,t) e^{-i(2\pi f)t} e^{-ikx} \qquad [3.17]$$

where f frequency ($f = a\,\Delta f$); k is wave number ($k = 2\pi / \lambda$; $k = b\,\Delta k$); x is spatial location ($x = c\,\Delta x$); t is time ($t = d\,\Delta t$); Δf, Δk, Δt and Δx are the discrete steps in frequency, wave number, time and spatial location, respectively; a, b, c and d are integer indices or counters; and i is the imaginary unit($i^2 = -1$).

The 2D FFT is used to obtain an f-k plot from the seismograph as shown in Figure 3.12. F-k plots are useful for isolating the fundamental mode surface wave energy within the transformed seismograph from other types of waves and noise. R-wave energy is generally the highest amplitude energy within the f-k plot. The f and k values from one point is used to calculate the corresponding V_{ph} value ($V_{ph}(f) = f\,\lambda = 2\pi f / k$). Multiple data points within high energy areas from the f-k plot are selected to generate a measured dispersion curve showing the change in V_{ph} with f. A representation of the subsurface as an R-wave velocity profile (change in velocity with depth) is obtained by creating a layered model for which the corresponding theoretical dispersion curve matches the measured curve obtained through the f-k analysis. The R-wave equations for layered media have no closed-form solution, so complex integrals must be solved to generate a theoretical dispersion curve for a layered medium. These results can be used to estimate the shear velocity profile of a medium because the velocity of surface waves (V_R) in a homogeneous medium can be approximated as a function of V_s using Eq. 2.8. Theoretical dispersion curves for three different cases are presented in Figure 3.13. This figure shows that R-waves are non-dispersive in homogeneous media. In addition, the effect of different layering conditions on the fundamental and higher mode dispersion curves is illustrated.

3.4.2 Interpretation of MASW

Specialized software packages such as GeoStudy Astier's SWAN (GeoStudy Astier 2010) are used to generate dispersion curves from MASW data and perform inversions. These programs can be used for pre-processing the data, automatically generating f-k plots, and selecting points from the f-k plot to generate a measured dispersion curve. The inversion algorithms generally iterate through values of layer thicknesses and R-wave velocities in the layered model to minimize the error between the measured and theoretical dispersion curves.

3.4.3 Problems and Limitations

Velocity reversals (decrease in velocity with depth) make interpretation of MASW data more difficult. However, in some cases they can be identified and compensated for in the inversion process because the wave energy is analyzed in a logarithmic scale, where the high energy components (not affected by inverse layering) and the low energy components (affected by inverse layering) can be identified. The most common problem of the MASW method is the difficulty of generating frequencies that are low enough to penetrate to greater depths with adequate signal-to-noise ratios.

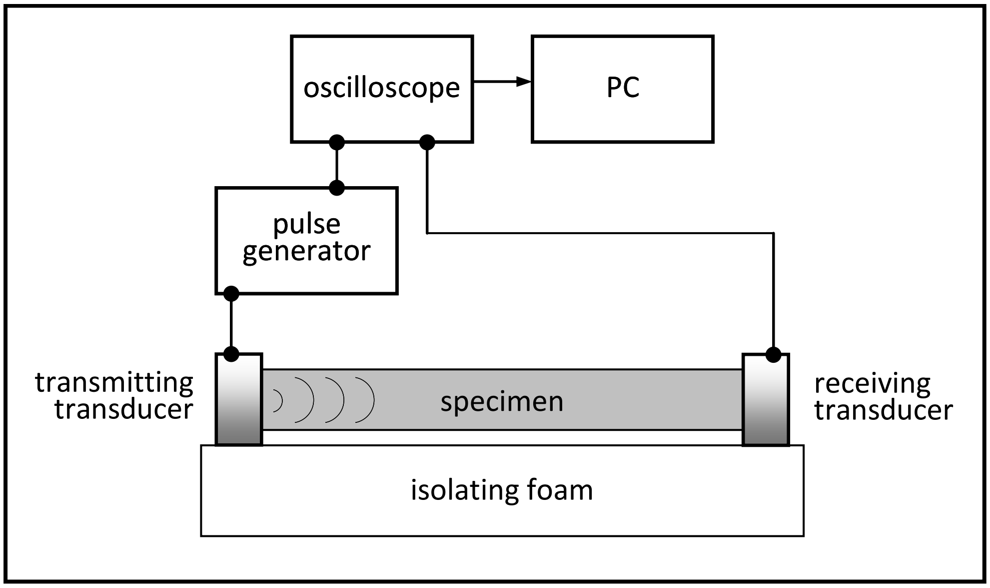

Figure 3.1: Ultrasonic pulse velocity testing setup

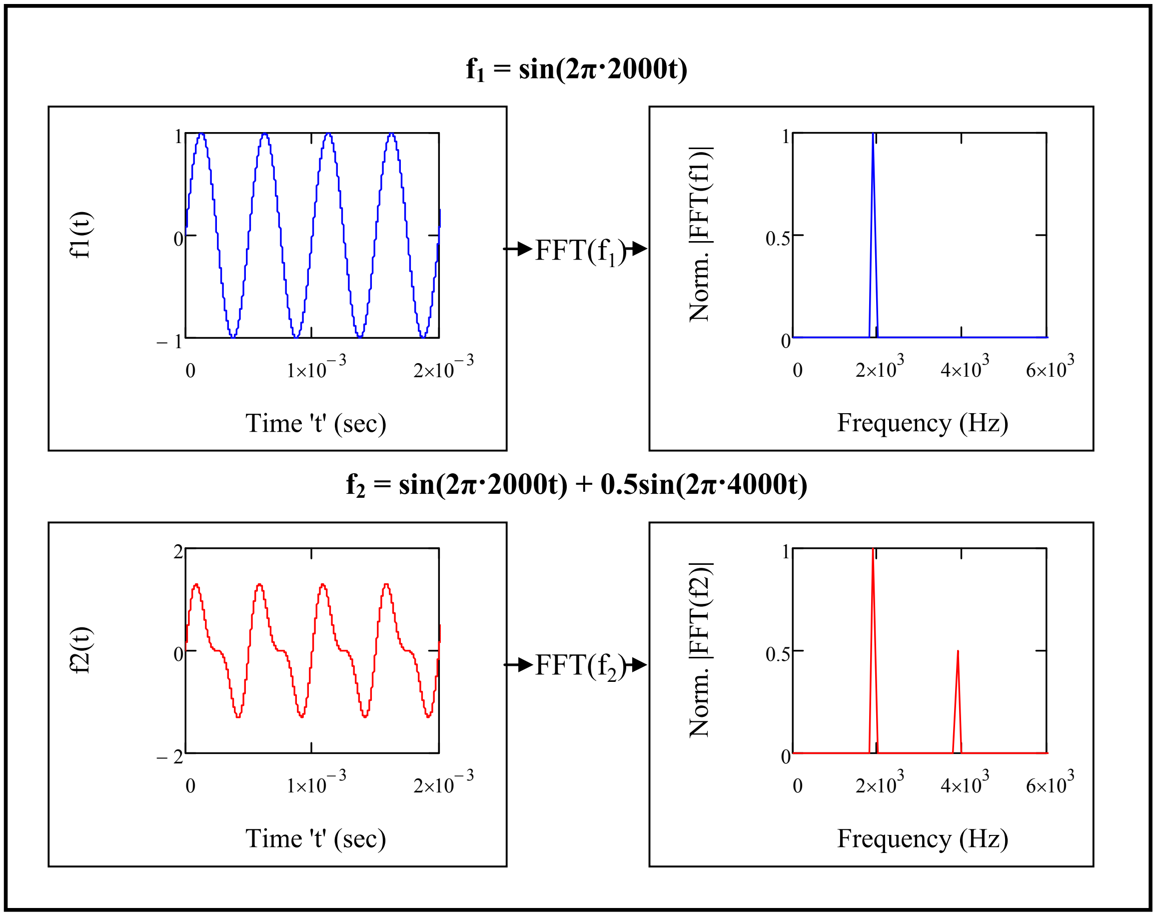

Figure 3.2: Example of discrete Fast Fourier Transform (FFT)

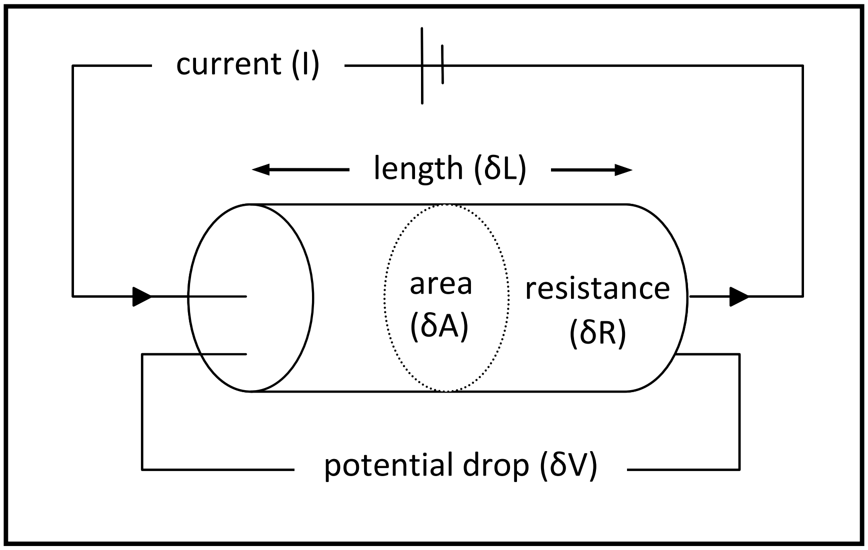

Figure 3.3: Variables required for computation of resistivity (Keary et al. 2002)

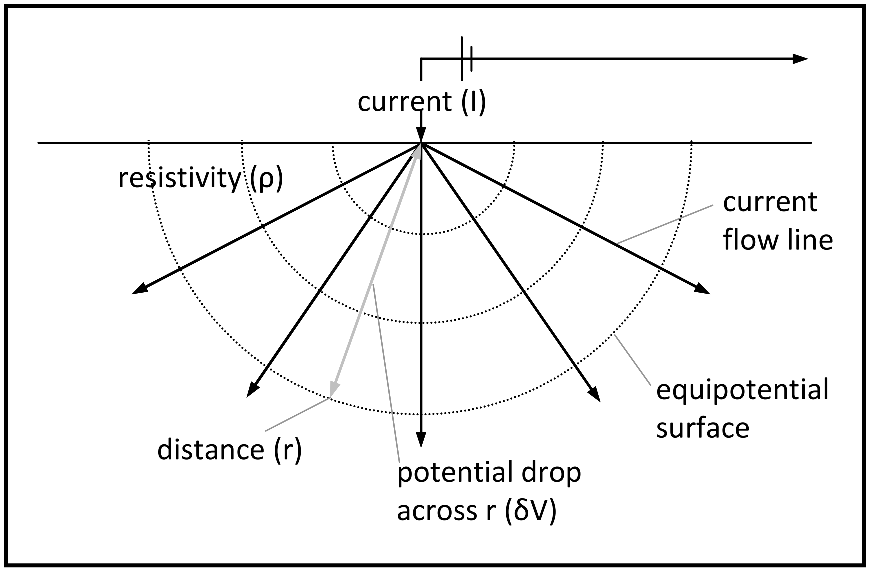

Figure 3.4: Current induced by single electrode (Keary et al. 2002)

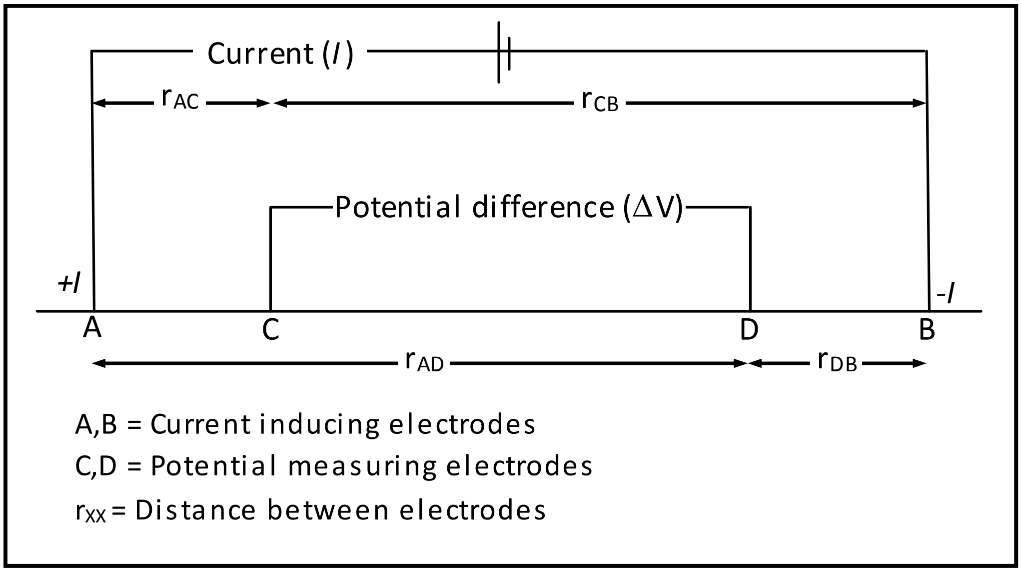

Figure 3.5: General electrode configuration used for electric resistivity surveying (Keary et al. 2002)

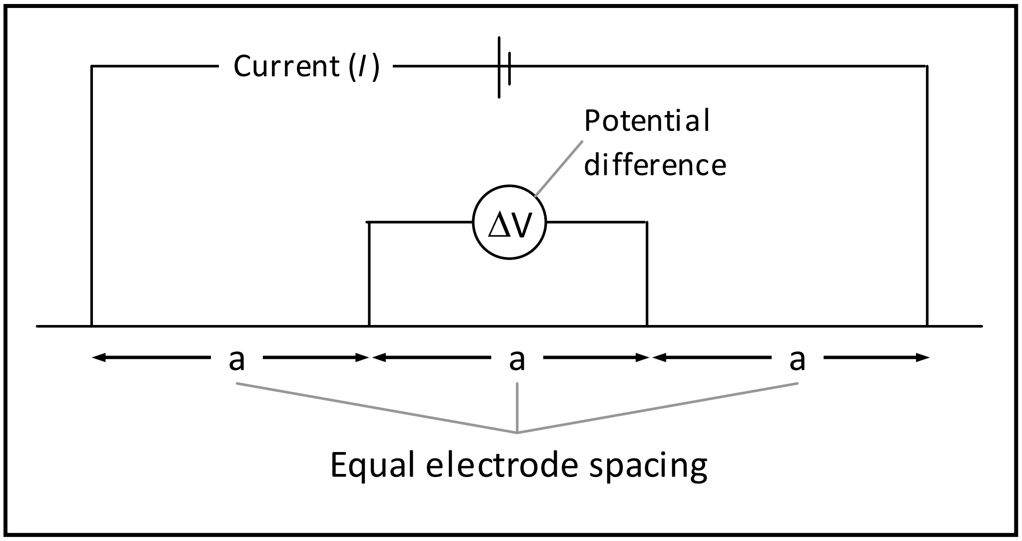

Figure 3.6: Wenner electrode array (Keary et al. 2002)

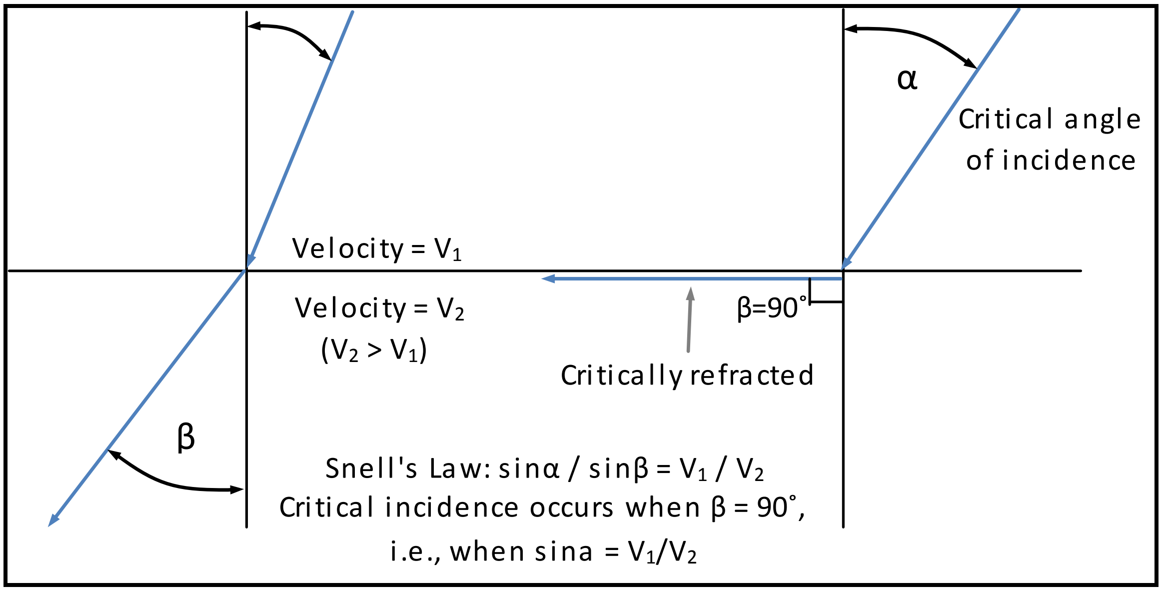

Figure 3.7: Snell’s Law and critical incidence (Redpath 1973)

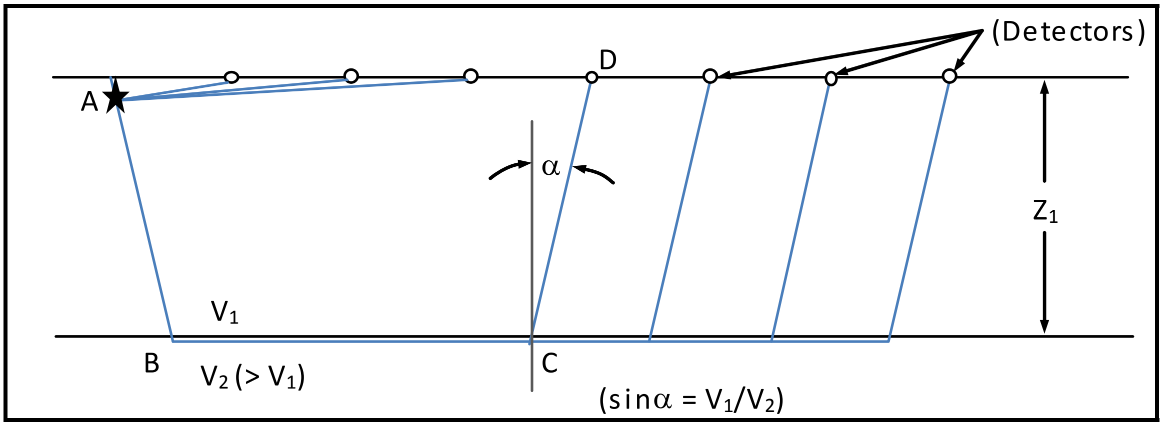

Figure 3.8: Simple seismic refraction survey raypaths (Redpath 1973)

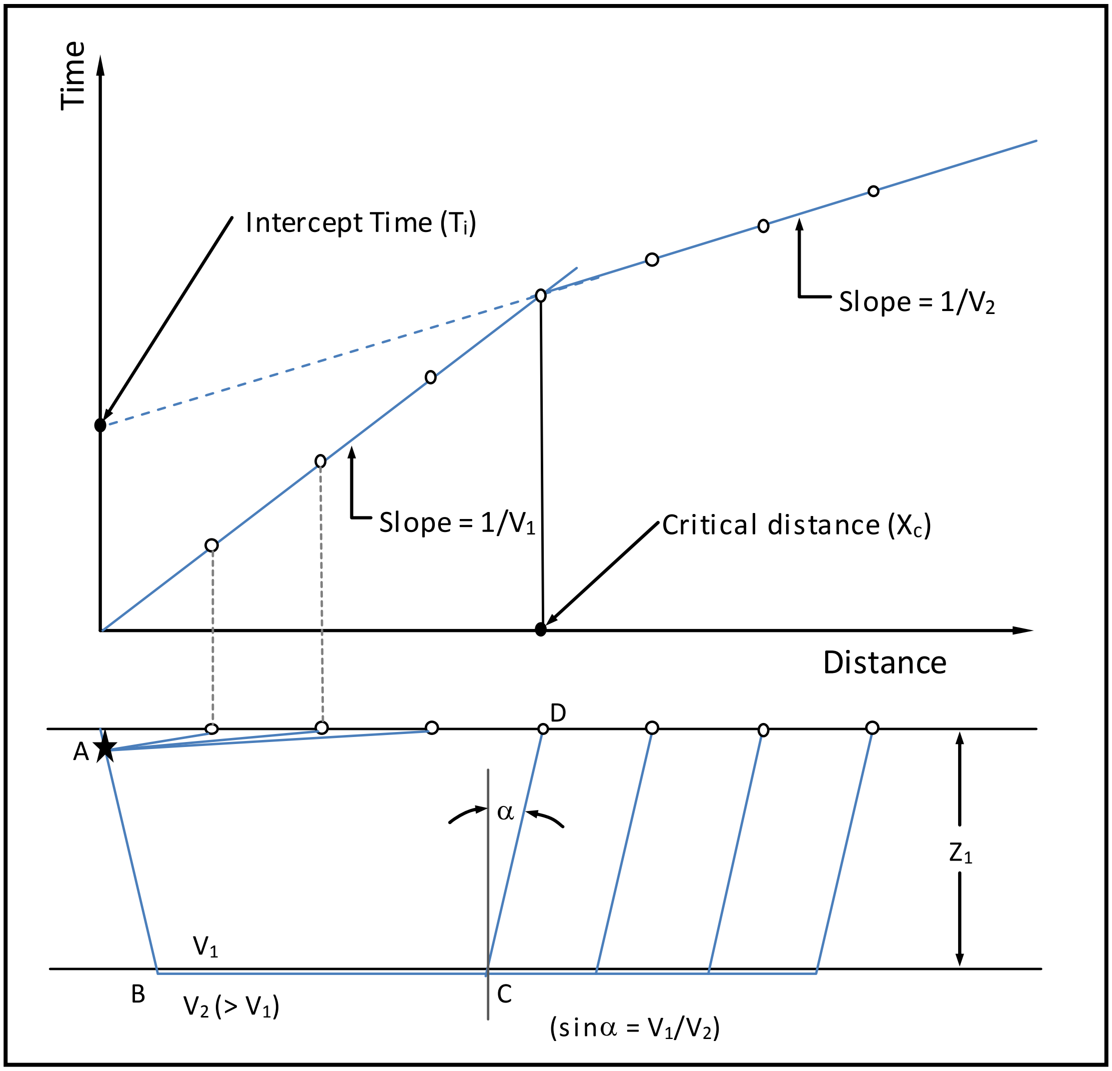

Figure 3.9: Time-distance curve from simple two-layer case (Redpath 1973)

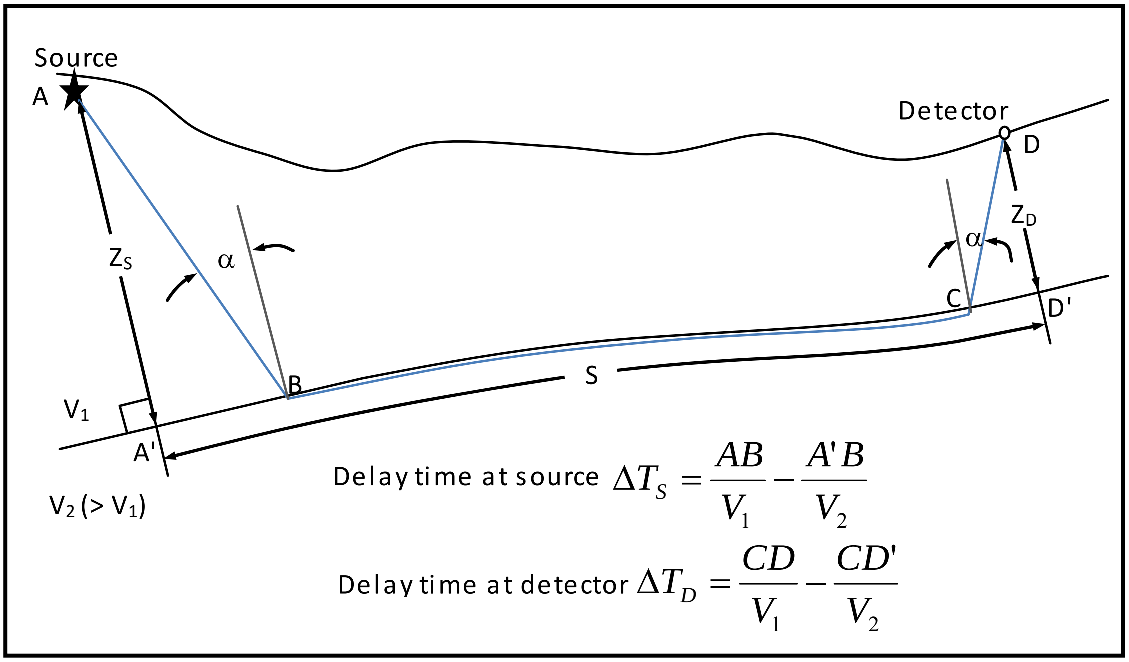

Figure 3.10: Definition of delay time (Redpath 1973)

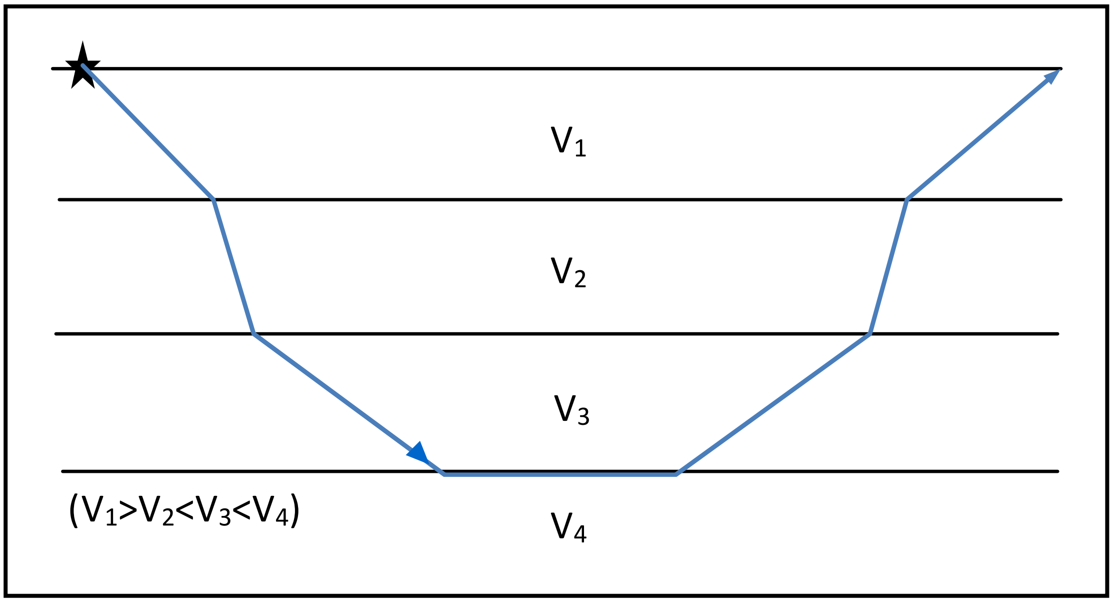

Figure 3.11: Refraction caused by velocity reversal (Redpath 1973)

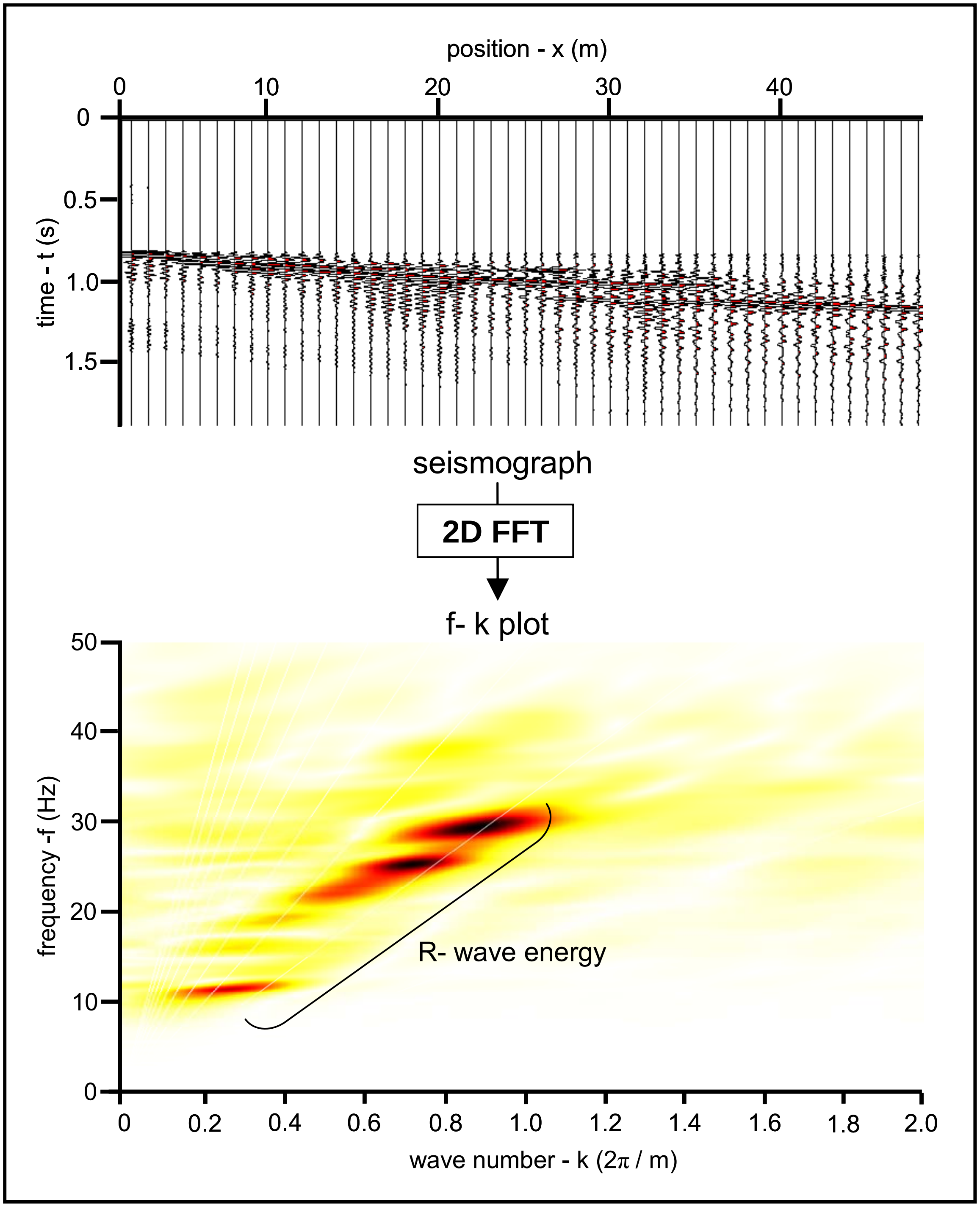

Figure 3.12: Illustration of f-k plot

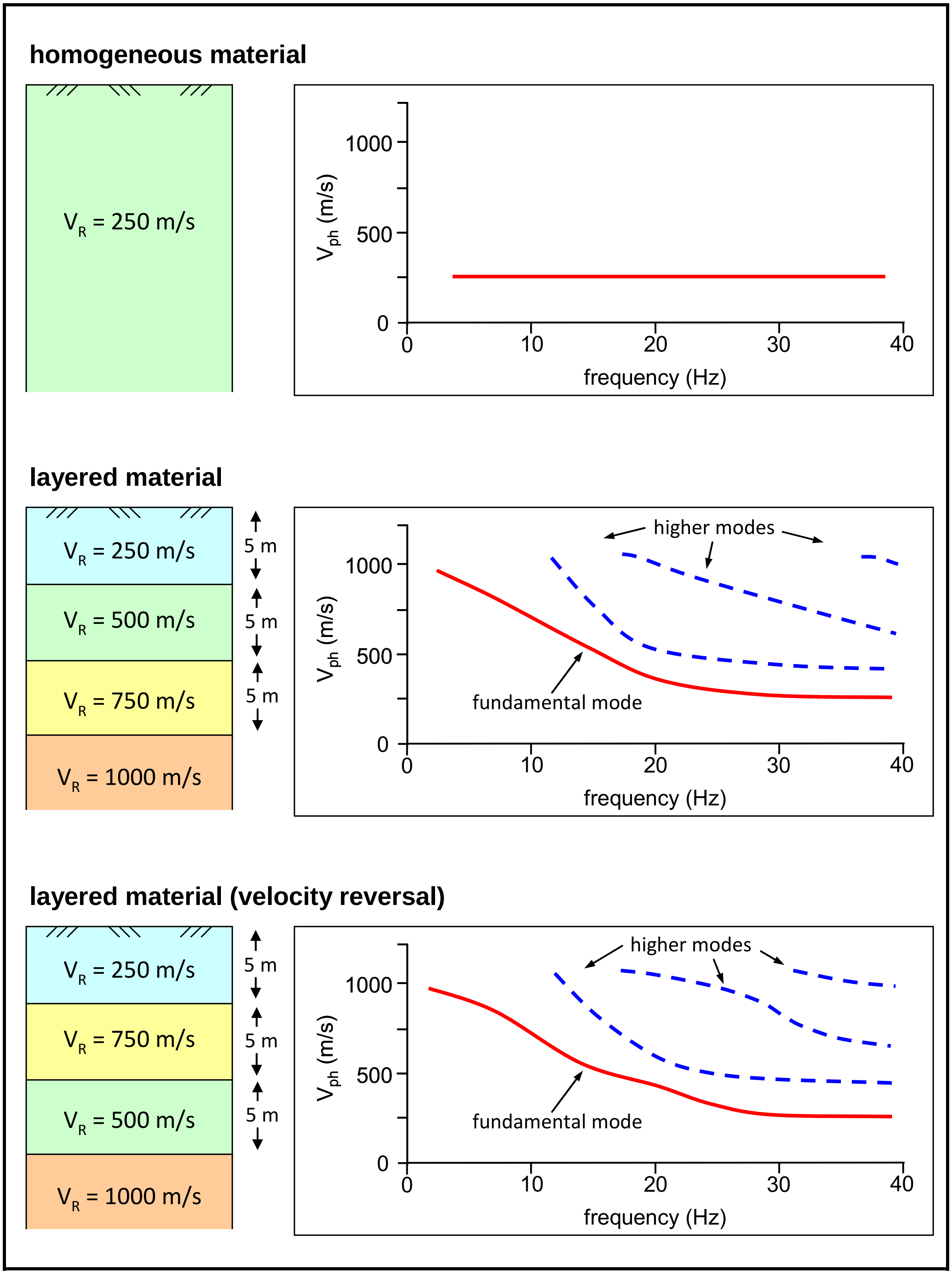

Figure 3.13: R-wave dispersion curves for different media

CHAPTER 4: LITERATURE REVIEW

4.1 Literature Review of Ultrasonic Testing on Cast Iron

Cast iron has been used to make water pipes in North America since the early nineteenth century (Koelble 2006). The first pipes were made of grey cast iron and manufactured using pit casting. This casting method was replaced by spin casting in the 1920s. This new manufacturing technique provided more even distribution of the molten iron during casting, reduction in the size of graphite flakes within the solidified microstructure and fewer manufacturing defects in general. Ductile iron succeeded grey cast iron as a pipe material in the 1940s. Cast iron pipes are currently made of ductile iron manufactured using spin casting and are commonly encased in polyethylene to mitigate corrosion (Seica and Packer 2004).

Cast iron is a generic term that applies to iron-carbon alloys containing more than two percent carbon; in general, it also contains small percentages of silicon and manganese, and trace amounts of phosphorous and sulphur. Cast iron unlike steel contains carbon in surplus of its solubility in solid iron. The result of this excess carbon is the precipitation of crystalline graphite during freezing (Walton 1971). Cast irons are generally classified by graphite shape and matrix composition. The microstructure of a cast metal depends primarily on chemical composition, cooling rate, and melt treatment (Davis 2006). Because graphite is a relatively weak material, generally an increase in graphite is associated with decreased strength in cast irons. Two types of cast iron used extensively in water pipes are grey cast iron and ductile iron.

Grey Cast Iron. Grey cast iron has a characteristic grey colour which results from the graphite within the metal crystallized as flakes as seen in Figure 4.1. The total carbon content of grey cast iron alloys generally ranges from 2.5 to 3.6 %. The shape, size, amount, and distribution of the flakes vary between different grey cast irons. The cooling rate during the manufacture process has significant influence on flake morphology. Moderate cooling rates generally produce grey cast irons with the best mechanical properties (graphite flakes with uniform distribution and random orientation). The matrix of grey cast iron generally occurs in three common phases: ferrite, cementite, and pearlite. Ferrite is a softer phase consisting of nearly pure iron (low carbon content). Cementite is a harder phase composed of an intermetallic compound of iron and carbon. Pearlite is the most common matrix phase in grey cast irons and is characterized by lamellar plates of ferrite and cementite (Davis 2006).

Ductile Iron. Ductile iron has higher ductility relative to other cast irons; it contains graphite in spheroidal nodules as seen in Figure 4.1. This nodule formation is the result of certain additives (commonly magnesium) introduced to the molten iron during manufacturing. Their total carbon content generally ranges from 3.6 to 3.8 % and the magnesium content from 0.03 to 0.06 % (no magnesium in grey cast iron). The shape of the nodules can vary from flake form to true nodular form. Ductile iron commonly has more than 90 % of the graphite in nodular form (90% nodularity). The size and uniformity of distribution also vary between different ductile irons. Spheroidal graphite is less affected by cooling rate than graphite flakes. The most common matrix phases in ductile irons are ferrite and pearlite or varying proportions of the two (Davis 1996).

Differences in physical and mechanical properties of cast irons arise from their varying microstructures. The shape of graphite in cast irons is the single most important factor affecting their mechanical properties. Typical values of elastic modulus, tensile strength, and elongation for grey cast irons are 65 to 160 GPa, 150 to 430 MPa, and 0.5 to 1.0 %, respectively. Typical values of elastic modulus, tensile strength, and elongation for ductile irons are 170 to 175 GPa, 350 to 900 MPa, and 1.0 to 18.0 %, respectively (Davis 1996). The graphite flakes in grey cast iron act as stress concentrators; the sharpness of the graphite cavities increase internal stresses upon loading generating its characteristic brittle behaviour. These discontinuities are responsible for the lower strength in grey cast iron relative to ductile iron. Increasing the carbon content increases the amount of graphite and thus reduces the strength of cast iron. Higher tensile strengths and elastic moduli are attributed smaller flakes. Furthermore, uniform as opposed to segregated flake distribution result in better mechanical properties (Davis 1996, Angus 1976). The matrix composition also affects the mechanical properties: ferrite has low strength and high ductility, cementite has high strength and brittle behaviour and pearlite has hardness and strength intermediary to those of ferrite and cementite (Davis 2006).

The occurrence of graphite in ductile iron as nodules increases the strength of the metal by up to seven times in comparison with grey cast iron and dramatically improves ductility. All properties related to strength and ductility decrease as the proportion of non-nodular graphite within a ductile iron increases. The size and distribution of graphite nodules also affect the properties. Many small nodules tend to increase tensile properties. Excessive nodules may weaken a metal. As the amount of graphite in a metal increases, there is a relatively small decrease in the strength, modulus of elasticity and elongation. The matrix of ductile irons generally consists of varying proportions of ferrite and pearlite. The strength and hardness of an iron increases as the amount of pearlite increases (Davis 1996).

Various studies examining the mechanical properties of exhumed cast iron pipe are present in the literature (Seica and Packer 2004, Rajani 2000, Conlin and Baker 1991). None of these papers evaluate of the relationships between ultrasonic testing results and mechanical properties for cast iron water pipes. Ultrasonic testing is generally used in wall thickness measurements and corrosion detections in exhumed pipes and pipes still in service (Rajani 2000, Skabo and Jackson 1991). However, relationships between ultrasonic properties and mechanical characteristics for other forms of casted irons have been evaluated in various studies. The following sections summarize two such papers which use methods and present information applicable to the current study.

4.1.1 Evaluation of Cast Iron Structure by Ultrasonic Frequency Analysis

Onozawa and Ohira (1990) used ultrasonic frequency analysis in the evaluation of different cast irons. This paper was the only study found in the literature that considered the frequency domain of ultrasonic tests on cast iron. Ultrasonic measurements were done on grey cast iron and ductile iron.

4.1.1.1 *Methodology and Setup*

The cast iron samples were manufactured specifically for this study with carefully controlled chemical compositions. These samples included one ductile iron specimen, one compacted vermicular iron (intermediary between grey cast iron and ductile iron with thick graphite flakes) and four grey cast iron specimens with varying carbon content and size of graphite flakes. The changes in microstructure between samples were created through alterations in the melt composition. An ultrasonic pulse velocity testing apparatus, similar to that shown in Figure 3.1, was used to measure s-wave velocity and analyze the frequency of the recorded signals. The resonant frequency of a sample was taken as the frequency of the main peak in the observed Fourier magnitude frequency spectrum. The ultrasonic transducers used operated between 1 and 5 MHz in a transverse wave mode (s-waves). No detail is given about the size or shape of the samples tested. Average shape coefficients (K) were calculated according to measurement taken from microscopic images of the different samples. The formula used to calculate K is given by

$$K = 4\pi \frac{A}{P^2} \qquad [4.1]$$

where A is the acerage surface area of graphite flakes or nodules and P is the average peripheral length of the graphite flakes or nodules. This coefficient gives a measure of how much graphite is in nodular form. Ductile iron had highest value, compacted vermicular had the next highest, then grey cast irons had increasing K values as their corresponding graphite flakes because thicker or shorter and approached the shape of nodules.

4.1.1.2 *Summary of Results and Main Conclusions*

When comparing the frequency content between ultrasonic measurements on the ductile iron and grey cast iron, the ductile iron had a higher resonant frequency than the grey cast iron. In addition, the grey cast iron sample showed greater attenuation of high frequencies than the ductile iron; the graphite flakes in grey cast iron have a greater scattering effect on the wave energy than the nodules in ductile iron. The ultrasonic velocity and resonant frequency showed a linear relationship. The grey cast iron samples had s-wave velocities (V_S) ranging between 4100 and 4750 m/s, compacted vermicular iron had a V_S of about

5300 m/s, and the ductile iron had a V_S of about 5400 m/s. The relationship between K and ultrasonic velocity presented by the authors is shown in Figure 4.2. This comparison showed linear relationships in two regions. The first region was below V_S of about 5000 m/s where a linear relationship with almost perfect correlation was seen between V_S and K for the four cast iron samples. The second region occurred above 5000 m/s where the compacted vermicular iron and ductile iron data points formed a linear relationship with a greater slope than seen in the grey cast iron region. From these very good correlations, Onozawa and Ohira (1990) concluded that ultrasonic testing is a highly effective method of evaluating the quality of cast irons.

4.1.1.3 *Details Applicable to Current Study*

This study presents the applicability of ultrasonic testing for the evaluation of the quality of cast iron. Changes in carbon shape leading to weaknesses within a pipe could possibly be detected through changes in ultrasonic velocity or ultrasonic signal frequency content. Furthermore, it shows that relationships of ultrasonic velocity with other properties occur in two regions: one for grey cast irons and another for ductile irons. For the evaluation of cast iron water pipes, any correlations must be made separately according to these two materials. Finally, expected ranges of ultrasonic velocities for cast irons are presented. Upon closer examination, it is most likely that the velocities reported are actually p-wave velocities. Converting the reported grey cast iron V_S range (4100 to 4750 m/s) using a Poisson's ratio of 0.25 (Angus 1976) and Eq. 2.6 (Eq. 2.6 simplifies to $V_P = 1.69\ V_S$) to p-wave velocity (V_P) indicates a range from about 6930 to 8030 m/s. Other sources in the literature indicate maximum V_P of grey cast iron around 5500 m/s. It was concluded that the V_S values reported by Onozawa and Ohira (1989) were actually V_P. Finally, a range of 1 to 5 MHz ultrasonic transducers is presented as possible frequencies to be used in the current study. Using the a range in velocity from 4100 to 5400 m/s and frequency range from 1 to 5 MHz, the wavelengths obtained in the ultrasonic testing were between 5.4 mm and 0.8 mm; similar wavelengths should be able to evaluate correlations in the cast iron pipe samples.

4.1.2 Evaluation of mechanical properties of cast iron by ultrasonic velocity

Ohide et al. (1989) used ultrasonic testing to evaluate microstructure and mechanical properties of cast irons. Microstructure examination and ultrasonic and tensile testing were done on samples of grey cast iron and ductile iron.

4.1.2.1 Methodology and Setup

Cast iron samples were manufactured specifically for this study. Both grey cast iron and ductile cast iron samples varied mainly in the amount of carbon present in the alloy and shape coefficient. The changes in microstructure between samples were created through alterations in the melt composition. The variation in carbon content was measured as the percentage of area occurring as graphite on a polished sample measured through microscopic analysis. The ultrasonic testing was done on rectangular test bars of unknown dimensions machined from the cast blocks. These rectangular bars were further machined to obtain specimens of 80 mm in length and 7 mm in diameter for the tensile testing. Ultrasonic velocities were obtained using a thickness measuring device. This setup has a single longitudinal, p-wave generating transducer that measures reflections within the sample. Transducer frequencies of 5 and 10 MHz were used.

4.1.2.2 Summary of Results and Main Conclusions

The relationship observed between ultrasonic velocity and graphite area is presented in Figure 4.3a. Two separate linear trends are observed: one for the grey cast irons samples and one for the ductile iron samples. For both cast iron types, V_P decreases with increasing carbon content. The velocity of graphite is significantly less than in pure iron. Therefore, as the percentage carbon increases, the more graphite a wave must travel through and the greater reduction in velocity occurs. The relationship between V_P and graphite area showed very good correlation for grey cast iron samples while more scatter was seen in the relationship for the ductile iron samples. The trends observed between V_P and tensile strength is presented in Figure 4.3b. Again, two separate linear relationships are observed for the different cast iron types samples. Both trends show an increase in tensile strength with velocity. As observed in Figure 4.3a, velocity is related to graphite content. Graphite is significantly weaker than the nearly pure iron matrix; decreases in graphite content result in increases in strength. Consequently, as the graphite content decreases the velocity increases and so does the strength. Furthermore, the sharp corners of the graphite flakes in grey cast iron act as stress concentrators. The nodular graphite in ductile iron does not have the same effect. This effect may explain why the relationship between V_P and tensile strength has a greater slope for grey cast iron samples than ductile iron as observed in Figure 4.3b. The change in graphite content measured by the wave velocity has a greater effect on the strength in grey cast iron because of the increase or decrease in stress-concentrators. The V_P reported for grey cast iron varied from about 3900 to 5400 m/s and from about 5400 to 5700 m/s for ductile iron. The measured tensile strengths varied from about 15 to 35 kgf/mm^2 (147 to 343 MPa) for grey cast iron and from about 45 to 55 kgf/mm^2 (441 to 539 MPa) for ductile irons. The authors concluded that cast iron microstructure can be quantitatively evaluated through ultrasonic velocity measurements provided that the manufacturing history of the iron is known.

4.1.2.3 Details Applicable to Current Study

The two separate linear trends observed in Figures 4.3a and 4.3b further support examining relationships between ultrasonic measurements and mechanical properties of grey cast iron and ductile iron separately. Furthermore, the observed linear relationship between ultrasonic velocity and tensile strength indicate that changes in velocity could potentially be used to detect changes in strength in cast iron water pipes. Ranges for velocity and tensile strength in grey cast iron and ductile iron are presented. Finally, the lack of reference to any frequency analysis of the ultrasonic tests conducted in this study provides rational for evaluation of the effects of changes in cast iron properties on the frequency content of ultrasonic signals.

4.2 Literature Review of Geophysical Methods Used for Site Investigation

Geophysical methods have become very useful tools for geotechnical site investigations due to recent technological advancements in data collection and acquisition equipment and development of new analysis software. For example, the MASW method was developed by the Kansas Geological Survey in 1999 (Park et al. 1999). Applications of these methods in shallow soil investigations are common in the literature. The following three sections summarize studies performed using various geophysical methods for stratigraphy delineation in shallow soils. These summaries provide insight into the performance of these methods in different environments, the equipment and procedures used in their application, data analysis and interpretation techniques, and discussion of advantages and limitations. These details provide useful background information for the current study.

4.2.1 A Comparison of Geophysical Methods at a River Terrace Site

Hirsch et al. (2008) performed a geophysical investigation at a future site for a waste water treatment facility near Calgary, Alberta. The site is located on the bank of the Bow River to the south of the city. The subsurface on-site consists mainly of river deposited sands and gravels with finer-grained overbank and lacustrine deposits in some areas. The site is underlain by shale bedrock with a weathered upper boundary occurring at depths from 2.5 m to 8.5 m with an average of 5.5 m below the ground surface. The groundwater across the site generally occurred about one metre above the bedrock.

Three geophysical methods were used in the study: ground penetrating radar (GPR), ERI, and SR. GPR is a high resolution (cm to sub-cm wavelengths) nondestructive method that uses short radar pulses. Pulses are sent from the surface using an antenna. Changes in dielectric permittivity associated with changes in soil texture and moisture content create reflections. Measurements are made a long a line to obtain a profile of reflectors. One of the principal limitations of GPR is strong attenuation of pulses in electrical conductive materials such as clays and wet sediments. This limitation negates the use of GPR for the site studied in this thesis due to the high clay content across the site. For this reason, only the ERI and SR results from this study are discussed.

4.2.1.1 Methodology and Setup

The geophysical surveys were completed along two lines. The ERI survey was completed with a 56 electrode array. A switching box system was used that automatically cycled through different electrode locations and spacings to create a profile along the measurement line. A Wenner electrode configuration was used. The ERI surveys were completed with 2-m and 4-m electrode spaced arrays. The data were inverted using a smoothness-constrained least-squares method. The SR survey was completed with a 60 geophone array with a geophone spacing of 2 m. The geophones were buried in shallow holes to reduce noise from the wind. A 16-pound sledgehammer and a metal plate were used as a source. For each 118 m line, five shots were recorded at -1, 29, 59, 89, 119 m. Eight boreholes (four on each line) were advanced to verify the results of the geophysical methods.

4.2.1.2 Summary of Results and Main Conclusions

The ERI survey provided information to a depth of about 15 m across the site. This method was the most effective in differentiating the stratigraphic units. High resistivity gravel overlying the low resistivity bedrock was identified in the resistivity profiles. The depth to the bottom of the gravel was not exactly located in all the profiles because of blurring of the transition caused by the smoothing constraint used in the inversion algorithm. Interruption of the gravel layer by lower resistivity silt deposited from the adjacent upland and over bank deposits from the river was also observed in the profiles. The SR survey identified two refracting boundaries across the site: a shallow refractor ranging in depth from about 1.0 to 2.0 m and a deeper refractor consistent with the depth of the bedrock (ranging from 2.5 to 8.5 m below surface). The velocities of the different layers were consistent across the site: the top layer had a velocity ranging from 200 to 330 m/s; the second layer (within the gravel unit) velocity ranged from 540 to 770 m/s, and the bottom refractor (taken as the bedrock) had a velocity ranging from 3800 and 4100 m/s. The upper-most layer was not present in the ERI profiles. This layer was required in the velocity model to allow convergence of the inversion. It is theorized that this boundary may be the result of an increase in velocity with depth with little change in change in resistivity. The SR survey was less effective than the ERI in delineating the upland and overbank deposits due to either small contrast in the velocities between the materials at these sections or changes in the geology too rapid for accurate prediction by the inversion algorithm. The authors concluded that combining the results of the different methods with the borehole data gave a high resolution interpretation of the subsurface across the site.

4.2.1.3 Details Applicable to Current Study

Previous studies in the area of the site being investigated for the current study suggest the presence of soft compressible soils underlain by hard sandy glacial till. Contrast in electrical resistivity and stiffness and thus velocity of such materials present both ERI and SR as ideal geophysical methods for this study. The depth of penetration for this study will be no greater than that reported by Hirsch et al. (2008) (about 15 m); therefore, the electrode and geophone spacing used in their study are applicable: two and four m spacing for electrodes and two m spacing for geophones. Finally, a sledgehammer as a source and required source-receiver offsets presented can be considered.

4.2.2 In situ shear wave velocity from multichannel analysis of surface waves (MASW) tests at eight Norwegian research sites

Long and Donohue (2007) conducted MASW tests on eight sites with the goal of assessing the repeatability, accuracy, and reliability of this method for use in engineering studies. The test sites were located in Norway. These locations presented a variety of soils for testing the MASW method: five sites were underlain by soft to firm homogeneous clay, two by silty material, and the final site by loose to medium-dense sand. These materials were generally homogenous to the depth of penetration of the MASW surveys. The site names and corresponding soil types are presented in Table 4.1. All of these sites have been well-characterized from previous investigations. MASW data was inverted to generate profiles showing the change in shear-wave velocity (V_S) with depth. Seismic cone penetration test (SPCT), cone penetration test (CPT), and cross-hole seismic test results from these studies were used to verify the results of the MASW surveys.

4.2.2.1 Methodology and Setup

A sledgehammer was used as a source in all the surveys. Multiple surveys spaced at least one metre apart were conducted at each site to test the repeatability of the results. The data was collected using a RAS-24 seismograph. Either 10 Hz or 4.5 Hz geophones were used. The 4.5 Hz were generally used on the sites with the softest soils to better detect low frequency energy. However, it was found that there was no significant difference in the limit of low frequency measurements between the two types of geophones: the 10 Hz and 4.5 geophones could detect signals as low as 5 Hz and 2 to 3Hz, respectively. A variety of survey conditions were used as shown in Table 4.1.

4.2.2.2 Summary of Results and Main Conclusions

Clay Sites. The MASW surveys showed consistency and repeatability in the inverted profiles for each of the clay sites. Scatter between profiles was observed to increase with depths below about 8 m indicating better resolution at shallower depths. The MASW profiles agreed very well with SPCT, CPT, and cross-hole seismic data collected in previous independent studies. At two separate locations, the MASW profiles detected velocity inversion zones (decrease in velocity with depth) that were also presented in SCPT data. The MASW analyses at the clay sites reported V_S ranging from about 80 to 150 m/s at surface and increasing to about 120 to 325 m/s at depth (~8 m).

Silt Sites. The MASW profiles from the Os site were highly repeatable. The profiles from Halsen showed similar results but had maximum differences of 25 m/s. This discrepancy is attributed to the heterogeneity in the silt underlying the site. Only CPT data were available from previous studies at these sites. These measurements had to be converted into V_S values by empirical relationships for comparison with the MASW results. Generally trends in these data sets were similar. However, V_S values converted from CPT and those predicted from the MASW analyses for the silt site did not agree as well as was seen between MASW and previous V_S measurements in the clays. These differences were explained by the fact that the empirical equations used to convert the CPT data to V_S were developed for intact clays not silts. The MASW analyses at the silt sites reported V_S ranging from about 70 to 120 m/s at the surface and increasing to about 120 to 325 m/s at depth (~10 m).

Sand Site. Only one MASW survey was completed at the sand site. The resulting V_S profile values are higher than those reported in SCPT and cross-hole tests from previous studies. The site of the original studies had since been extensively developed. As a result, the MASW survey was located about 30 m from other tests and closer to the zone of influence of some large grain silos. The different testing location may have contributed to the different results. The MASW analyses at the sand site reported V_S ranging from about 140 m/s at the surface and increasing to about 180 m/s at depth (~10 m). Long and

Donohue (2007) concluded that the MASW method was easy and efficient and gave consistent and repeatable results.

4.2.2.3 Details Applicable to Current Study

The above summarized study presents MASW as a third applicable geophysical method for the current study. This method is shown to be very successful in clays and silts. Although the authors reported less success in sands, there was less data available for this site and spatial variability may explain the observed shortcomings. One important result observed in this summarized study was the detection of the slight velocity inversion (decrease in V_S by about 10 m/s from one layer to the next deepest layer) also observed from the CPT results at two of the clay sites. A stiff sandy layer overlying a relatively softer layer has been identified at the site of the current study. Because seismic refraction surveys are unable to detect velocity reversals, the ability of the MASW survey to resolve this boundary will add to the results of the current study. Although reasons for the decrease in resolution with depth seen in the MASW results are not discussed by the authors, other literature discusses this phenomenon as one of the limitations of this method. The resolution of deeper layers is obtained from large wavelength (and thus low frequency) surface wave energy that penetrates to these depths. It can be difficult to generate the required low frequencies with enough energy to achieve these depths from the surface. If soft layers exist near surface, these can attenuate wave energy further impacting the penetration depth and depth resolution. The importance of selecting an appropriate source is apparent from these findings. Finally, the above summarized study presents some expected s-wave velocities for shallow soils similar to those found on the current study site.

4.2.3 The Use of Multichannel Analysis of Surface Waves in Determining Gmax for Soft Clay

Donohue et al. (2004) verified the results of MASW surveys in soft, stratified clays deposited from glacial lakes during the last ice-age. Testing was done at two sites in Ireland: Athlone and Portumna. The stratigraphy investigated at Athlone consisted of a surficial 2 m layer of soft peats underlain by a 4 m layer of grey organic clay followed by a lower 7 m layer of brown laminated clay. The stratigraphy investigated at Portumna consisted of and upper 2.5 m of soft peats underlain by a 4.5 m clay layer, underlain by another 3 m of clay. The lower clay layers at both sites were underlain by glacial till. The MASW survey results were compared to CPT data collected in previous studies. The authors also used output from a numerical model to evaluate the performance of the inversion software Surfseis in resolving data collected from a multi-layered medium. Surfseis is a MASW data inversion software that uses an inversion algorithm common to most MASW analysis software packages.

4.2.3.1 Methodology and Setup

A sledgehammer was used to generate the surface waves. An array of twelve 4.5 Hz geophones with one-metre spacing was used for all surveys. Data was collected for source offsets of 1, 6, 13, and 25m to determine optimum acquisition. Three surveys were completed at Athlone and two surveys were performed at Portumna to test the repeatability of the MASW surveys. Survey lines at each site were parallel and separated by 2 m.

The numerical model used in the Surfseis verification was the Discrete Particle Scheme (DPS). This synthetic earth representation consisted of interacting particles arranged in a closely packed isotropic hexagonal configuration. The DPS had a fixed value for Poisson's ratio of 0.25 and uses particle density, diameter, and p-wave velocity as user inputs. Variations in parameters can be inputted to simulate changes in stratigraphy. A source and receivers were created on the uppermost layer of particles. The model outputted a seismogram that could then be inverted using Surfseis. Two different 4-layer models were considered simulating the complete stratigraphy at the Athlone and Portumna sites. These models showed sharper changes in velocity between layers instead of the gradual changes generally seen in the field. In the second model, seismographs using both 7 Hz and 12 Hz source energy were generated.

4.2.3.2 Summary of Results and Main Conclusions

In such soft soils, surveys at both locations penetrated to about 9 m. The V_S profiles obtained from the MASW surveys were converted to shear modulus (G) according to Eq. 2.5. The cone tip resistance measurements form the CPT tests were also converted to G using empirical relationships. The G_S profiles obtained from both methods were compared. Profiles from surveys taken at the same site generally showed very good agreement with slight increases in variations with depth. MASW profiles from both sites agreed very well with the corresponding CPT profiles also showing slightly increased differences at depth (G_S and thus V_S slightly underestimated in deep layer at both sites). The boundary between the upper peat layer and first clay layer was clearly defined at both sites by the MASW results. The boundary between the clay units at both sites was less apparent in the MASW profiles because of the gradual increase in velocity with depth observed across this interface in the CPT data. Values of V_S reported in the clays by the MASW surveys ranged from 30 m/s near surface to 85 m/s at depths around 8 m.

The results from the inversion of the DPS output with Surfseis agreed well with the model inputs. The sharp layer boundaries were well-defined in the MASW profile near surface and became slightly less precise with depth. The Surfseis inversion showed the 7 Hz source penetrated to 15 m while the 15 Hz source penetrated to only 7.5m. This result illustrates the effect of source frequency content on penetration depth.

The authors of this study concluded that MASW survey produced repeatable results that corresponded very well with previously collected CPT data at both sites. They further stated that the depth of penetration of the surveys was limited to 9 m which could be increased using lower frequency geophones with wider geophone spacing or a longer array.

4.2.3.3 Details Applicable to Current Study

The above summarized study demonstrates the applicability of the MASW method to layered media thus further supporting its use in the current study. The ability to detect sharp changes in V_S as demonstrated in the results makes this a promising choice for the current study as both soft clay layers and relatively stiffer sandy till materials have been identified at the site.

Table 4.1: MASW survey configurations

Site Name	Soil Type	Survey Config. No.	No. of Geophones	Geophone Spacing (m)	Geophone Freq. (Hz)	Source-Receiver Offset (m)	Depth of Penetration (m)
Onsoy	soft clay	1	24	1.0	10.0	0, 2, 4	16.2
		2	12	1.0	4.5	0, 2, 4	12.3
Museum Park	soft clay	1	24	1.0	10.0	0, 2	10.6
Danvikgata	soft clay	1	24	1.0	10.0	0, 2	10.4
Eberg	firm clay	1	12	1	4.5	0, 2, 4, 8	10.3
		2	12	1	4.5	0, 2, 3, 5	12.5
		3	12	1.5	4.5	0, 2	11.1
Glava	firm clay	1	24	1.0	10.0	0, 2	14.3
Halsen	silt	1	24	1.0	10.0	0, 2	10.4
Os-Skeisleira	silt	1	24	1.0	10.0	0, 2	14.3
Holmen Island	sand	1	24	1.0	10.0	0, 2	12.5

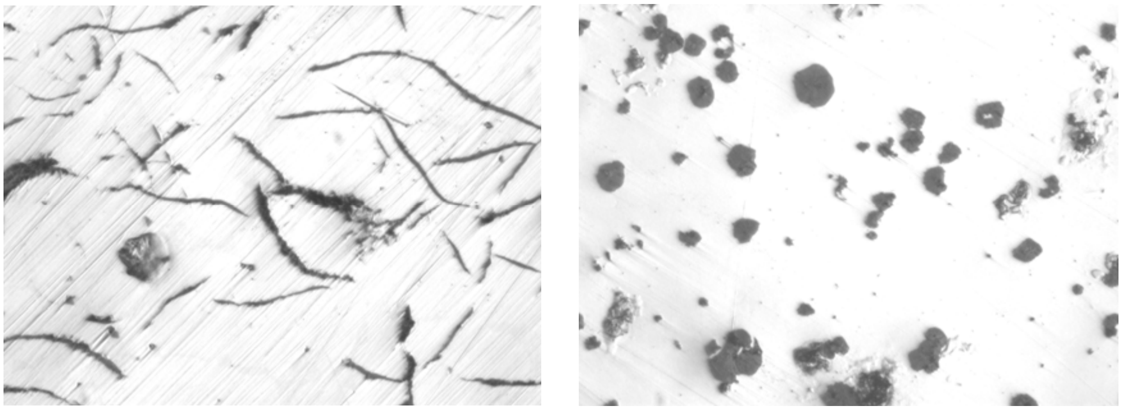

Graphite flakes in grey cast iron

Graphite nodules in ductile iron

Figure 4.1: Grey cast iron and ductile iron microstructures

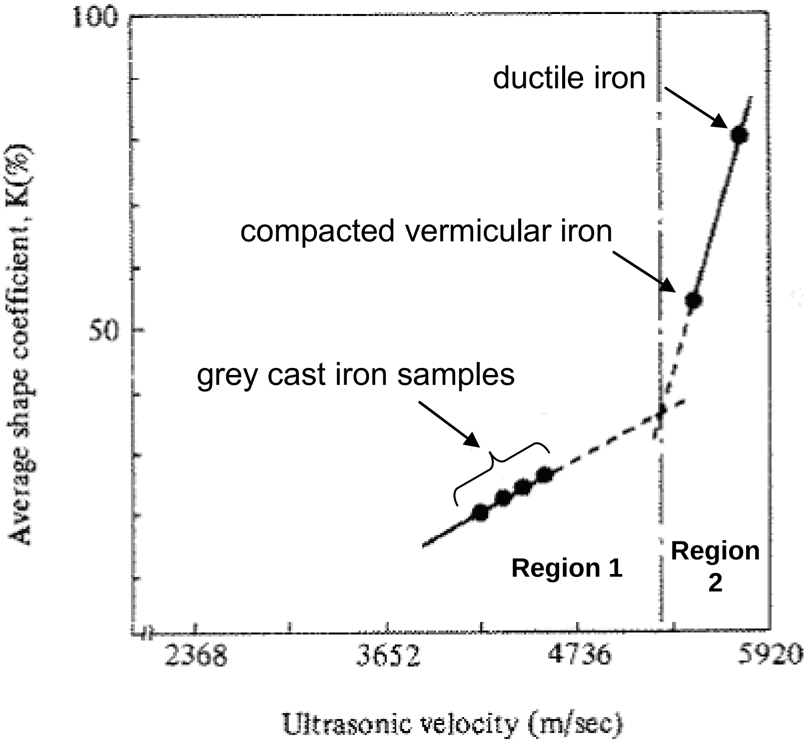

Figure 4.2: Average shape coefficient versus ultrasonic velocity (Onozawa and Ohira 1989)

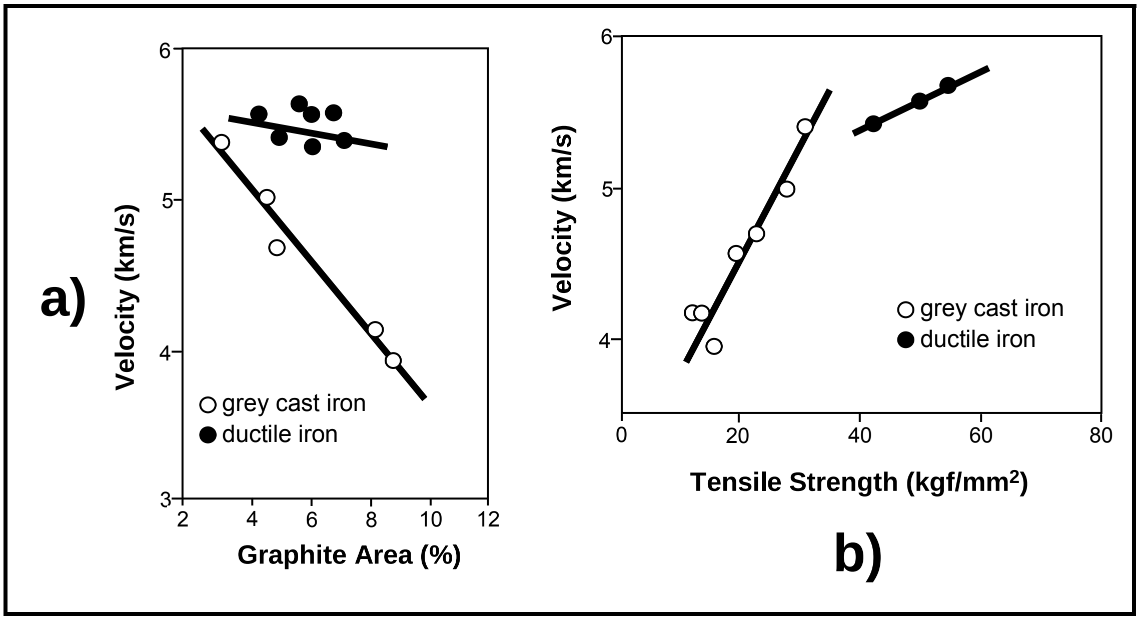

Figure 4.3: Ultrasonic velocity versus a) graphite area and b) tensile strength (Ohide et al. 1989)

CHAPTER 5: ULTRASONIC CHARACTERIZATION OF EXHUMED CAST IRON WATER PIPES

5.1 Background

Grey cast iron pipes were used extensively in the construction of water distribution networks from the end of the nineteenth century until the late 1940s. Subsequently, the superior mechanical properties of ductile iron pipe became preferred. Throughout this period a variety of manufacturing technologies were used. As a result, cast iron pipes with varying compositions and ages exist today. Many of these pipes remain in service worldwide in old cities. For example, the average age of the water distribution system in the City of Toronto is 90 years. This network is comprised of approximately 5347 km of predominantly small diameter (100 to 300 mm) cast iron piping. The occurrence of breaks in these aging pipes is estimated as 2 per week (Seica and Packer 2004). With the increasing age and state of deterioration of cast iron pipes, an increase in the frequency of leaks and breaks can be expected to create more problems for water utility managers. Insight into the state of deterioration and structural condition of aging pipes can be advantageous in developing preventative and mitigation strategies for these frequent failures.

Nondestructive testing methods such as ultrasonic testing are commonly used for quality assessment of manufactured metals. Ultrasonic methods have applied in wall thickness measurements for corrosion detection in cast iron pipes still in service (Skabo and Jackson 1991). Furthermore, relationships between ultrasonic velocity and microscopic properties of cast irons, such as percent carbon content, nodularity, and matrix composition, have been established in various studies (Tamburelli and Quaroni 1975; Orlowicz et al. 2010). The analysis of mechanical properties of exhumed cast iron pipes has been used in various studies to evaluate their state of deterioration (Rajani 2000, Seica and Packer 2004). These studies generally focus primarily on large strain mechanical properties such as tensile and flexural strength. They make limited use of ultrasonic testing only for mapping corrosion through pipe thickness measurements.

Ohide et al. (1989) showed very good linear relationships between ultrasonic velocity and tensile strength among other mechanical properties for grey and ductile cast irons of varying grade. Samples of cast iron varied in amount of graphite and samples of ductile iron varied in amount of graphite and nodularity. Good linear relationships were observed between ultrasonic velocity and tensile strength for both grey and ductile irons when each different iron type was evaluated individually. The ductile samples had an average tensile strength about two times that of the grey cast iron samples and a greater standard deviation. In addition, the average ultrasonic velocity for the ductile samples was slightly greater than the average velocity of the grey iron samples. As a result, evaluating the relationship between velocity and strength for grey cast iron and ductile iron together does not give one trend but two linear relationships. Ohide et al. (1989) concluded that cast iron structure can be quantitatively assessed by measuring ultrasonic velocity provided that the manufacturing history of the iron is known.

Fuller et al. (1990) and Collins and Alchekh (1995) observed similar relationships between velocity and tensile strength for samples of ductile iron. Both of these studies showed some non-linearity in the trends from samples with high velocity and strength. In all of the above mentioned studies, the manufacturing of the cast iron being tested is always carefully controlled and test specimens are machined with precise dimensions. In addition, not much consideration is given to frequency content of the ultrasonic energy or the impacts of specimen geometry on the results of ultrasonic testing.

This chapter investigates the use of ultrasonic testing to provide insight into the structural integrity of exhumed cast iron water pipes. Non-destructive and destructive testing programs were performed on eight cast iron pipes ranging in service life from about 30 to 130 years. The pipes originated from different manufacturing materials and methods and had various diameters, wall thicknesses, and states of corrosion. The experimental program included microstructure examination, small strain measurements with ultrasonic testing and large strain measurements with tensile and flexural testing. The ultrasonic data analysis is performed not only in the time domain as traditionally done in ultrasonic testing but also in the frequency domain using the Fourier and the wavelet transforms.

The effect of Lamb wave propagation in the pipe samples on the recorded ultrasonic signals is evaluated. This kind of surface wave is rarely considered in the literature when presenting ultrasonic results. The relationship between the large strain and small strain properties of cast iron used in water pipes is investigated.

5.2 Experimental Methodology

A laboratory-testing program was designed to measure the small strain and large strain properties of eight sections of exhumed cast iron pipes. The measurement of small strain parameters involved ultrasonic pulse velocity testing. The large strain measurements included tensile testing and flexural testing. A summary of the pipe sections tested is presented in Table 5.1. The wall thickness and relative conditions varied between the pipes. Average pipe-wall thickness and corrosion depth for each pipe is presented in Table 5.1. The sections of pipe varied in length from 47 to 110 cm. These sections were first cut into lengthwise strips. Ultrasonic measurements were done on these initial full-length strips. Smaller coupons (about 20 cm length) were cut longitudinally from these strips with a water jet for the various lab tests. Representative samples were prepared and examined with an optical microscope to evaluate microstructure. Ultrasonic measurements were also performed on all the 20-cm coupons before the large-strain testing. Measurements on each coupon permitted the observation of changes in wave properties and large-strain properties within individual pipes and allowed for the assessment of any correlations between these measured parameters. Tensile testing was performed on coupons from all pipes while flexural testing was done on samples from only pipes 4A, 4B, 4C, 6A and 12A. Flexural testing was not performed on the 18-inch pipes because of a limited amount of material available.

5.3 Experimental Setup and Testing Procedures

Microstructure Evaluation. Representative samples from each pipe were polished and digitally photographed at varying levels of magnification. A general assessment of the microstructure of the pipes was required, thus the ASTM procedures for preparing metal samples for microstructure analysis were followed only partially. Consequently, some striations are visible in the microstructure pictures presented in later sections.

Ultrasonic Pulse Velocity Test. Ultrasonic testing was conducted on lengthwise strips cut from the pipes and all samples cut for the tensile and flexural testing. The dimensions of these samples are presented in the following sections. The instrumentation used for ultrasonic testing consists of two compressional-wave (p-wave) piezoelectric transducers (1 MHz, Panametrics V102-RM), a pulse generator (Panametric Pulser Receiver Model 5052PR), a digital oscilloscope (HP 54610B), a sample mounting frame, a load cell (type 50 DBB, capacity 500 N), a power supply (HP 3620 A), a digital multimeter (HP 34401 A), and a computer. For each test, a sample was mounted between the two transducers on the frame equipped with the load cell. Vacuum grease was used as ultrasonic couplant between sample and transducers. The load cell output was monitored with the digital multimeter to measure the pressure applied on the transducers. A constant pressure of about 150 kPa was maintained in all tests to improve the repeatability of the results.

The travel time between the transducers was measured with the digital oscilloscope (resolution $\Delta t = 0.01\ \mu s$). The p-wave velocity was determined by dividing the sample length by the travel time. The complete time history of the arriving wave was transferred to the computer using a GPIB interface (resolution $\Delta t = 0.1\ \mu s$) for later signal processing. The ultrasonic equipment was calibrated by measuring the travel time on a series of steel samples of different length following the procedure suggested by Khan et al. (2010). The measured arrival times are plotted against the corresponding sample length and a line of best fit is evaluated. The line intercept represents the inherent time delay for the system (0.4 μs) which is subtracted from all the arrival times recorded in this study.

Tensile Test. Tensile tests were performed following to the ASTM standard E8 (ASTM E8/E8M-08 2008). Tensile coupons were cut according to the sheet-type, ½-in wide specifications. These dogbone-shaped samples were 20 cm long with a reduced section of 1.3 cm width, and grip sections on either side of 5.7 cm long. The thicknesses of the coupons were the same as the wall-thickness of the original pipe. Some coupons required machining to provide flat gripping areas to prevent breakage at the hydraulic grips. The testing equipment included a hydraulic load frame and hydraulic grips (MTS Model 322 for 18 in diameter pipes, MTS Model 810 for other pipes), a digital extensometer (MTS Model 634.25E-24 with 2 in gage length), and a data acquisition system. All tensile testing was performed at a constant strain rate of 0.5 mm/min. The coupons were loaded until failure. Force data from the MTS machines and displacement data from the extensometer were transferred to the computer for later analysis.

Flexural Test. Flexural tests were performed following the ASTM standard D790. (ASTM D790-07 2007). The flexural samples were 22 cm long by 2.5 cm wide to accommodate the span length and width specified in the standard. The thicknesses of the coupons were the same as the wall-thickness of the original pipe section from which they were cut. The samples were tested on a hydraulic load frame (MTS Model 810) equipped with curved loading noses and supports which are changed to match the outer and inner curvatures of the different pipes. The samples are loaded to failure at a constant strain rate of 5 mm/min. Displacement data was measured with the built-in LVDT on the MTS machine. Force and displacement data from the MTS machine is transferred to the computer for later analysis.

5.4 Results

Microstructure Evaluation. Figure 5.1 presents pictures of the polished cast iron samples at 50 × magnification. Only one sample was taken to represent the 18 in diameter pipes as these were all made around the same time and at the same foundry and their microstructure is expected to be similar. Table 5.2 summarizes some general comments on the different microstructures observed.

Ultrasonic Pulse Velocity Testing. A typical time signal and the average frequency spectrum (average of all coupons from individual pipe) from each pipe are presented in Figures 5.2 and 5.3, respectively. The average p-wave velocity measurement from the long strips and from the short coupons for each pipe is presented in Table 5.3.

Tensile Testing. Typical tensile stress-strain curves from each pipe are illustrated in Figure 5.4. Large strain parameters obtained from tensile testing included elastic modulus, tensile strength and elongation. Tensile strength was taken as the maximum stress sustained by the test specimen while the elongation was measured as the strain at this maximum stress. The elastic modulus was measured from the initial tangent to the stress-strain curve (about 0.01 to 0.05 % strain). A summary of the parameters obtained from the tensile testing are presented in Table 5.4.

Flexural Testing. Typical flexural stress-strain curves from each pipe are illustrated in Figure 5.5. Large strain parameters obtained from flexural testing included flexural modulus, flexural strength and flexural elongation. Flexural strength was taken as the maximum stress sustained by the test specimen while the flexural elongation was measured as the strain at this maximum stress. The flexural modulus was measured from the initial tangent to the stress-strain curve (about 0.10 to 0.15 % strain). A summary of the parameters obtained from the flexural testing are presented in Table 5.5.

5.5 Analysis and Discussion

The correlations between the small-strain measurements from ultrasonic testing and the large-strain measurements from tensile and flexural testing are investigated. The Pearson product moment correlation coefficient ($-1 < r > 1$) is used to evaluate the linear relationship between various combinations of data sets. Abdel-Megeed suggests that five or more data points are required for accurate correlation coefficients (1984). The Pearson coefficient was preferred to the coefficient of determination (R^2) because it reflects the positive or negative nature of the linear trend in the data and the degree of correlation. Positive linear relationships between ultrasonic velocity and tensile have been established in the literature. Therefore positive correlations are expected between the ultrasonic wave properties and large-strain measurements examined in this study. For the purposes of this study, an r value of +0.6 or above is considered to indicate a relationship with reasonable correlation between data sets because of the inherent variability in the pipe samples (variation in pipe wall thickness and corrosion depths as seen in Table 5.1).

Correlation of P-Wave Velocity with Large Strain Parameters. A significant increase in average V_P measurements (up to 350 m/s) from the long strips to the short coupons is observed in Table 5.3. This change in velocity illustrates the effect of sample dimension on ultrasonic velocity measurements. The time measured in an ultrasonic velocity test originates from the arrival of the high frequency p-wave. A longer sample attenuates ultrasonic energy, especially higher frequencies, to a greater extent in comparison to a shorter sample because of the larger travel time. An attenuated p-wave arrival can be missed or not seen at all depending on the resolution of the testing equipment. As a result, the later arrival of s-waves or surface waves is measured therefore reporting a slower velocity.

The relationships between the p-wave velocity of each coupon from an individual pipe and the corresponding elastic modulus, tensile strength, tensile elongation, flexural modulus, flexural strength, and flexural elongation were evaluated. The r values calculated for the correlations between the p-wave velocity and these large-strain parameters are presented in Table 5.6. To give an appreciation for the data dispersion associated with specific r values, various correlations of p-wave velocity and elastic modulus are shown in Figure 5.6.

In general, the p-wave velocity and the large-strain parameters are not well correlated. Only 5 of the 39 comparisons presented in Table 5.6 have r values greater than 0.6. This lack of correlation may be caused by the variation in cross-sectional area due to manufacturing defects and corrosion observed in the coupons. The velocity of p-waves traveling through the body of a coupon will not be significantly impacted by shallow defects. However, reductions in cross-sectional area will affect the large stress and strain behaviour of the coupons. In addition, limited variation in carbon content and other microscopic properties between coupons may not be significant enough to be captured by the p-wave velocity. At a frequency of 1.0 MHz with an approximate velocity of 5000 m/s, the corresponding wavelength is 5 mm. The differences in microstructure between different coupons from one pipe are at least an order magnitude smaller than half this wavelength. Using a higher frequency source could improve such correlations. Higher frequencies will generate smaller wavelengths and therefore increase the resolution of the testing. However, depth of penetration and therefore length of sample are reduced with increased source frequency.

Better correlations of p-wave velocity with both moduli are observed than with the strengths and elongations. The ultimate strength and strain at failure are affected by cracks or corrosion that act as stress concentrators at the surfaces samples. As previously mentioned, p-waves velocity is not sensitive to shallow surficial defects. Considering the above mentioned and that the tensile modulus and flexural modulus were measured at lower strain levels (0.01 to 0.05 % and 0.05 to 0.10 % respectively) better correlation between the p-wave velocity and the moduli is expected than with strength and elongation.

With the exception of pipes 4A and 12A, the correlation of the p-wave velocity with the flexural modulus was generally than with the tensile modulus. A more accurate extensometer was used in the tensile testing and therefore better correlations with the tensile data were expected. Less data points in these flexural comparisons (only four coupons) than in most of the tensile comparisons may contribute to these higher r values.

Average values of velocity and large strain parameters from all tested coupons were used to evaluate global correlations between pipes. Correlations of average velocity with average elastic modulus, tensile strength, and elongation for each pipe are presented in Figure 5.7a, 5.7b, and 5.7c, respectively. The average is computed from the measured parameters from all coupons from one pipe. Two distinct groups of data points are seen in these figures: the ductile iron pipes have higher p-wave velocities and large strain parameters than the grey cast iron pipes. Figure 5.7 shows error bars indicating one standard deviation for velocity, modulus, strength and elongation measurements. The velocity measurements had significantly smaller standard deviations than the large strain measurements (in some cases, error bars are not seen in Figure 5.7 because these are smaller than the data point shapes). The velocity measurements show less scatter because they originate from very precise measurements of length and time while the stress and strain measurements were more influenced by the varying conditions of the coupons (geometry, thickness, and corrosions depth varies between coupons).

The literature has shown very good positive linear relationships between ultrasonic velocity and tensile strength in both grey cast irons and ductile irons. However, in these studies the specimens tested are carefully machined with uniform geometries. In addition, significant changes in microstructure (eg. matrix composition, percent carbon, nodularity) are induced through planned changes in the chemical composition and manufacturing process. Such successful correlations are not observed in Figure 5.7. These poor relationships between ultrasonic velocity and the large strain parameters may be again caused by effects of variations in pipe condition. Furthermore, the changes in microstructure between pipes may not be as significant as the changes in manufactured samples used in other studies. The large strain parameters presented in Figure 5.7 do show a general increase with p-wave velocity measurements for the brittle pipes but with significant scatter in the data points. Only the velocity and tensile strength showed a positive relationship in the ductile irons while elastic modulus and elongation decreased slightly with velocity. Specific r values were not evaluated for the global correlations because of the limited number of data points.

Correlation of Frequency Content with Large Strain Parameters

The frequency contents of the recorded ultrasonic signals were used as an indication of attenuation. It was hypothesized that samples with lower large-strain values resulting from higher carbon content would cause greater attenuation of the ultrasonic signals and that the frequency spectra would be more sensitive to these changes than the velocity measurements. The relationship between the total area of the FFT magnitude (|FFT|) frequency spectrum measured from each coupon in an individual pipe with the corresponding elastic modulus was evaluated. These showed low correlation.

An algorithm was then developed to examine correlations between specific areas within the |FFT| frequency spectra and the elastic moduli from each coupon for individual pipes. Five different areas with specific frequency bandwidths (15 kHz, 35 kHz, 40 kHz, 55 kHz, and 100 kHz) were selected based on the peaks and other areas of significant energy observed in the measured frequency spectra. For the spectrum from an individual coupon, the algorithm shifts the central frequency of the first bandwidth area from 0 to 1 MHz.

The result is a vector with a value of the bandwidth area at each corresponding central frequency as shown in Figure 5.8. This process is repeated to generate a vector of areas for each coupon from the same pipe. A correlation coefficient at a specific frequency is then obtained for the relationship between the bandwidth area centred at that frequency from each coupon spectrum and the elastic modulus of each coupon as shown in Figure 5.9. A vector containing the change in correlation coefficient with frequency is then plotted to show if good correlations exist and at what frequencies they occur as presented in Figure 5.10) The process is repeated for the remaining frequency area bandwidths which produced five vectors of correlation coefficient changing with central frequency as illustrated in Figure 5.11.

The algorithm was first used to evaluate the correlation between the unaltered frequency spectra collected during the ultrasonic testing and the elastic moduli from each individual coupon for all pipes. The reported correlation coefficient for each pipe was taken from the maximum peak where the 15, 35, and 45 kHz curves converged (eg. peak in coefficient curves at about 510 kHz in Figure 5.11). The 55 kHz and 100 kHz bandwidths were too wide to show any good correlations. The resulting r values are presented in Table 5.7. Good correlations were only observed in three of the pipes (4B, 12A, 18A). Various combinations of normalizing in both the time and frequency domains were attempted to remove any coupling effects from the |FFT| spectra. The best results came from normalizing each time signal to its maximum prior to performing the FFT. The resulting r values are shown in Table 5.7. The normalization improved the r values slightly for five pipes (4B, 4C, 6A, 18B, and 18C) and reduced r values for the remaining pipes (4A, 12A, 18A).

It is possible that better correlations between the frequency spectrum areas and E were not obtained because of interference by Lamb wave energy. This type of wave is rarely considered in ultrasonic studies presented in the literature. Lamb wave dispersion curves were generated for each pipe according to Eq. 5.4 to determine what ranges of the frequency spectra might originate from Lamb waves. The average p-wave velocity and average thickness of each pipe were used in the calculations. Typical dispersion curves for ductile iron and grey cast iron are presented in Figures 5.12a and 5.12b, respectively. Both the symmetric and anti-symmetric fundamental modes are plotted. The dispersion curves showed that the main frequency content from the time signals measured in all the pipes occurs in the dispersive frequency range for Lamb waves. Figure 5.12 shows that the average frequency spectra have main peaks in the lower frequency range where the symmetric and anti-symmetric mode phase velocities are changing with frequency (below 400 kHz in Figure 12a and below 250 kHz in Figure 12b). Lamb waves are geometrically dispersive; the dispersive range of frequencies depends mainly on the thickness of the sample. Thus, changes in the sample geometry generate variations in the measured wave velocities that are not related to differences in material properties.

The Wavelet transform was used to isolate p-wave energy with shorter wavelengths and exclude the higher amplitude Lamb wave energy especially in the lower frequency range. To the knowledge of the author of this study, this approach has not previously been applied to ultrasonic testing data for cast irons. Debauchies' discrete wavelet transform was used to decompose the time signals into different frequency levels. Figure 5.13 presents an example of a decomposed signal. Reconstructed time signals from each coupon from 1000, 500, 250, 125, and 62.5 kHz levels were extracted. Each signal was again normalized in the time domain and FFTs were completed. These frequency spectra were then analyzed using the shifting area algorithm. The best correlations came from the 500 kHz level time signals supporting the theory that the lower frequency Lamb waves do not show good correlation with material properties. The resulting r values are presented in Table 5.7. The wavelet analysis improved the r values for three pipes (4A, 4B, and 18B), reduced the r value for two pipes (6A and 12A) while the remaining r values changed very little in comparison to the original Fourier area comparison. Relationships between frequency spectra area and tensile strength and elongation were not completed because better correlations with these large-strain parameters controlled by surface defects than with relatively lower strain elastic moduli were not expected. The final results of the wavelet analysis showed improved correlations from the velocity analysis but still no consistent relationships between frequency spectrum areas and elastic modulus.

Table 5.1: Tested pipe sections

Pipe ID	Pipe Diam. (in.)	Manuf. Year	Service Location	Avg. Wall Thickness (mm)	CV[1]	Avg Corros. Thickness (mm)	CV	Comments
4A	4	1962	North Bay, ON	7.6	2%	none		inner cement liner
4B	4	1962	North Bay, ON	10.2	3%	2.4	40%	-
4C	4	1975	North Bay, ON	10.5	5%	none		-
6A	6	1970	North Bay, ON	9.0	10%	1.0[2]	46%	inner cement liner
12A	12	1976	North Bay, ON	6.6	9%	none		inner cement liner
18A	18	1860	Hamilton, ON	16.1	13%	2.7	74%	-
18B	18	1860	Hamilton, ON	16.5	7%	1.2	114%	-
18C	18	1860	Hamilton, ON	20.3	2%	2.8	35%	-

[1] coefficient of variance

[2] corrosion here refers to discolouration observed inside cement liner

Table 5.2: Microstructure general observations

Pipe No.	Graphite Shape	Distribution	Relative Size	Type of Cast Iron
4A	Nodules	Uniform	Large	Ductile
4B	Flakes	Segregated	Very Short	Grey
4C	Flakes	Uniform	Long	Grey
6A	Nodules	Uniform	Small	Ductile
12A	Nodules	Uniform	Large	Ductile
18B	Flakes	Uniform	Long	Grey

Table 5.3: P-wave velocity (V_P) measurements

	Strips			Coupons		
	Length	Avg V_P		Length	Avg V_P	
Pipe ID	(cm)	(m/s)	CV	(cm)	(m/s)	CV
4A	103.9	5195	0.4%	22.0	5545	0.3%
4B	81.1	4655	0.8%	22.0	4966	0.2%
4C	47.3	4642	1.1%	22.0	4743	2.9%
6A	109.8	5211	0.8%	22.0	5514	0.7%
12A	98.7	5223	0.7%	22.0	5549	0.9%
18A	-	-	-	20.0	4776	0.9%
18B	-	-	-	20.0	4892	1.3%
18C	-	-	-	20.0	4898	0.7%

Table 5.4: Tensile testing results

	No. of Coupons	Avg. Elastic Modulus		Avg. Tensile Strength		Avg. Elongation	
Pipe ID	Tested	(MPa)	CV	(MPa)	CV	(%)	CV
4A	12	153093	3%	356.6	5%	1.7	30%
4B	8	97856	10%	144.7	11%	0.2	13%
4C	3	88543	7%	121.5	9%	0.2	16%
6A	8	160091	7%	317.6	13%	2.2	29%
12A	9	150667	9%	334.5	12%	2.3	33%
18A	8	88921	9%	63.2	35%	0.1	42%
18B	5	91900	17%	76.4	22%	0.1	30%
18C	10	110028	13%	122.0	30%	0.2	48%

Table 5.5: Flexural testing results

Pipe ID	No. of Coupons Tested	Avg. Flexural Modulus (MPa)	CV	Avg. Flexural Strength (MPa)	CV	Avg. Flexural Elongation (%)	CV
4A	4	147573	7%	697.6	9%	1.57	8%
4B	4	64825	19%	253.3	14%	0.54	9%
4C	4	74474	12%	241.8	14%	0.41	17%
6A	4	128964	10%	622.5	7%	2.15	17%
12A	8	133601	17%	669.7	15%	2.22	15%

Table 5.6: Correlation coefficients (r) for coupon p-wave velocity (V_P) versus large-strain parameters

	r for Tensile Testing Measurements				r for Flexural Testing Measurements			
Pipe ID	No. of Samples	V_P vs. Modulus	V_P vs. Strength	V_P vs. Elong.	No. of Samples	V_P vs. Modulus	V_P vs. Strength	V_P vs. Elong.
4A	12	0.11	-0.07	0.25	4	-0.64	-0.11	-0.25
4B	8	0.25	0.43	0.14	4	0.47	0.23	-0.47
4C	3	0.31	0.55	1.00	4	0.92	-0.03	-0.81
6A	8	0.23	-0.06	-0.30	4	0.46	0.81	0.66
12A	9	0.64	0.74	0.01	8	0.31	0.30	0.17
18A	8	0.09	-0.37	-0.40	-	-	-	-
18B	5	0.97	0.18	-0.75	-	-	-	-
18C	10	0.20	0.41	0.41	-	-	-	-

Table 5.7: Maximum correlation coefficients (r) for coupon frequency spectrum bandwidth areas versus elastic modulus

Pipe	No. of	r for Bandwidth Area vs. Elastic Modulus				
		FFT Spectra Areas			WT Spectra Areas	
ID	Samples	Freq.[1] (kHz)	No Norm.[2]	Norm.[3]	Freq.[1] (kHz)	Norm.[3]
4A	12	509	0.59	0.46	505	0.71
4B	8	610	0.66	0.67	660	0.82
4C	3	865	0.33	0.93	500	0.92
6A	8	450	0.36	0.52	550	0.48
12A	9	460	0.70	0.68	250	0.49
18A	8	490	0.88	0.85	500	0.86
18B	5	745	0.47	0.66	250	0.73
18C	10	365	0.42	0.54	450	0.57

[1] central frequency of area with maximum correlation

[2] time signals and frequency spectra un-altered

[3] time signals normalized to remove coupling effects

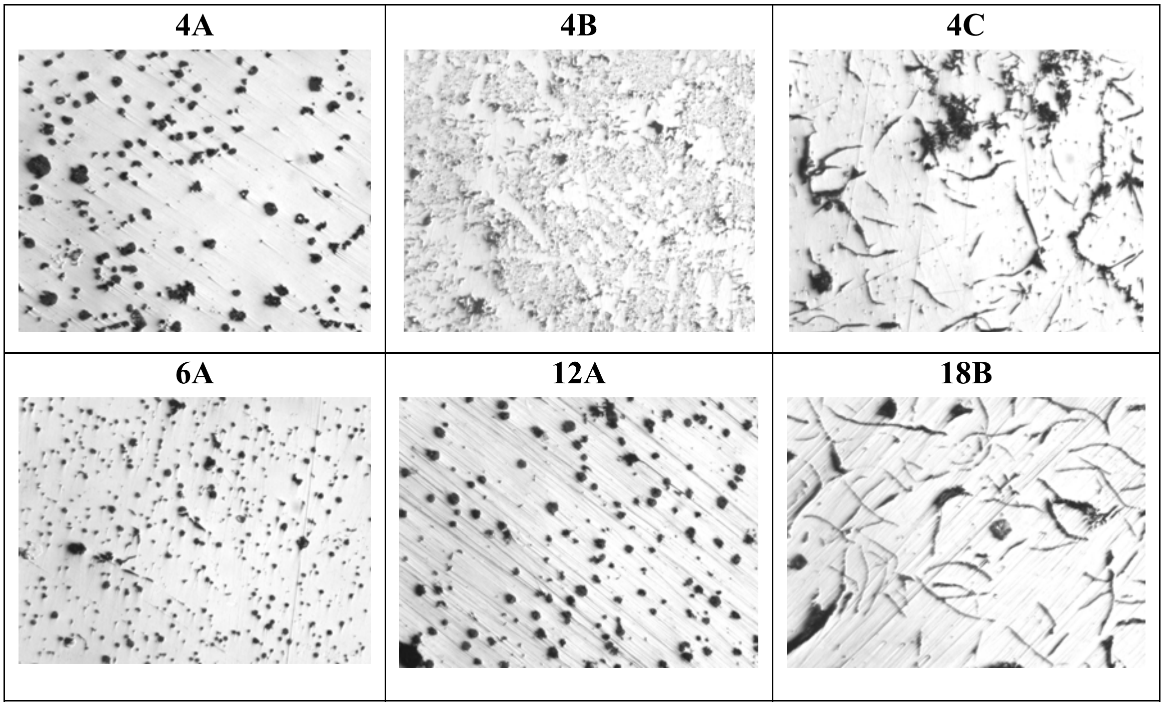

4A

4B

4C

6A

12A

18B

Figure 5.1: Pictures of pipe microstructures (50 × magnification)

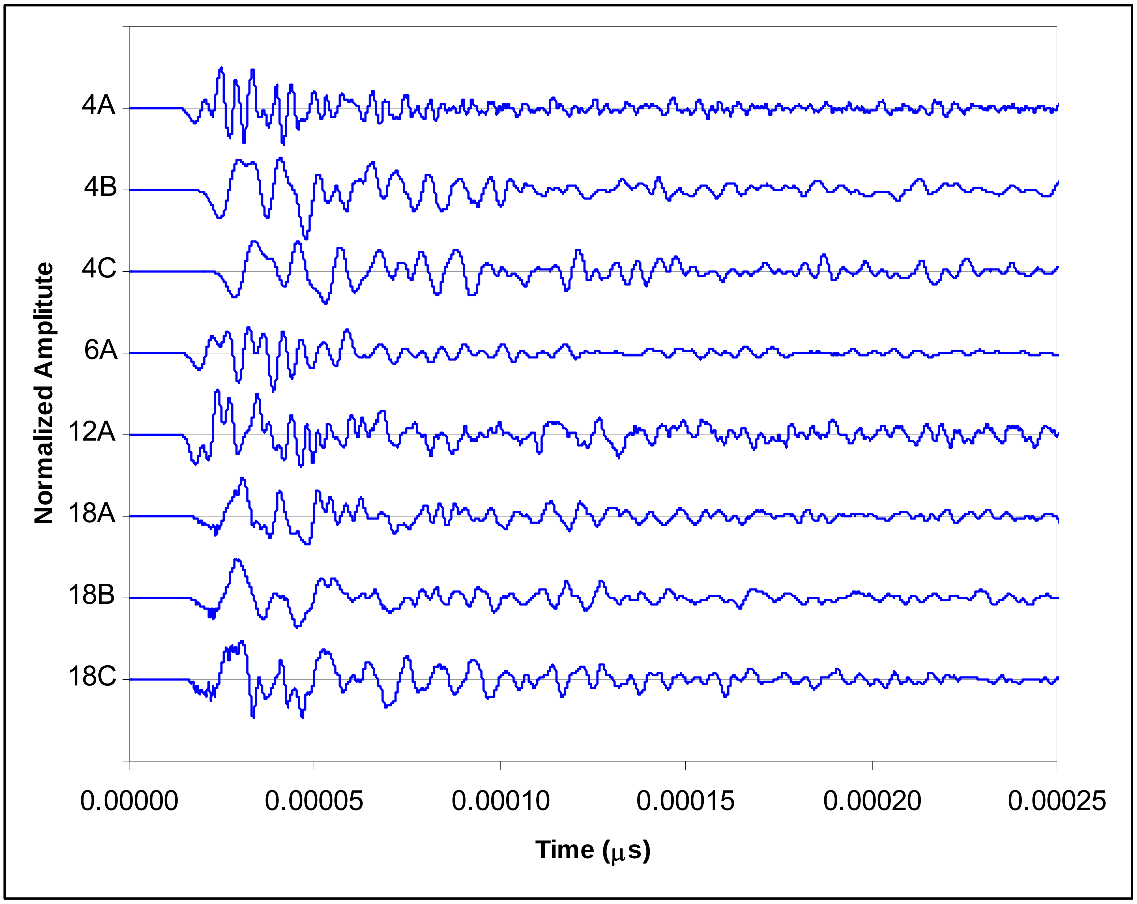

Figure 5.2: Typical time signals

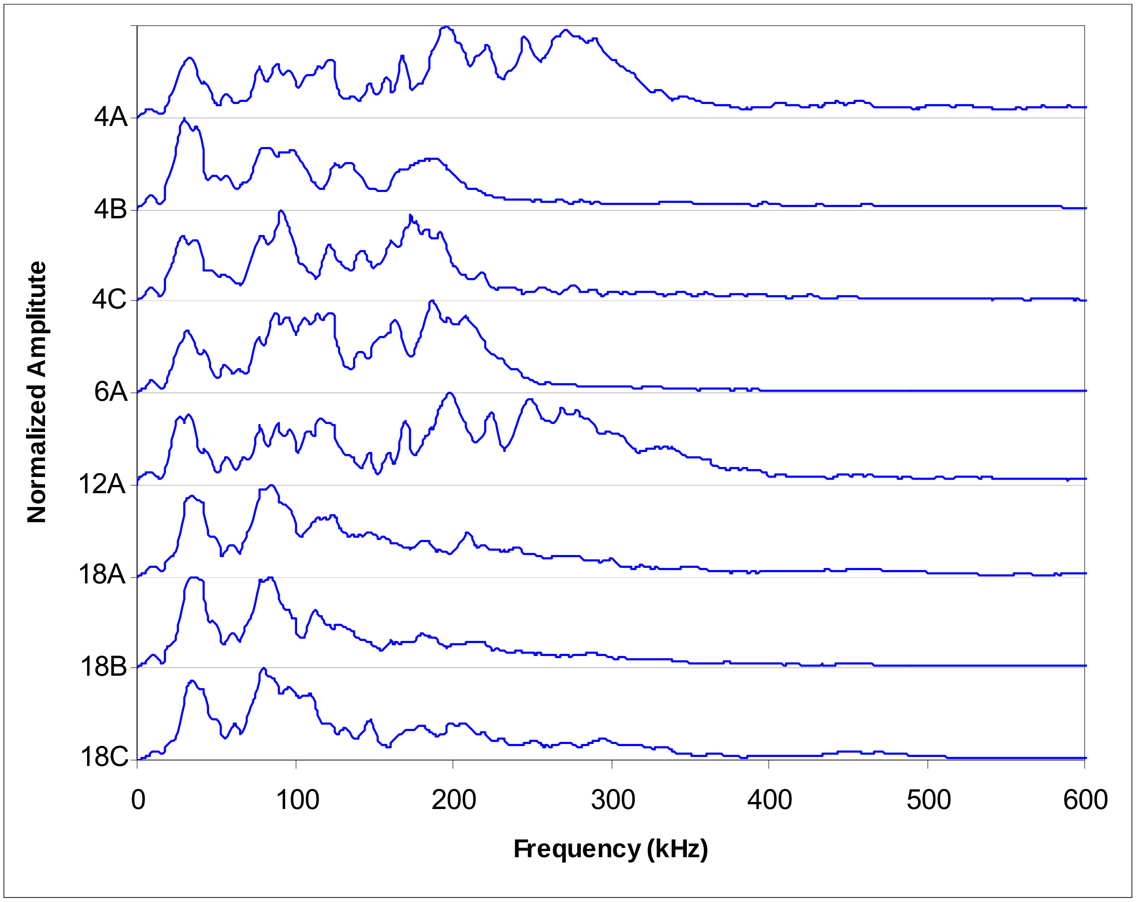

Figure 5.3: Average frequency spectra

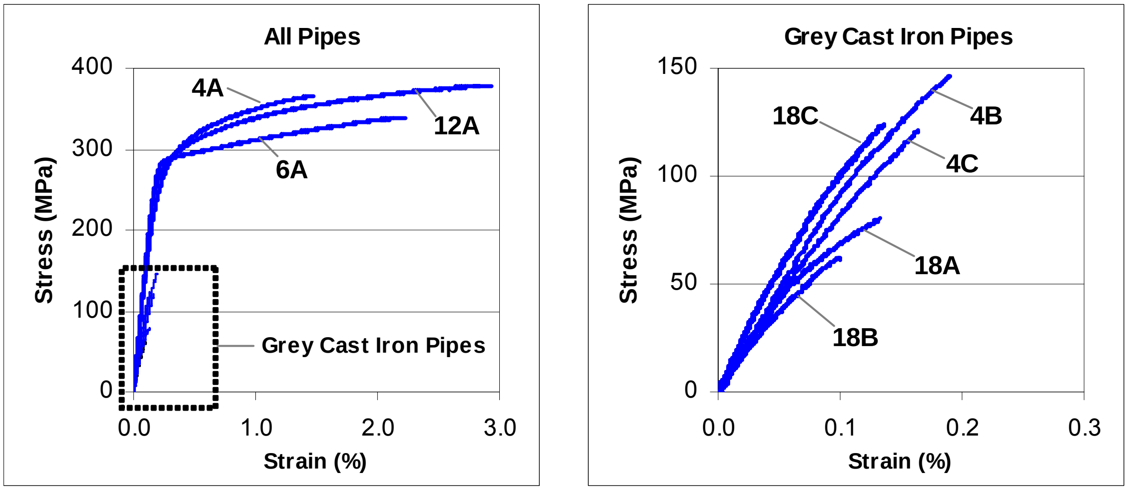

Figure 5.4: Typical tensile stress-strain curves

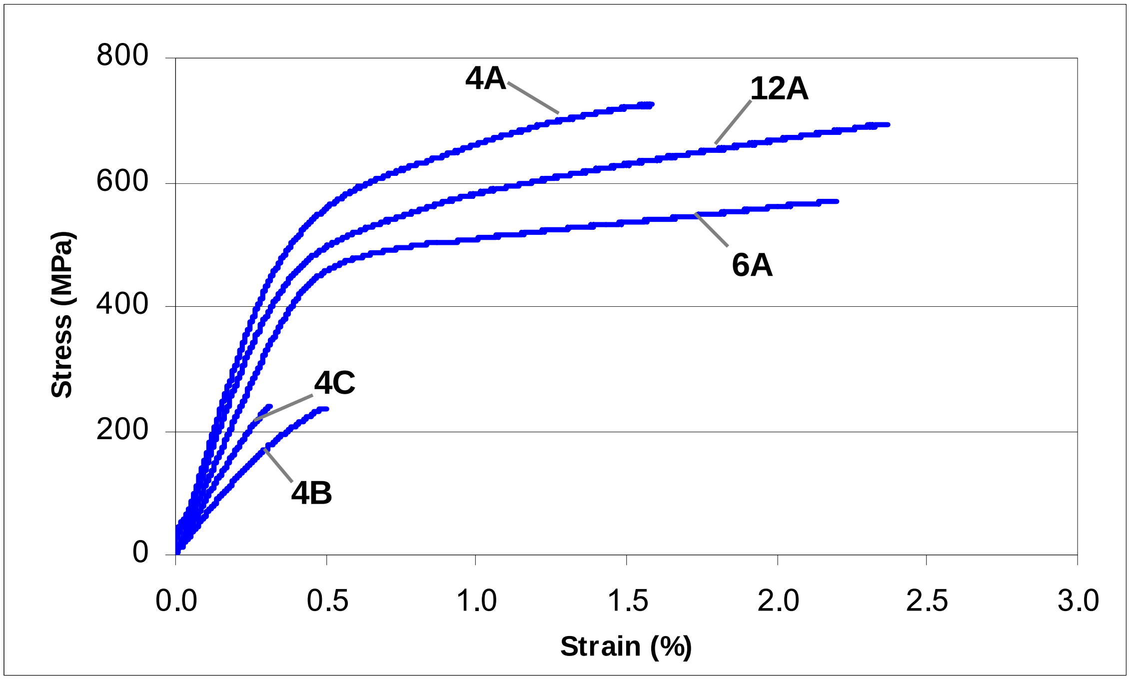

Figure 5.5: Typical flexural stress-strain curves

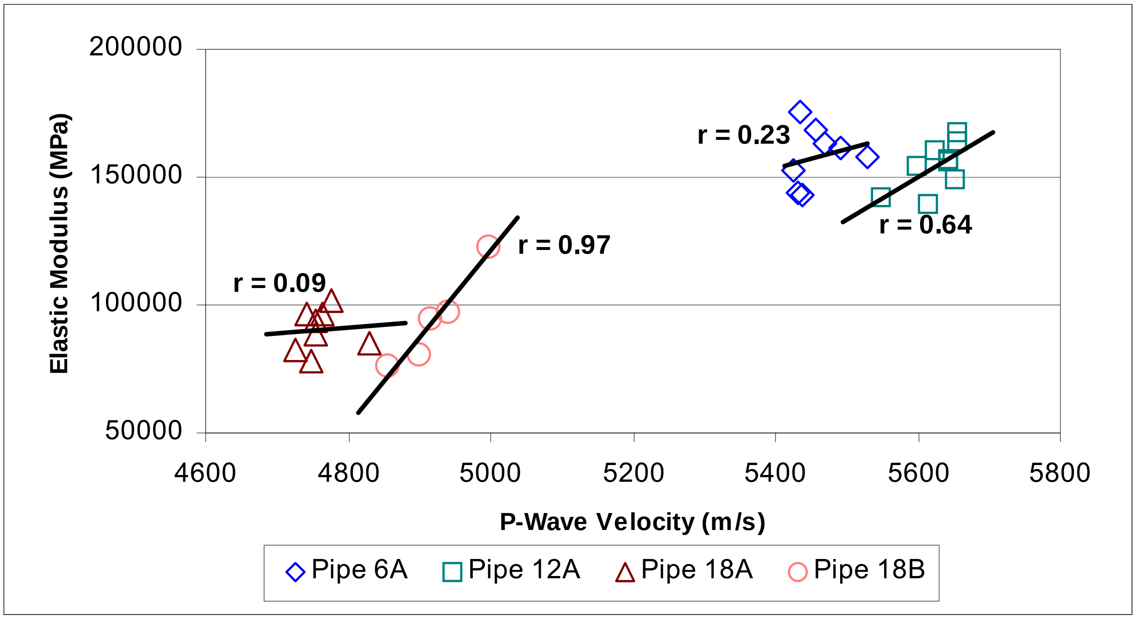

Figure 5.6: Various r values from p-wave velocity and elastic modulus relationships (r related to scatter of points not trend-slope)

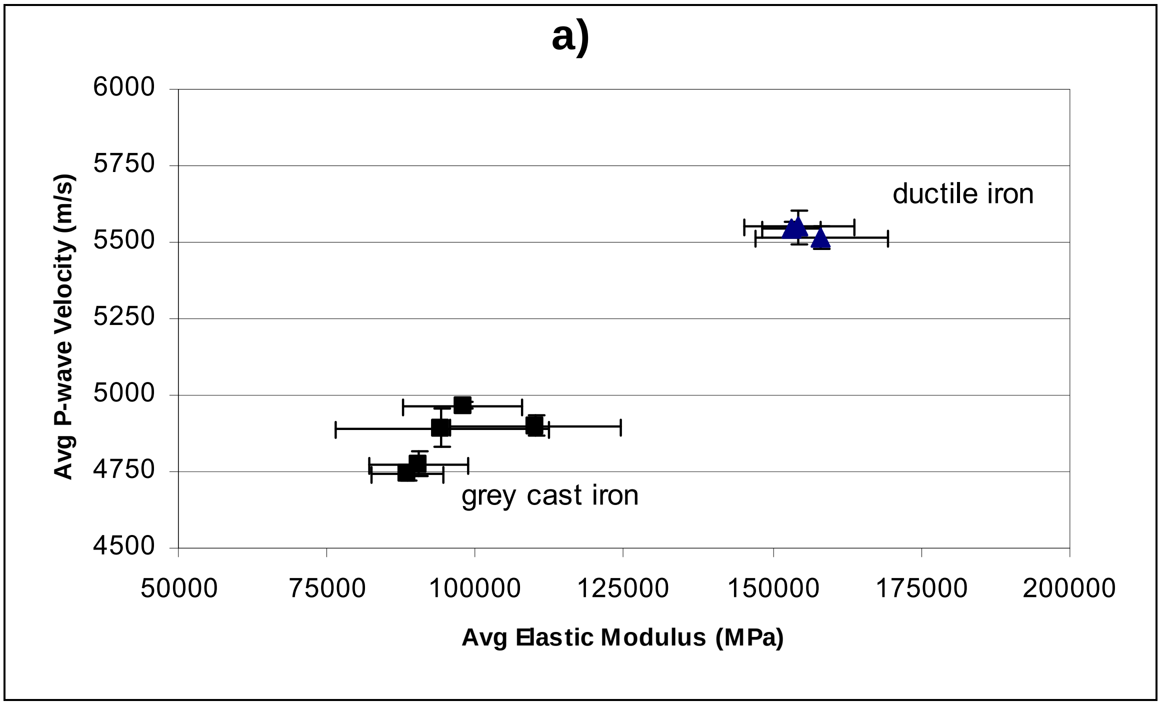

Figure 5.7a: Relationships between average p-wave velocity and elastic modulus(error bars indicate one standard deviation)

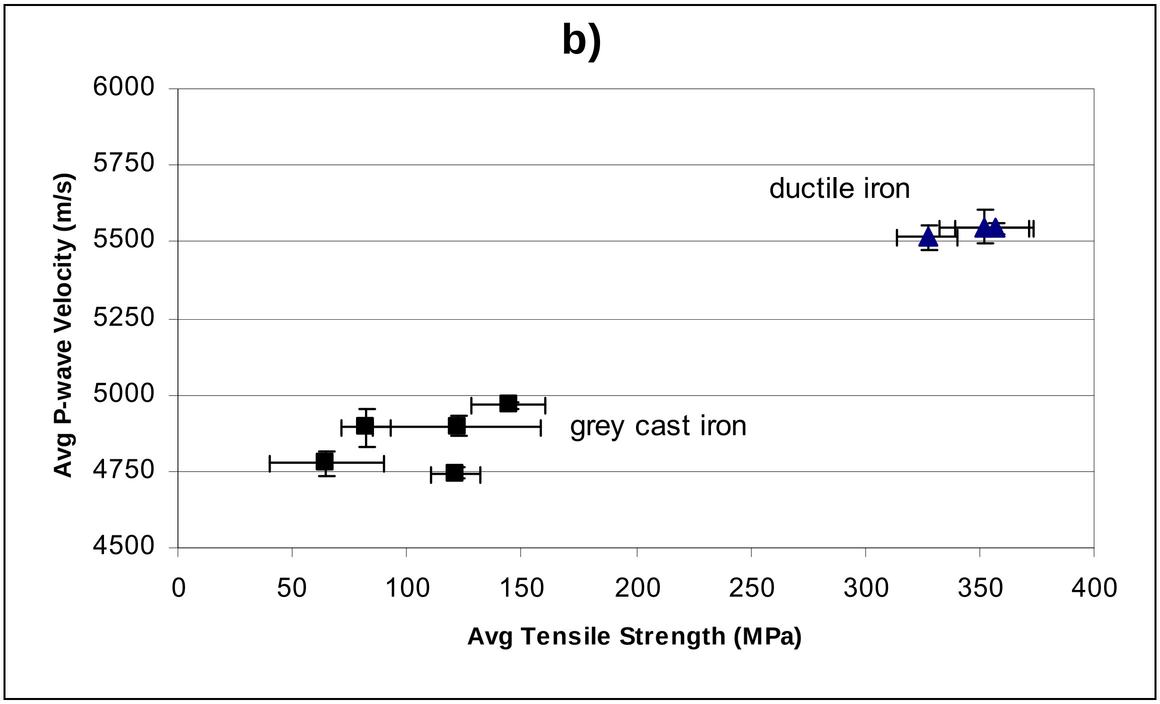

Figure 5.7b: Relationships between average p-wave velocity and tensile strength (error bars indicate one standard deviation)

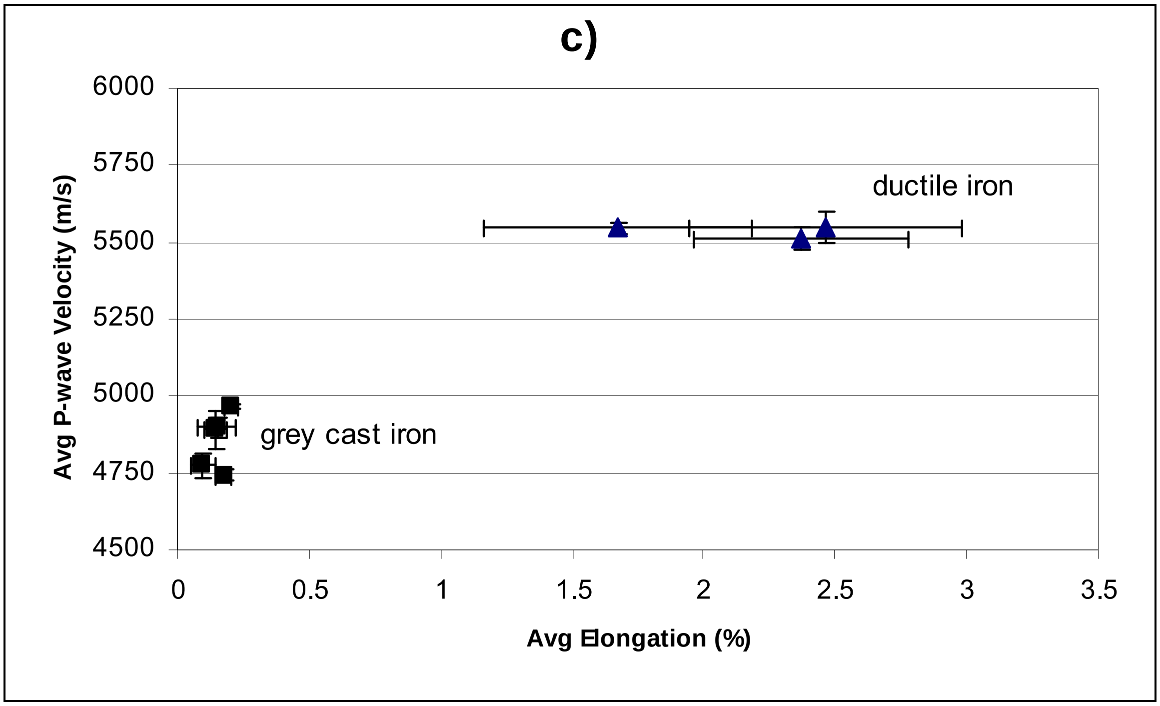

Figure 5.7c: Relationships between average p-wave velocity and elongation (error bars indicate one standard deviation)

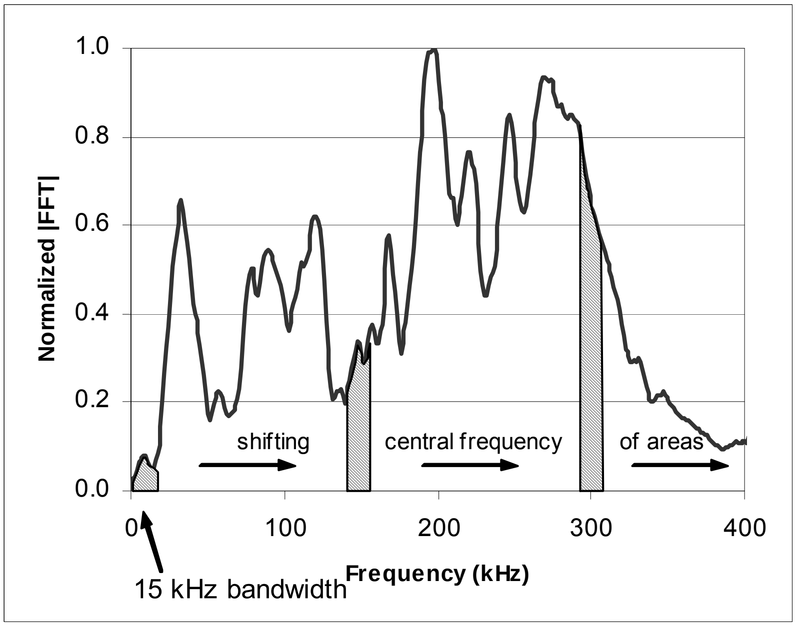

VECTOR OF AREAS	
central frequency (kHz)	norm. bandwidth area
8	0.78
9	0.45
10	0.56
…	…
148	2.89
149	3.27
150	3.63
…	…
298	8.78
299	8.64
300	8.58
…	…
999	0.26
1000	0.28

Figure 5.8: Illustration of shifting bandwidth areas in |FFT| frequency spectra from coupon 4A01

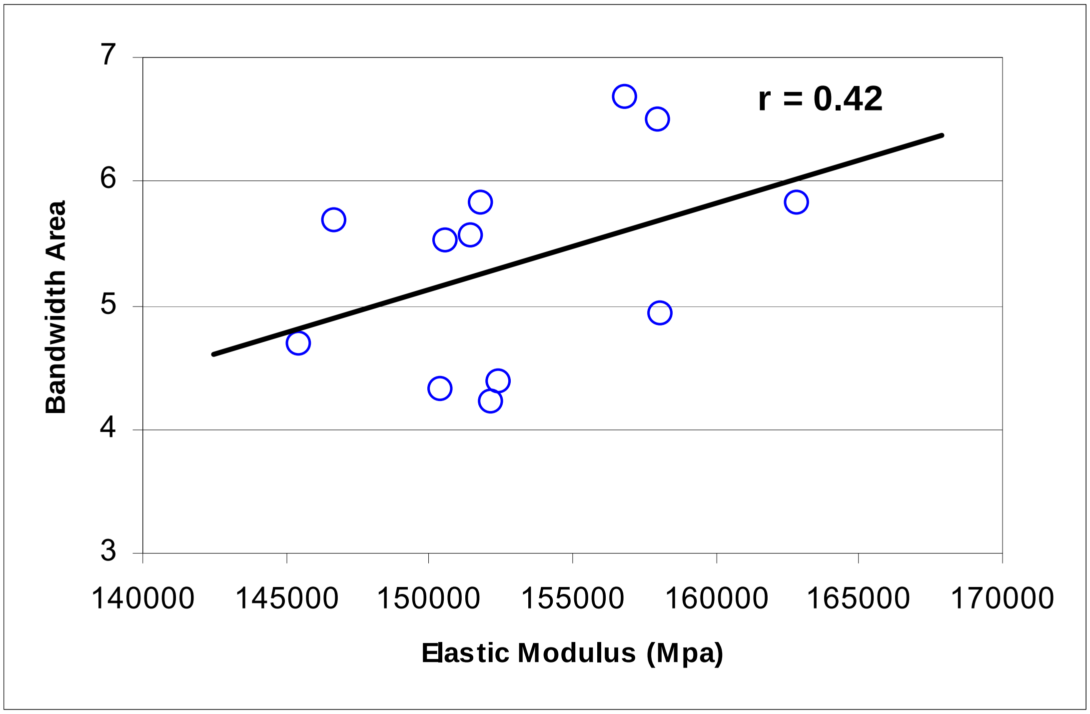

Figure 5.9: Correlation coefficient (r) from 15 kHz bandwidth area centred at 168 kHz

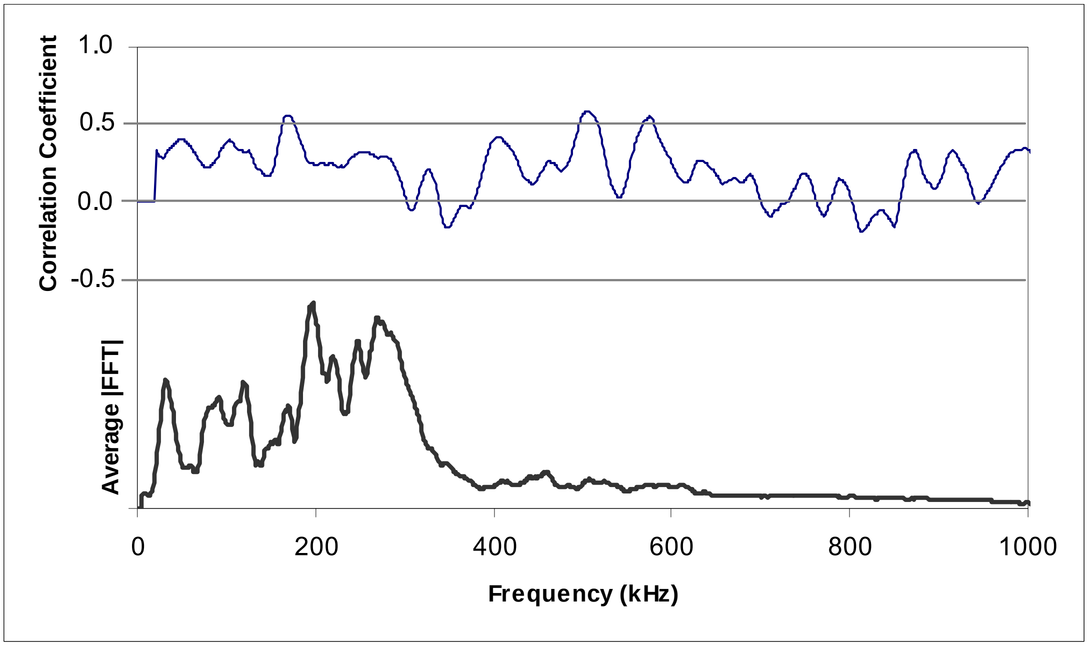

Figure 5.10: Correlation coefficient from 15 kHz bandwidth area plotted with average |FFT| of all coupons in 4A

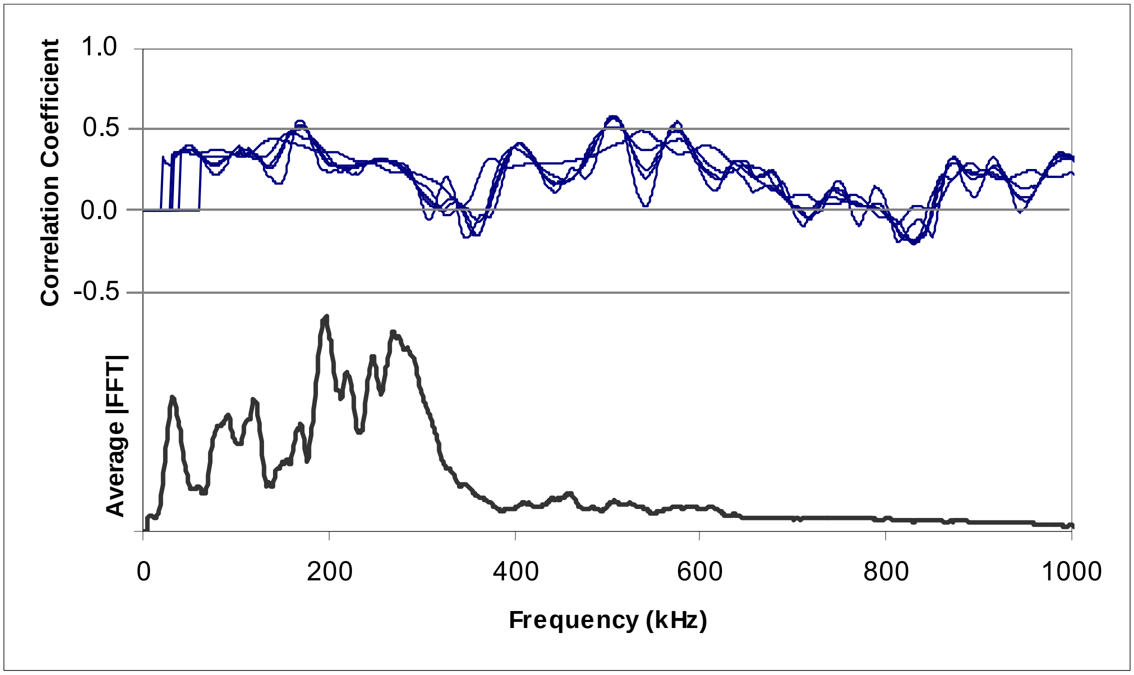

Figure 5.11: Correlation coefficients from all bandwidth (15, 35, 40, 55, and 100 kHz) areas plotted with average |FFT| of all coupons in 4A

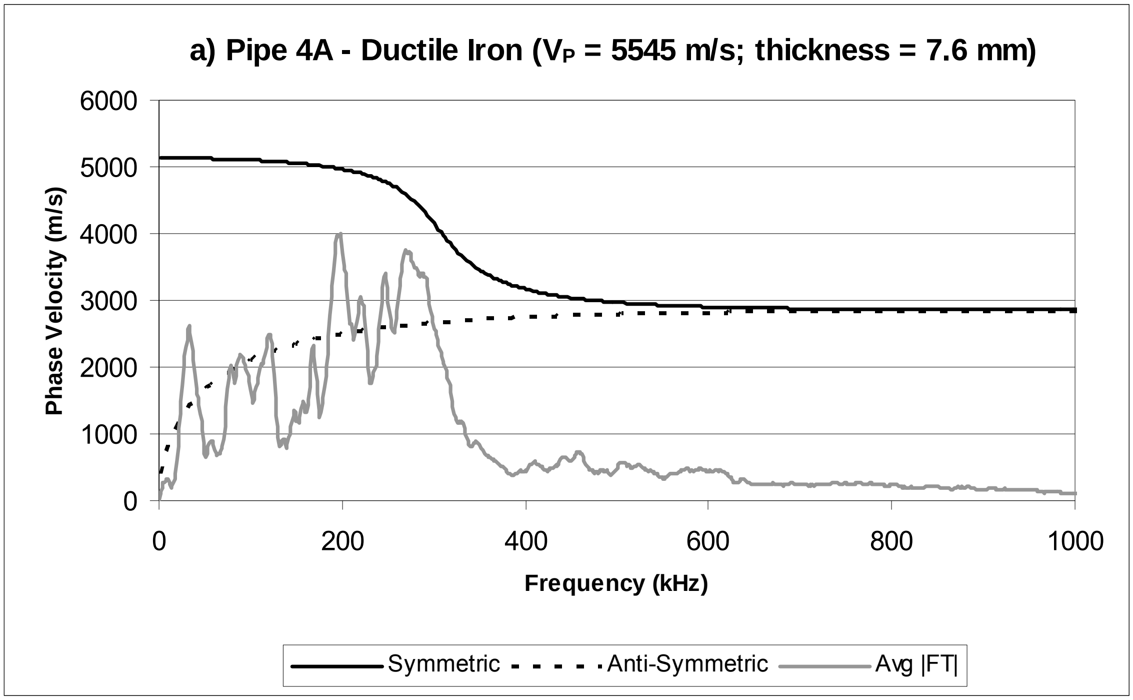

Figure 5.12a: Lamb mode dispersion curves for pipe 4A

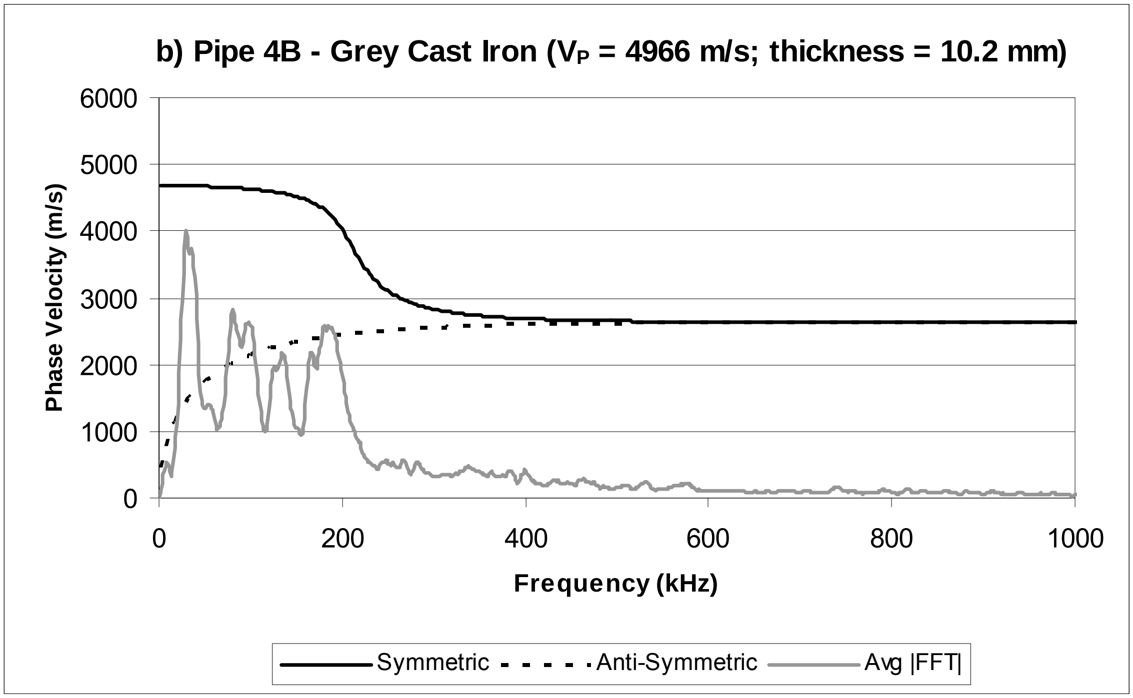

Figure 5.12b: Lamb mode dispersion curves for pipe 4B

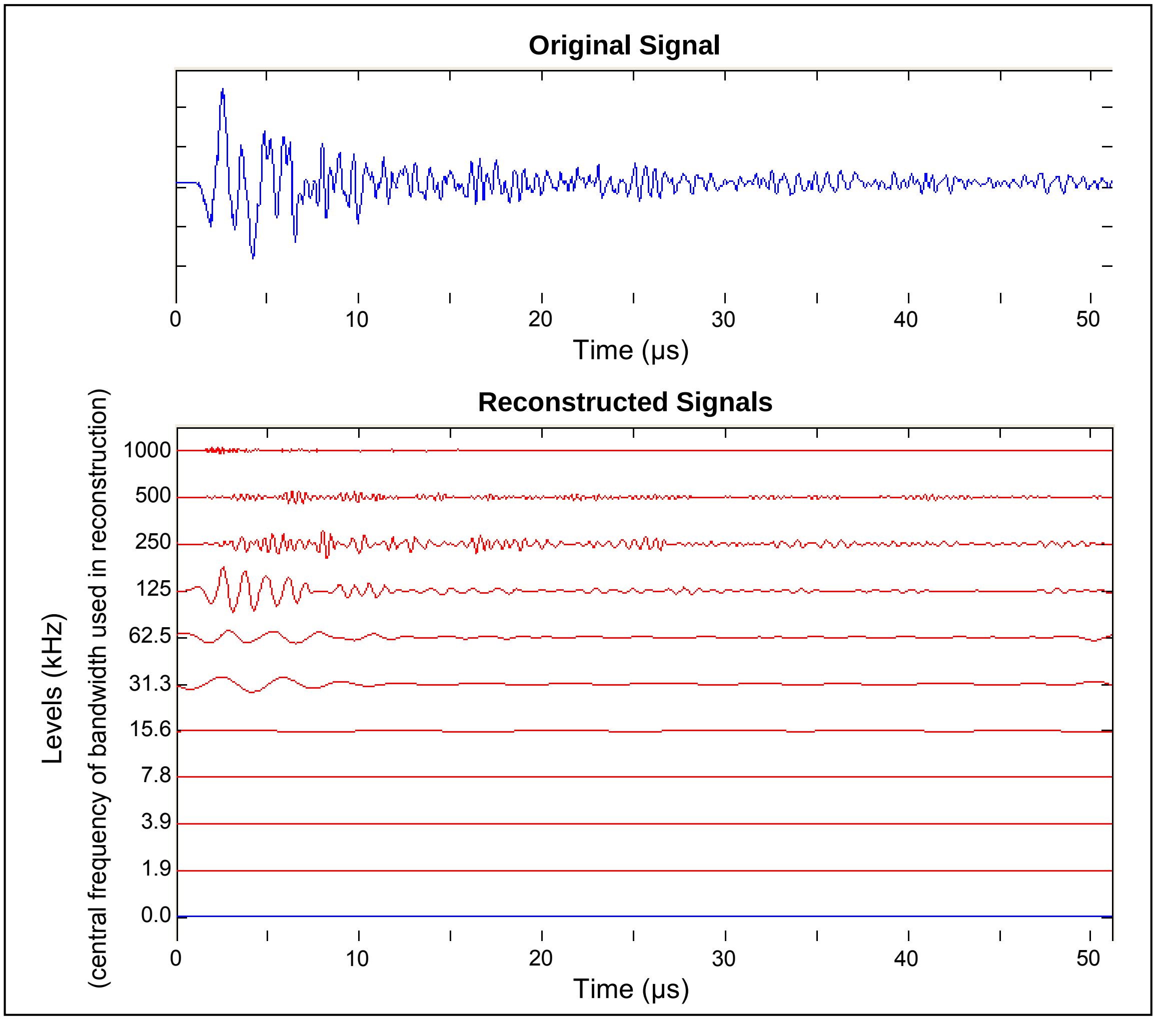

Figure 5.13: Example of Debauchies' wavelet decomposition

CHAPTER 6: USE OF GEOPHYSICAL METHODS FOR SOIL PROFILE EVALUATION

6.1 Background

The design and construction of foundations and embankments require knowledge of the engineering properties and thicknesses of subsurface soils. An important aspect of a foundation investigation is the identification of the depth to a competent layer that can support loads transferred by the foundation. Conventional site characterization involves the drilling of boreholes at selected spacing to generate a model of soil layers. The drilling of a sufficient number of boreholes to adequately establish a subsurface model is often constrained by limited budget, restricted access of drilling equipment, environmental regulations, and challenges in obtaining permission to enter private properties. In consideration of the above constraints, three geophysical techniques were selected for evaluation of their effectiveness in delineating stratigraphy when supported by a limited number of boreholes. These geophysical methods interpret stratigraphy by measuring the change in material properties with depth. They can be conducted from the ground surface and are relatively inexpensive, fast, and environmentally friendly.

The accuracy and resolution of these techniques have been improved significantly in recent years due to advances in equipment and data processing. Consequently, the use of geophysical methods for shallow geotechnical investigations has become increasingly practical. Hirsch et al. (2008) used ERI, SR, and ground penetrating radar (GPR) to delineate gravel and fine grained lacustrine deposits up to 8.5 m thick overlying mudstone bedrock along the Bow River near Calgary, Alberta. The ERI method was the most effective for locating boundaries and detecting changes in sediment type. Their SR method accurately predicted the location of the bedrock interface but was less effective at detecting stratigraphy in the overlying overburden. The GPR method had the greatest resolution within the sediments and showed internal structures not detected by the other methods. However, the signal was severely attenuated in areas with fine-grained sediments of high conductivity. Tomeh et al. (2006) used SR and MASW in a preliminary foundation investigation for a large retaining wall near Atlanta, Georgia. SR was successfully used to delineate the bedrock profile and MASW was used to further characterize subsurface conditions in areas with relatively shallow depth to bedrock (up to 12 m). In addition, Nettles et al. (2008) incorporated ERI and MASW in a detailed geotechnical investigation for a proposed resort property in Rendezvous Bay, Anguilla, BWI. The combination of these methods was successful in determining the thickness of unconsolidated overburden, detecting the depth to competent rock across the site (up to 18 m in depth), and identifying anomalous subsurface features (solution zones and fractures in the limestone). The results showed that these methods are effective in delineating subsurface features, even in complex geological environments.

This chapter presents field results from an investigation performed to evaluate the effectiveness of geophysical methods for the geotechnical site characterization of a site close to an environmentally sensitive wetland area. Previous studies for the area suggested the presence of soft compressible soils underlain by hard glacial till. Three geophysical methods were used across two 188 m lines and their results were verified using borehole and CPT logs. The geophysical methods tested were electrical resistivity imaging (ERI), seismic refraction (SR), and multiple-channel analysis of surface waves (MASW) (Zonge et al. 2005, Redpath 1973, Lai and Wilmanski 2005).

The site studied for this work provided a unique situation for testing the selected geophysical methods. Inverse layering, in which a more compressible layer underlies a less compressible layer, was identified in boreholes across the site: a relatively competent silt and sand layer overlying a softer silty clay layer. Furthermore, the results from ERI, SR, and MASW tests are verified using results from a borehole and CPT investigation.

6.2 Experimental Methodology

This study involved collecting field measurements along two 188 m long lines. Line 1 ran almost from south to north, passing west of a pond and ending near a road (Figure 6.1). Line 2 ran from southwest to northeast along the southeast side of the pond. First, the ERI measurements were collected along the full length of each line. The seismic surveys (SR and then MASW) were subsequently completed along five 47 m long segments - two lines along Line 1 (Lines 1-1 and 1-2) and three lines along Line 2 (Lines 2-1 through 2-

3) (Figure 6.1). The 47 m line span was dictated by the geophone spacing (one metre) necessary for the required depth resolution.

The array patterns for both the SR and MASW methods were configured to accommodate the requirement for a 20 m gap between the furthest seismic source location and the ends of the transducer array. A stream to the northwest of the pond interrupted Line 1. As a result, only two seismic survey test sections were completed along Line 1. The alignment of test section Line 2-3 was altered to avoid the thick forest along the south border of the site.

Five strategically-located boreholes were advanced following the geophysical investigation (Figure 6.1). No drilling was completed along Line 1-2 because it was located because of the close proximity of two residences. BH08-1 was completed prior to the geophysical surveys. One cone penetrometer test (CPT) was completed four of the borehole locations (BH08-3, BH08-4, BH08-6, and BH08-7).

6.3 Experimental Setup and Procedure

6.3.1 ERI

A 48-electrode system was used for the resistivity measurements (Syscal Junior Switch). The electrodes were driven 20 cm into the ground along a straight line array at 4-m spacing. The resistivity meter was positioned at the mid-point of the line. The two lines were surveyed individually using the Wenner electrode array (equal spacing between electrodes). In addition to the two main lines, a higher resolution survey with a closer 2-m electrode spacing was performed from 48 m to 142 m on Line 2. This shorter length survey (94 m long) gave a shallower but more detailed indication of the resistivity structure of the upper stratigraphy over the middle part of Line 2. The system performed a series of electrical resistivity measurements by automatically cycling through different electrode locations and different electrode spacings to create a profile along the measurement line. Smaller electrode spacings are used to measure shallow field resistivities, while subsequently greater spacings are used to increase the depth of the measurements.

6.3.2 SR

The seismic refraction survey was performed using a 48-channel seismograph (Geode seismic recorder) and 48 horizontal geophones (50-Hz). The sensitivities of the geophones were verified by mounting them individually on a shaker (Labworks Inc. Model NV-ET-26B) and comparing the output response of the geophone to that of one accelerometer (Dytran Instruments Inc. Model 3035BG) attached to the geophone casing. Typical sensitivity curves with frequency for the horizontal geophones used in the SR survey and the vertical geophones used in the MASW survey are illustrated in Figures 6.2a and 6.2b, respectively. The SR method is based on first arrivals; thus, the non-linear response of the horizontal geophones (Figure 6.2a) does not have a significant effect on the results. However, the flat response of the vertical geophones (Figure 6.2b) is necessary for accurate measurement of dispersion curves in MASW analysis.

The geophone spacing was one metre for a total spread length of 47 m. Approximately ten cm of top soil was removed at the locations of the geophones and the seismic source to enhance the coupling of the transducers with the ground since coupling increases the signal-to-noise ratio of the measurements.

The seismic source was a 5 kg sledgehammer. S-waves were generated by hitting a c-shaped steel plate in the direction perpendicular to the geophone line. The edges of the c-plate were partially inserted into the ground to enhance the coupling between the plate and the ground. S-waves were used because of their smaller wavelength and therefore better resolution in comparison with p-waves. The horizontal geophones were oriented perpendicular to the survey line to record mostly s-wave motion.

Seismic traces were collected for seven different source locations: -20, -10, -0.5, 23.5, 47.5, 57, and 67 m. The source offsets were selected in the field so that sufficient refractions from the shallow and deep layers were obtained so that the stratigraphy could be interpreted. For each source location, positive and negative polarity shear waves were generated by hitting the steel plate in opposite directions. The change in wave polarity is used to enhance the interpretation of the first arrival times. Any generated p-waves do not change polarity which permits them to be differentiated from the s-waves. The signals from five blows on either side of the plate were recorded and stacked to improve the signal-to-noise ratio.

6.3.3 MASW

The MASW data was collected at the same geophone locations and using similar equipment as the seismic refraction data. The same 48-channel seismograph (Geode seismic recorder) was used with 48 low-frequency (4.5 Hz) vertical geophones. The sensitivities of the vertical geophones were verified as discussed above (Figure 6.2b). The geophone spacing was one metre for a total spread length of 47 m. The top ten cm of soil was removed from the selected source locations and geophone locations to enhance the coupling with the ground.

Different seismic sources were tested in a preliminary site investigation to select the best source for generating lower frequencies. The most effective seismic source was a 80 kg weight raised approximately 1.5 m and dropped onto a steel plate using a tripod-pulley system.

Seismic traces were collected for seven different source locations: -20, -6, -2, 49, 53, and 67 m. The shorter offset distances were used to study the propagation of higher frequencies (shallower layers), while the larger offsets were used to study the propagation of lower frequencies (deeper layers).

6.4 Results and Discussion

The main findings of the geophysical site investigation are presented below. The geotechnical site investigation (standard penetration test (SPT) and CPT testing) was performed after the geophysical tests. However, the results of the geotechnical investigation are presented first in order to simplify the discussion of the geophysical test results.

6.4.1 Boreholes and CPT

The results from the borehole SPT N values, the CPT resistivity and friction ratio, and the general stratigraphy are presented in Figures 6.3a through 6.3d. The borehole investigation revealed three layers across the site overlying a competent sandy silt till: a soft silt and clay surficial layer, a more competent sand and silt layer, and a soft silty clay overlying the till.

6.4.2 ERI

The depths to the competent till layer predicted by the resistivity survey and their comparison with the borehole data are presented in Table 1. Cross-sections generated from the ERI inversion are shown in Figures 6.4a through 6.4c. Inversion of the ERI data was completed using commercial software (Res2dinv, ver. 3.55, Geotomo Software 2006). The resulting cross-sections for Lines 1 and 2 generally show higher conductivity layers (7.6 to 13.2 mS/m) overlying a lower conductivity layer (2 to 4 mS/m). The simplest lithological system that is consistent with these results is upper clay rich layers and a lower layer containing more sands, silts and gravels. The less conductive material was interpreted as the till layer.

Table 6.1 indicates a difference of -2.5 m to +1.3 m between the depths of the till obtained through the ERI analysis and the borehole measurements. The maximum error (-2.5 m) occurred at BH-01 which was drilled prior to the geophysical survey and is located approximately 8 m offset from Line 2 (Figure 6.1). The next highest error (+1.3 m) occurred at BH08-4 which is located approximately 10 m offset from Line 2 (Figure 6.1). The location of this hole is also close to the end of Line 2 (16 m from the end of the line). The inversion algorithm provides results for the depth of the till in Line 2 beginning at approximately 20 m from the ends of the line because of the lack of resolution at the ends of the electrode array. The till boundary is outside the resolvable domain of the ERI inversion at BH08-04. The depth of the till from the right extremity of the ERI cross-section was used in the comparison with the borehole log (right side of Figure 6.4b). Except for the errors introduced by the locations of these two boreholes, the comparison between the borehole and ERI measured depth to till shows very good agreement with the borehole data (less than 0.3 m error on average).

The resolution of the ERI surveys with 4-m electrode spacing was not as effective in defining the upper lithologies. The 4-m spacing survey of Line 1 indicated only one layer overlying the till with conductivities between 12.5 to 13.2 mS/m (Figure 6.4a). The inverted cross-section accurately detected a pre-existing channel of the on-site stream which correlated well with the depth-to-till identified from BH08-5. A decrease in the conductivity of the upper layer below the existing stream is also observed in the original ERI inversion for Line 1. This trend is consistent with the assumption of fresh water from the stream being more resistive than pore water in the soil further below the stream.

The ERI profile from the 4-m spacing survey of Line 2 identified two layers above the till (Figure 6.4b), although the second layer was most prominent within the second half of the line. The upper-most less conductive layer (7.6 to 9.7 mS/m) identified in the inversion is consistent with the sand and silt layer identified in the boreholes. The more conductive layer (10.4 to 13.2 mS/m) overlying the till is consistent with the soft clay layer identified in the boreholes.

The ERI survey with 2-m electrode spacing completed along the middle section of Line 2 clearly identified three layers above the till (Figure 6.4c): an upper layer of higher conductivity (9.0 to 13.2 mS/m) consistent with the surficial silt and clay layer, a second layer of smaller conductivity (7.6 to 9.7 mS/m) consistent with the sand layer, and finally a third layer overlying the till of higher conductivity (10.4 to 13.2 mS/m) consistent with the clay layer identified in the boreholes. The 2-m spacing ERI survey had less resolution at depth and underestimated the depth of the till by approximately 2.0 m.

Laboratory resistivity measurements were completed on various soil samples collected during the borehole investigation to compare against the ERI field survey results. The conductivity of soil is affected mostly by pore water conductivity and mineralogy. The sampling process has little effect on these properties. So, providing that the samples are stored to prevent desiccation, the conductivity of disturbed samples is representative of conductivity of the soil in-situ. The apparatus and procedure used by Piggott (1999) was followed. Electric current was induced through the samples using two stainless steel mesh electrodes covering the opposing faces of the cylindrical specimens. Two additional stainless steel probes were advanced to the centre of the samples to measure the potential drop across the specimen parallel to the current flow. The measured voltage, the sampling interval, and the cross sectional areas of the specimens were used to calculate the conductivity of the soil samples.

The lab measured conductivity of samples taken from the silty clay stratum (third layer from the surface) ranged from 2.6 to 31.6 mS/m with an average of 15.3 mS/m. This value is consistent with the conductivity of the same layer obtained from the ERI field survey (10.4 to 13.2 mS/m). The lab measured conductivity of one sample taken from the till was 1.4 mS/m which also compared well with the ERI field measurements for the same material (2.0 to 4.0 mS/m). Samples from the upper two layers were not measured in the lab because the specimens from these strata were either too dry or too heterogeneous to get reliable resistivity measurements.

6.4.3 SR

Typical time histories and Fourier magnitude spectra for the first 15 geophones from the source, and frequency-wave number (FK) plots (where wave number (K) = $2\pi/\lambda$) for all geophones in the array from the SR surveys for both lines are illustrated in Figure 6.5. The cross-sections generated from the refraction analysis are presented in Figures 6.6a through 6.6e. A reciprocal method analysis for the five survey lines showed only two refracting boundaries across the site: a slower refracting boundary with shear wave velocity ranging from 300 m/s to 500 m/s overlying a faster refracting boundary with a shear wave velocity between 723 m/s and 928 m/s. These values are in the range of expected velocities for the materials identified from the boreholes (NBC 2005). The frequencies observed in the FK plots (Figure 6.5) generally indicate wavelengths greater than four meters. The higher frequency (smaller wavelength) waves were only observed in the first four to five geophones before the arrival of the refracted waves. Because the higher frequency components have relatively less energy than the lower frequency refracted waves, the smaller wavelength energy is not evident in the FK plots.

The upper refractor was taken as the contact between the surficial silt and clay layer and the underlying more competent (higher velocity) sand and silt layer. The lower refractor was considered as the upper boundary of the till. A refracting boundary between the second and third layer from the surface was not detected because of the inverse layering condition identified from the borehole investigation. The second layer from the surface (relatively competent sand and silt) is underlain by a softer silty clay layer resulting in a velocity inversion from which energy is not refracted.

Tomographic inversions (ray tracing method, Menke 1999) were then completed for each line using a commercial software package (Seisimager/2D, ver. 3.1, Geometrics 2005) by inputting the velocities and approximate depths obtained from the reciprocal analyses. The cross-sections generated from the tomographic inversions showed contoured variations of shear wave velocity with depth. These models, in addition to the reciprocal analyses, overestimated the depth of the till by up to four metres because of the velocity inversion mentioned above. Consequently, the depth of the upper boundary of the till in all of the cross-sections was scaled to correlate with the depths observed in the boreholes. This correction was performed so that the SR profiles could be compared with the borehole data. These adjusted tomographic models are presented in Figures 6.6a through 6.6e.

The necessity of the correction of the SR results in this inverse layering case identifies ERI as the better of the first two geophysical methods for locating the depth to till. The trends in the slope of the layers shown in the SR cross-sections do however correlate to the ERI cross-sections and the borehole data. The thickness of the top two layers predicted by the SR results did not correlate well with borehole data because the refraction resolution was not adequate to detect these thin layers (0.5 to 1.5 m). The spacing of the geophones could be reduced to adequately resolve these layers. However, the resulting reduction in the array length will effectively decrease the depth of penetration of the survey.

6.4.4 MASW

The comparison of the surface wave results with the borehole data is presented in Table 2. Typical time histories and Fourier magnitude spectra for the first 15 geophones from the source, and FK plots for all geophones in the array from the MASW surveys for both lines are illustrated in Figure 6.7.Typical dispersion curves for Lines 1 and 2 are shown in

Figures 6.8a and 6.8b and the velocity profiles generated from the MASW analysis are shown in Figures 6.9a through 6.9e. MASW inversion was completed for each line using a commercial software package (SWAN, GeoStudy Astier, 2008). The inversions from the dispersion curves provided layered models with average layer thicknesses and velocity values across each of the five survey lines. In general, the MASW cross-sections show all four distinct layers identified in the borehole investigation: a surficial layer with shear wave velocity ranging from 62 to 119 m/s, a second layer with shear wave velocity ranging from 320 to 423 m/s, a third layer with shear wave velocity ranging from 188 to 334 m/s, and finally a fourth layer with shear wave velocity ranging from 569 to 1266 m/s. These velocity values correlate well to the range of expected velocities for the materials identified by the boreholes (NBC 2005). The MASW survey was the only geophysical method of the three used that clearly identified the inverse layering at all the survey lines. The main frequencies observed in the FK plots (Figure 6.7) indicate that the wavelength of the recorded surface waves ranged from 7 to 30 m. Considering a depth of $\lambda/3$, the recorded R-waves penetrated from about 2 to 10 m.

The presence of a velocity inversion makes the analysis of surface wave tests more complex and requires the consideration of higher modes. The dispersion curve in Figure 6.8a shows that higher modes are more significant for Line 1 because they are closer to the fundamental mode (fitted model). Figure 6.8b shows that only the fundamental mode is important. Consequently, the MASW results for Line 2 are more reliable than the results for Line 1. The participation of higher modes could be responsible for the higher velocities for the till layer obtained from the inversion in Line 1.

Table 6.2 indicates that the MASW method consistently underestimated the depth to the till by up to 3.3 m. The MASW method gives average layer thicknesses along the length of the array, whereas borehole data gives single-point thicknesses. Therefore, differences are expected. Furthermore, one of the limitations of the MASW method is the decreased resolution in the definition of deeper layers if the generation of low frequencies is limited ($f < 15$ Hz for this site). The drop-weight source used in this study did generate low frequencies. However, they were not strong enough to improve the resolution in the location of deeper layers because of the presence of the velocity reversal. The inverse layering acts as a high-pass filter which reduces the penetration of large wavelengths into the ground. The drop-weight source should be modified to enhance the generation of low frequencies which should increase the resolution of deeper layers using the MASW method.

The MASW results predict the thicknesses of the upper three layers with varying degrees of accuracy as seen in Table 6.2. Again, some of this error may arise from comparing average values to discrete location measurements. The error increased with each successively deeper layer, further illustrating a decrease in resolution with depth.

Table 6.1. Depth of till predicted by ERI

	Depth to Hard Till (m)		
BH No.	From BH	From ERI	Difference
08-1	9.0	6.5	-2.5
08-3	6.1	6.3	0.2
08-4	10.7	12	1.3
08-5	6.1	5.7	-0.4
08-6	4.6	4.8	0.2
08-7	10.1	9.9	-0.2

Table 6.2. Layer thicknesses predicted by MASW

BH No. (MASW Line)	Layer[1]	Layer Thickness (m) From BH	From MASW	Difference
08-1 (Line 2-1)	1	1.2	0.7	-0.5
	2	1.7	1.5	-0.2
	3	6.1	5.2	-0.9
	Till Depth	9.0	7.4	-1.6
08-3 (Line 2-3)	1	0.6	0.9	0.3
	2	1.7	2.0	0.3
	3	3.8	3.1	-0.7
	Till Depth	6.1	6.0	-0.1
08-4 (Line 2-2)	1	0.6	0.6	0.0
	2	1.5	1.4	-0.1
	3	8.6	5.4	-3.2
	Till Depth	10.7	7.4	-3.3
08-5 (Line 1-1)	1	1.3	1.4	0.1
	2	1.0	1.1	0.1
	3	3.8	1.6	-2.2
	Till Depth	n/a[2]	4.2	n/a[2]
08-6 (Line 1-1)	1	1.4	1.4	0.0
	2	1.3	1.1	-0.2
	3	1.9	1.6	-0.3
	Till Depth	4.6	4.2	-0.4
08-7 (Line 2-2)	1	0.5	0.6	0.1
	2	3.2	1.4	-1.8
	3	6.4	5.4	-1.0
	Till Depth	10.1	7.4	-2.7

(1) layer 1: silt and clay; layer 2: sand and silt; layer 3: silty clay

(2) no comparison because till depth from BH08-5 is in buried creek bed

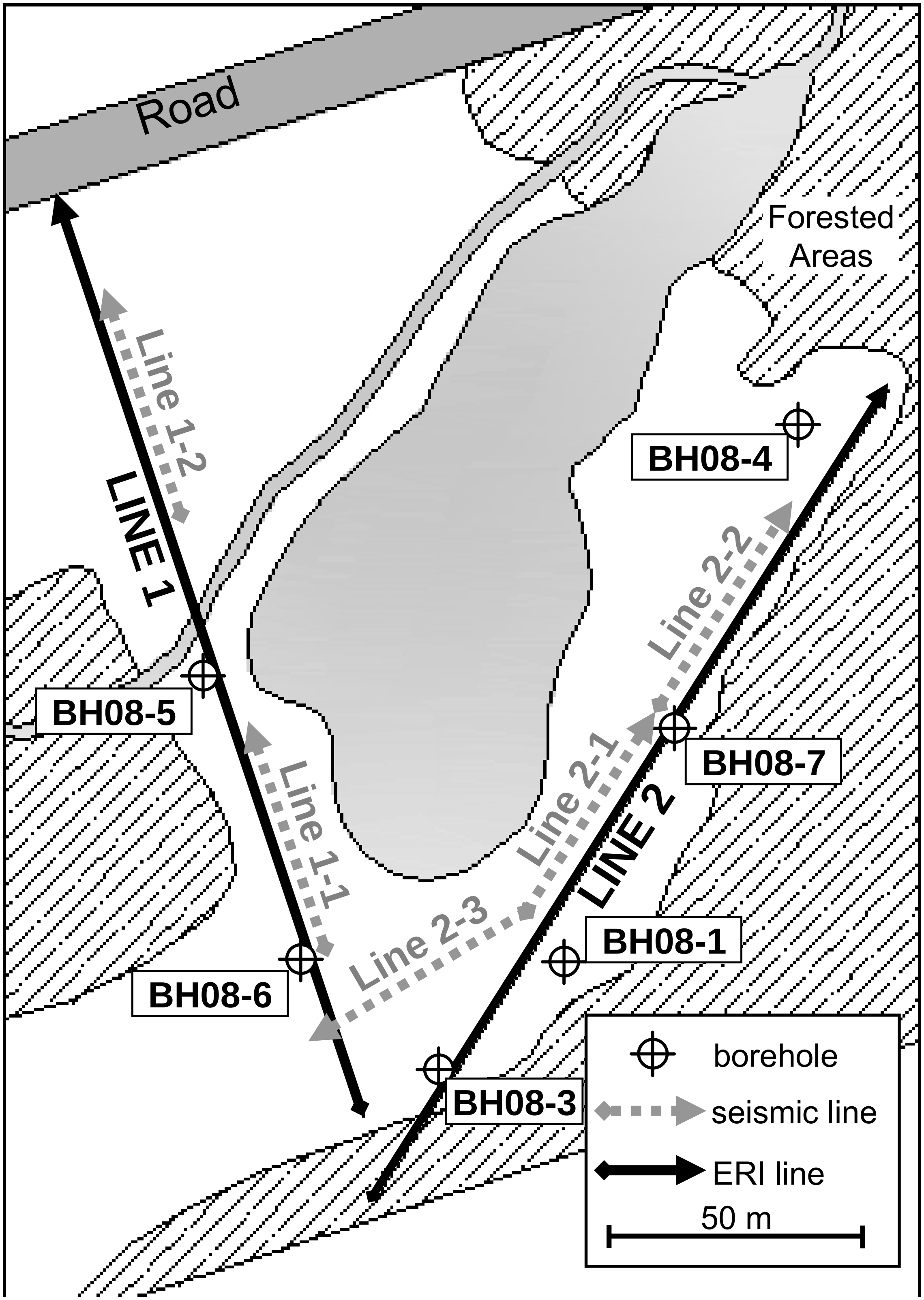

Figure 6.1: Survey line and borehole locations

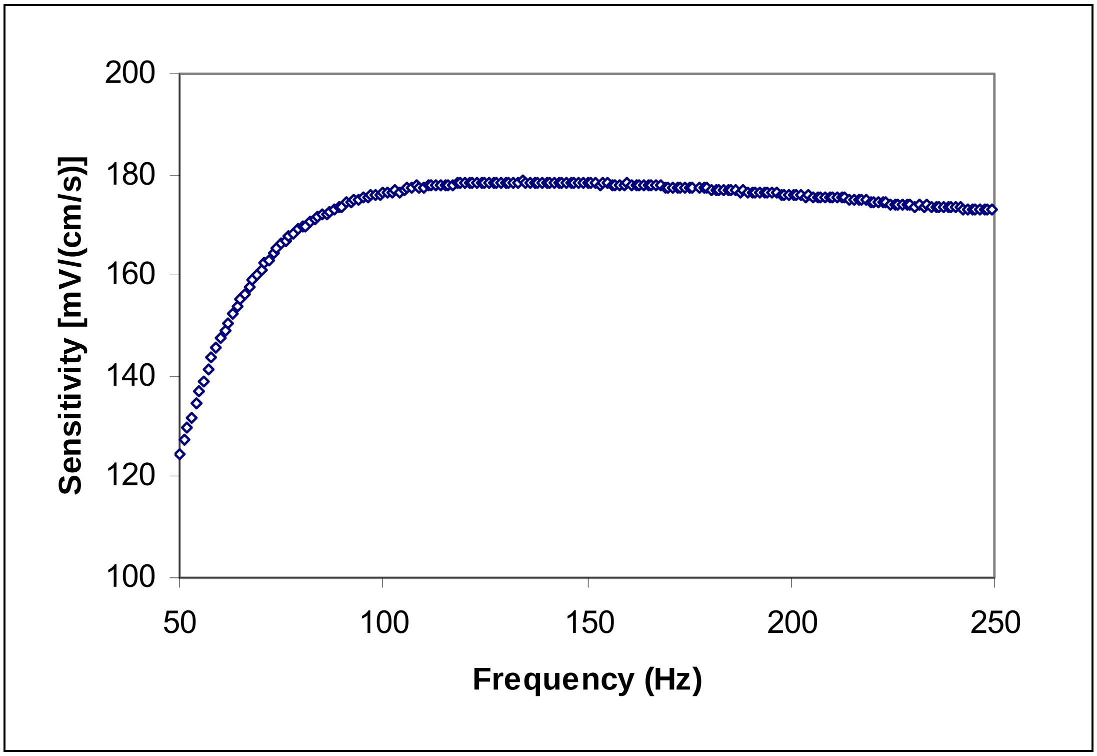

Figure 6.2a: Typical sensitivity curve for horizontal geophones

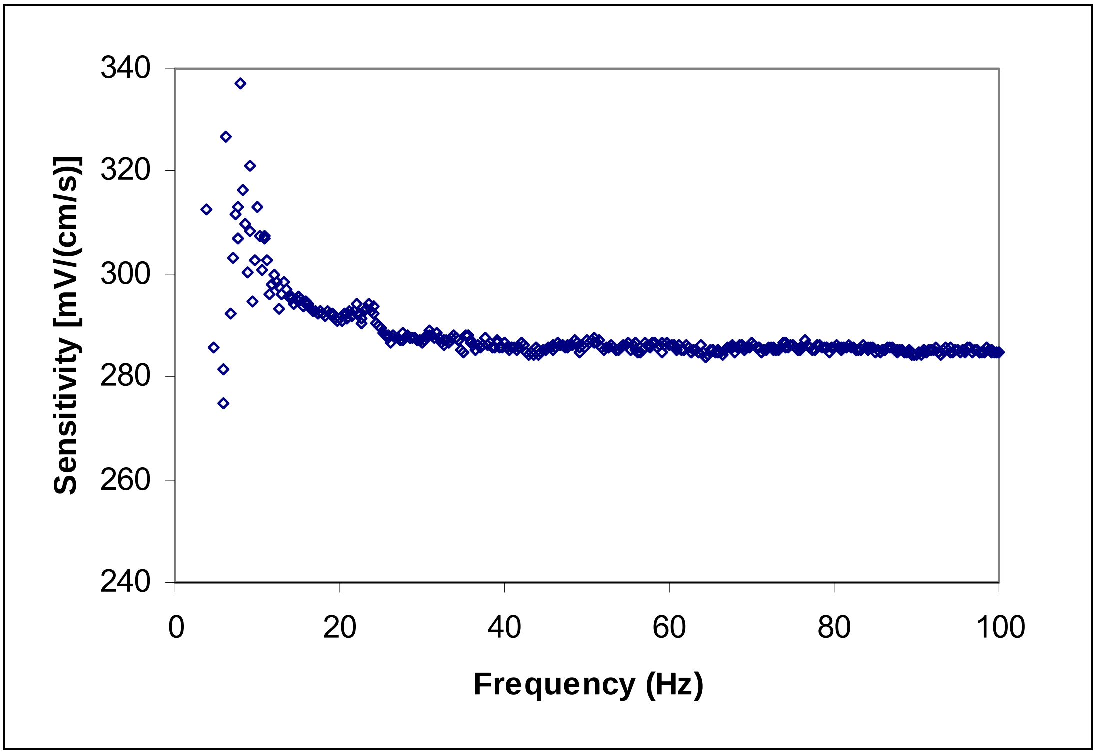

Figure 6.2b: Typical sensitivity curve for vertical geophones

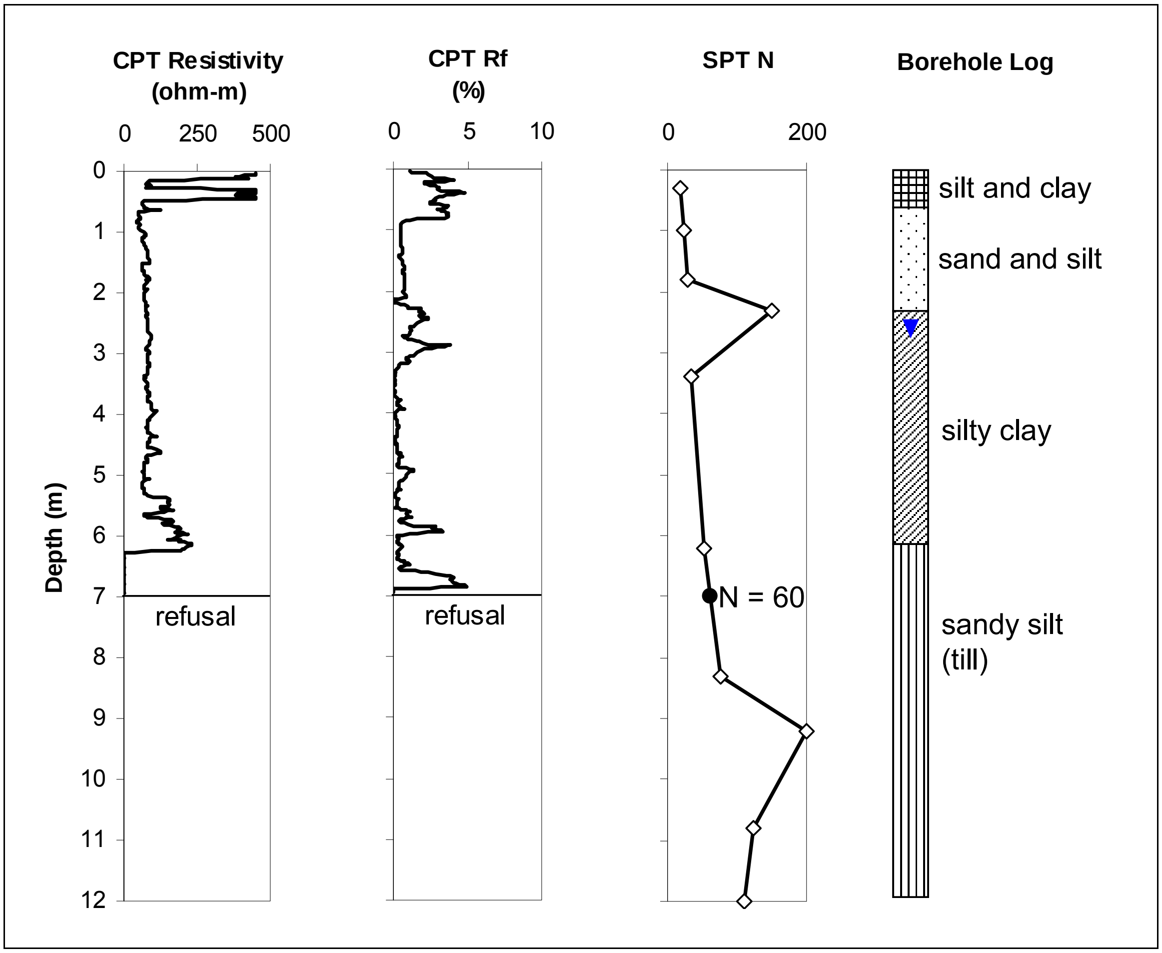

Figure 6.3a: CPT and SPT results for BH08-3

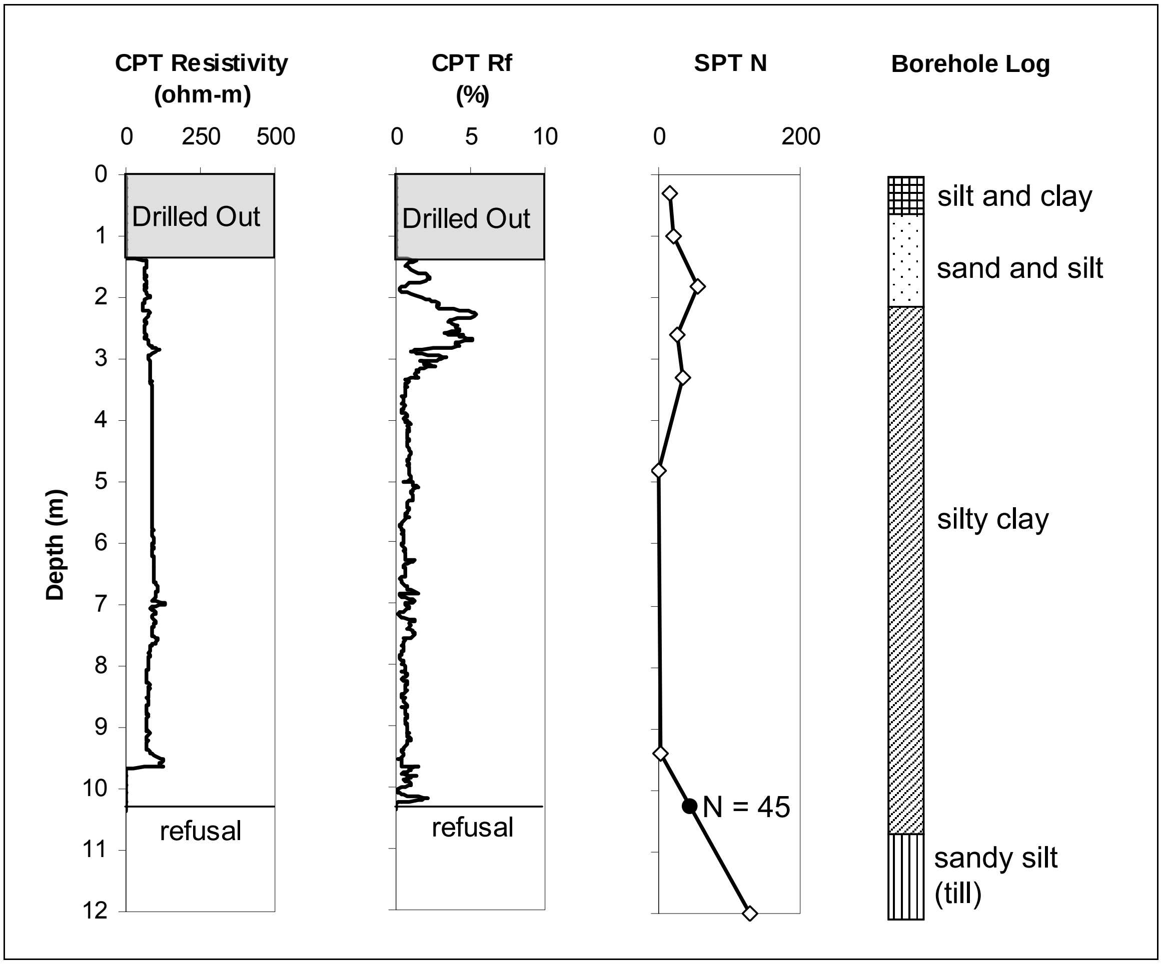

Figure 6.3b: CPT and SPT results for BH08-4

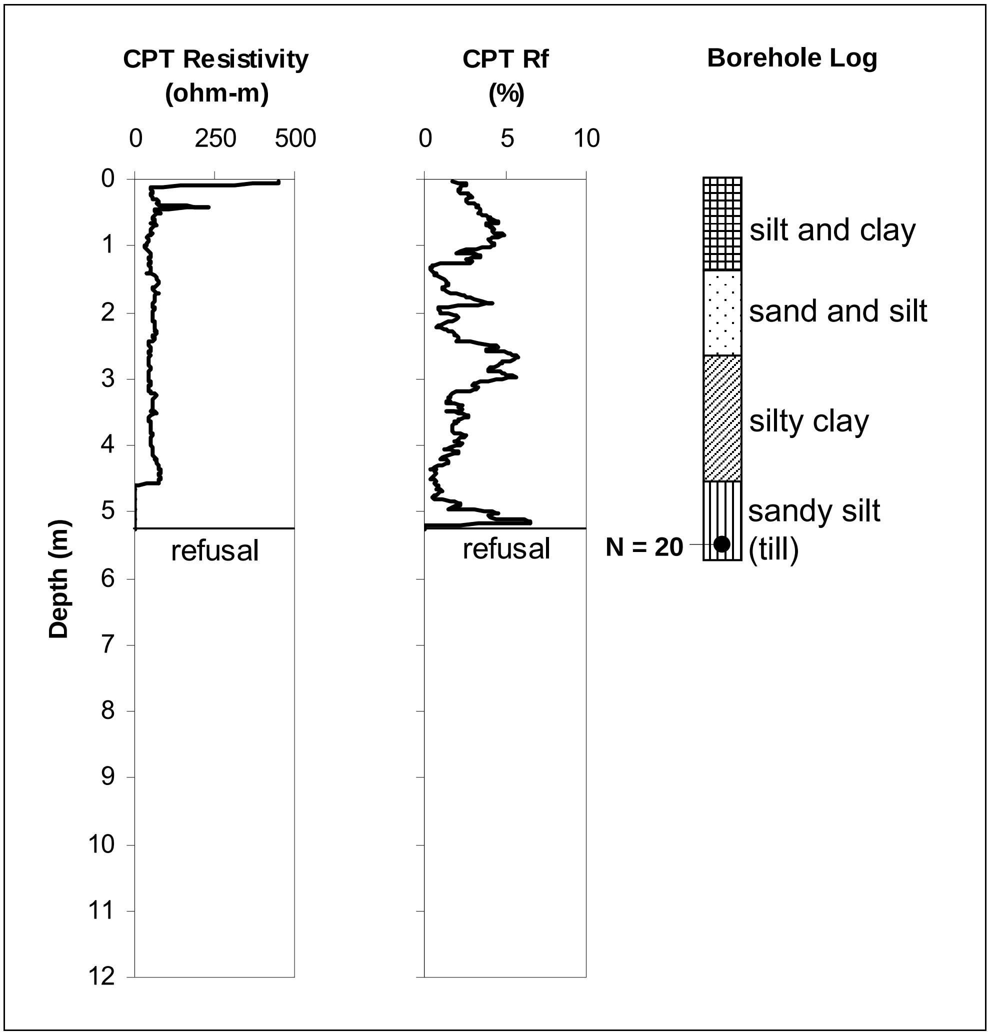

Figure 6.3c: CPT and SPT results for BH08-6

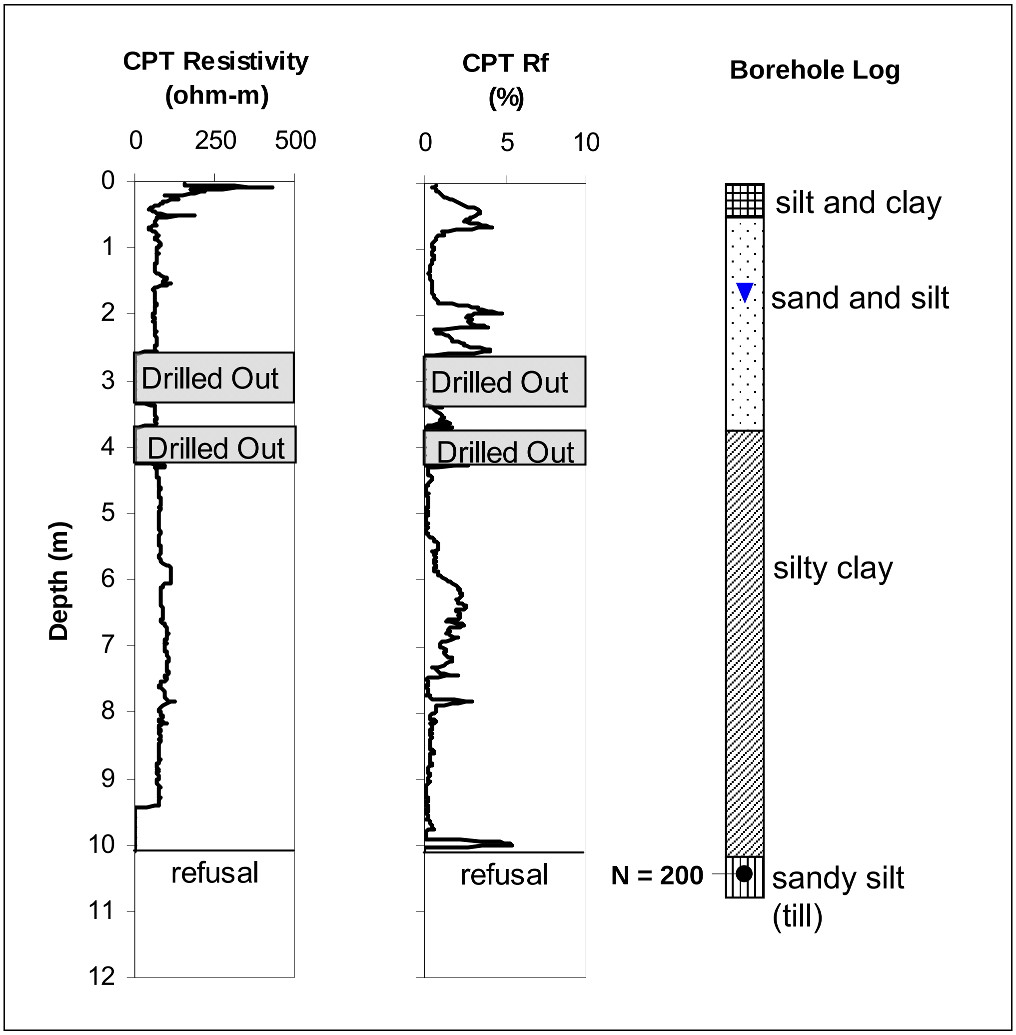

Figure 6.3d: CPT and SPT results for BH08-7

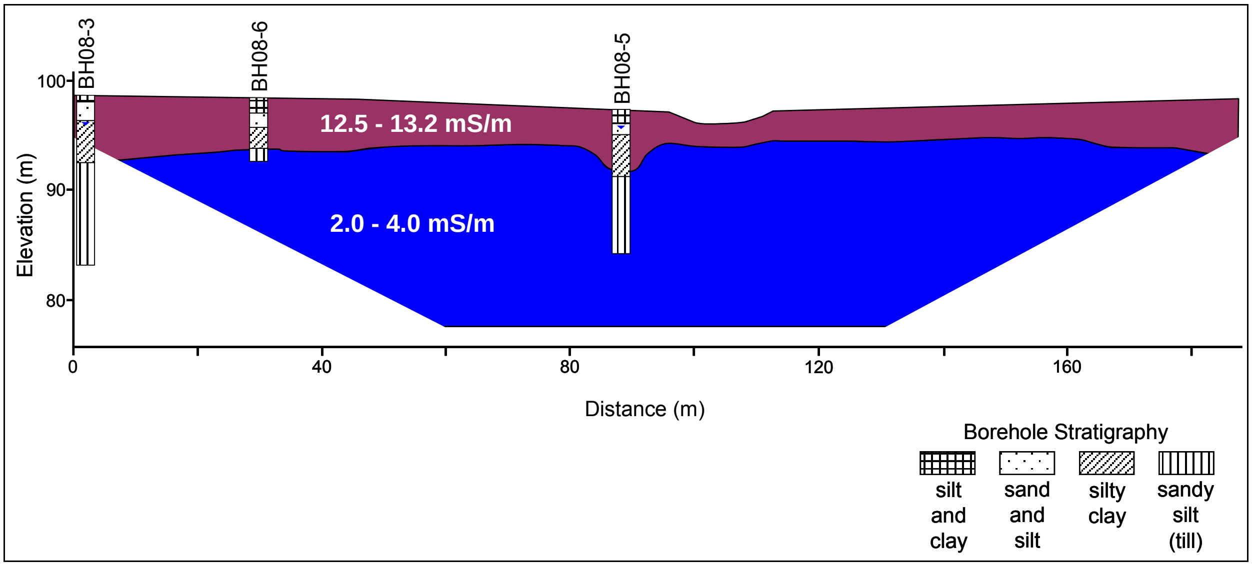

Figure 6.4a: Line 1 ERI cross-section (4-m electrode spacing)

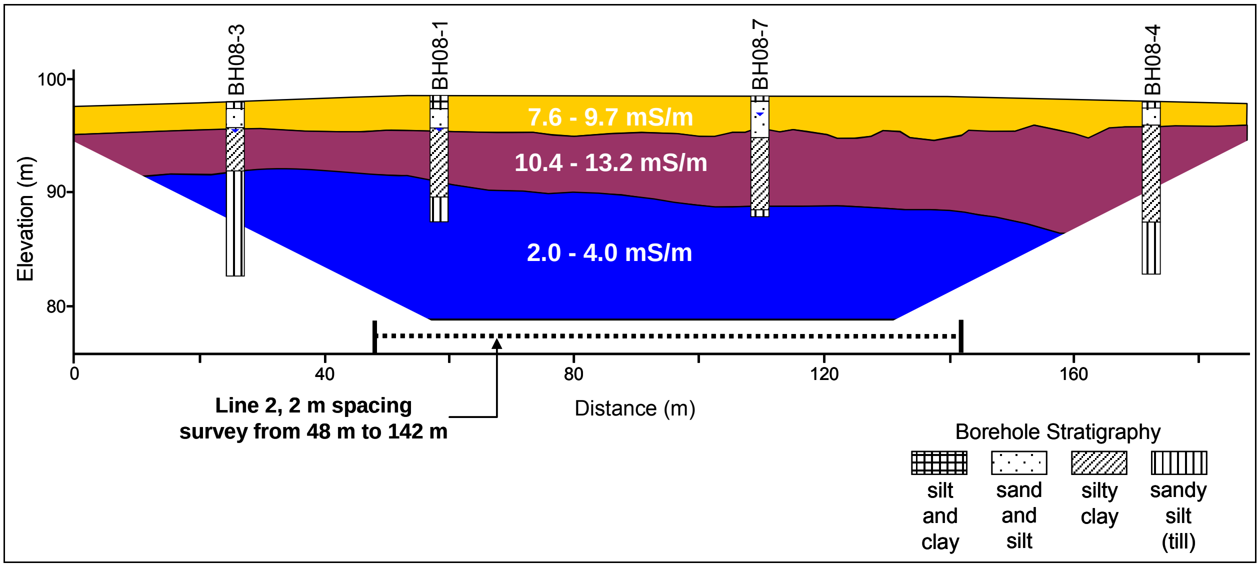

Figure 6.4b: Line 2 ERI cross-section (4-m electrode spacing)

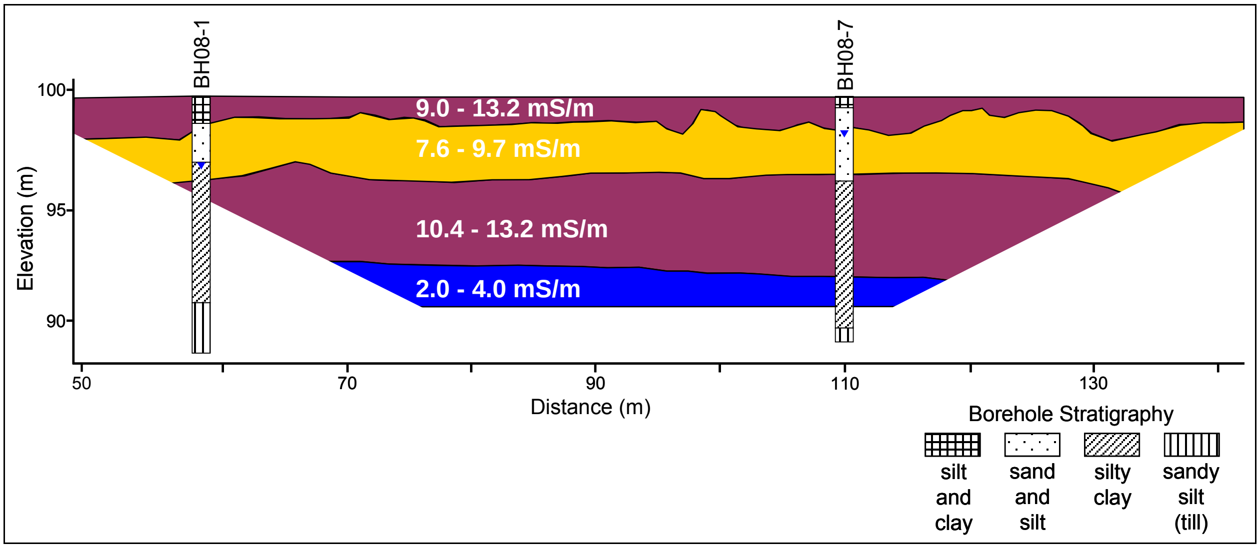

Figure 6.4c: Line 2 ERI cross-section (2-m electrode spacing)

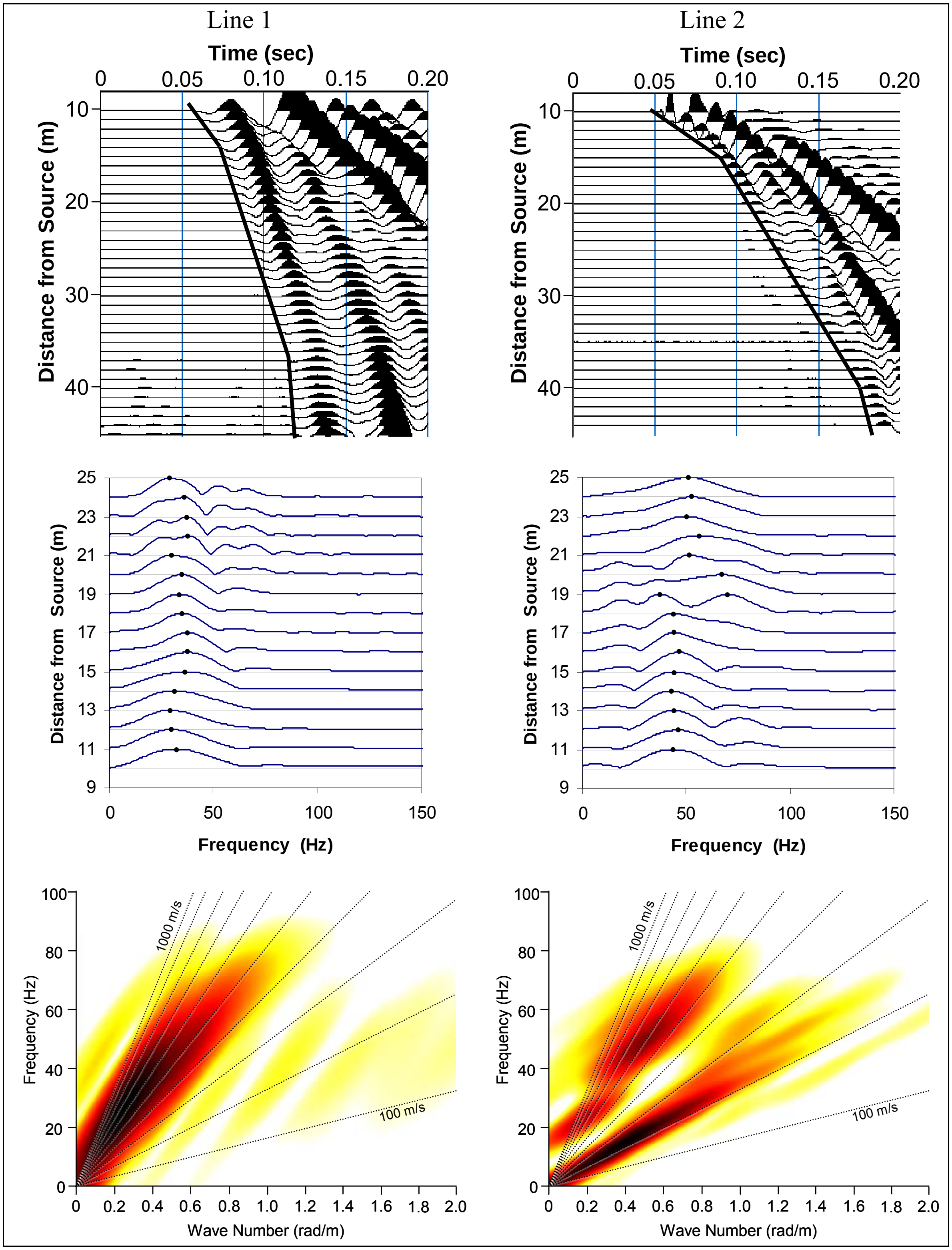

Figure 6.5: Typical time histories, Fourier magnitude spectra, and FK plots from SR survey for both lines (source offset of 10 m)

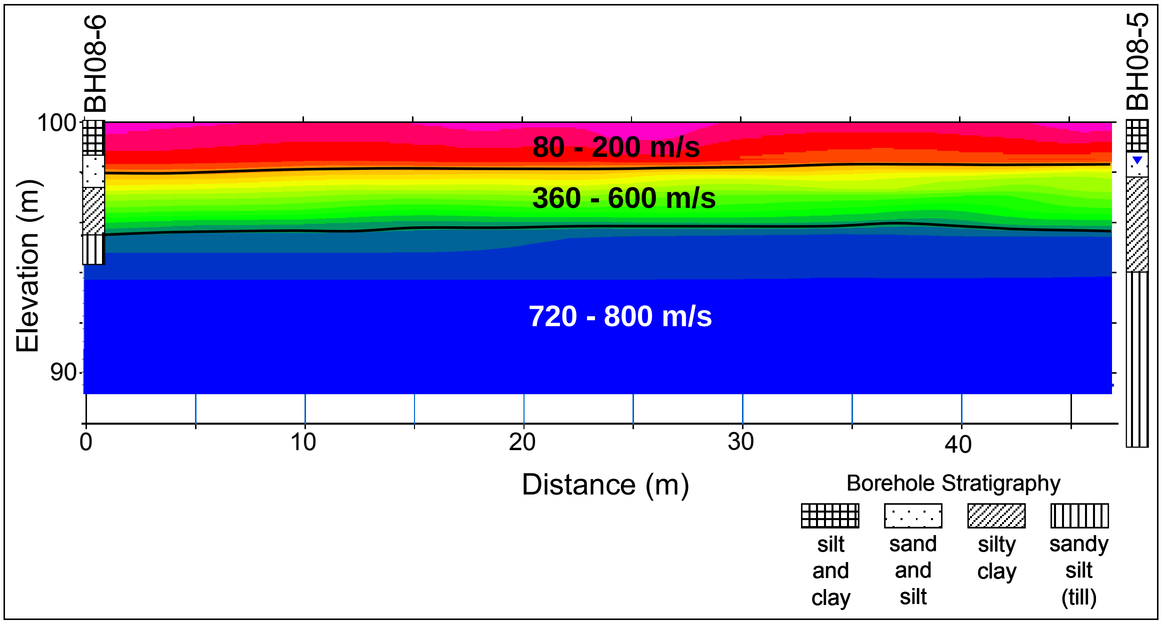

Figure 6.6a: Line 1-1 SR cross-section

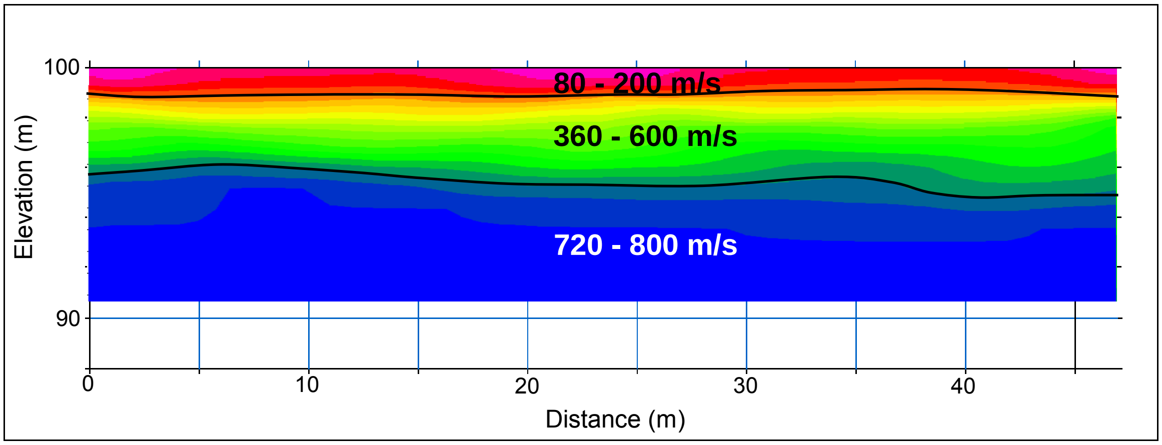

Figure 6.6b: Line 1-2 SR cross-section

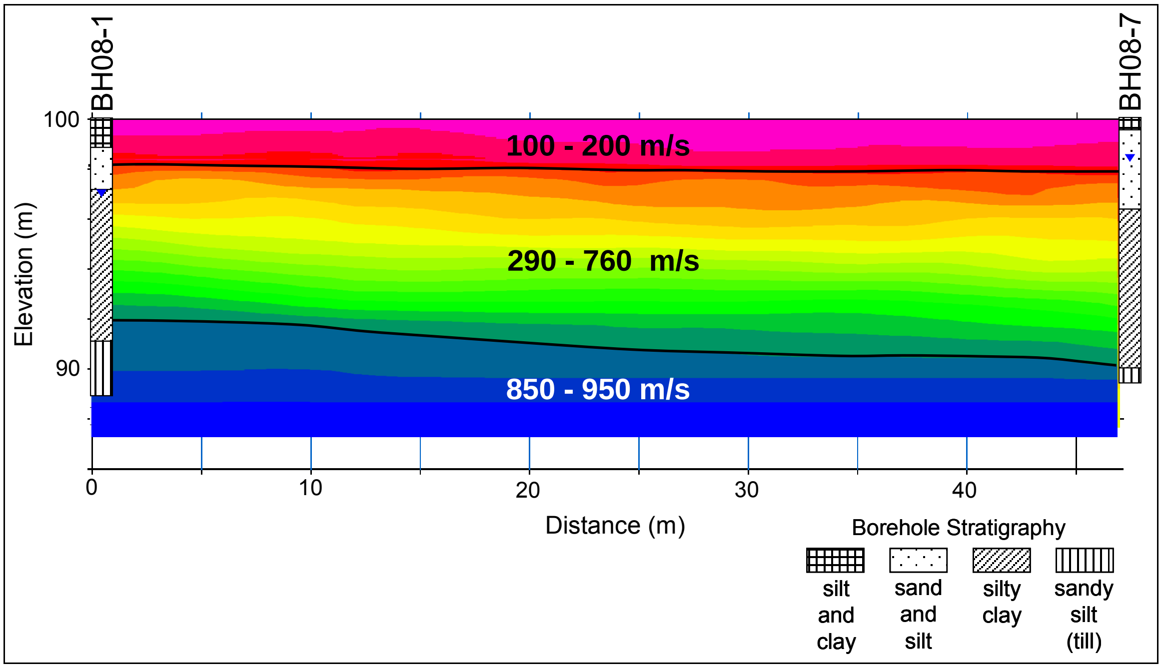

Figure 6.6c: Line 2-1 SR cross-section

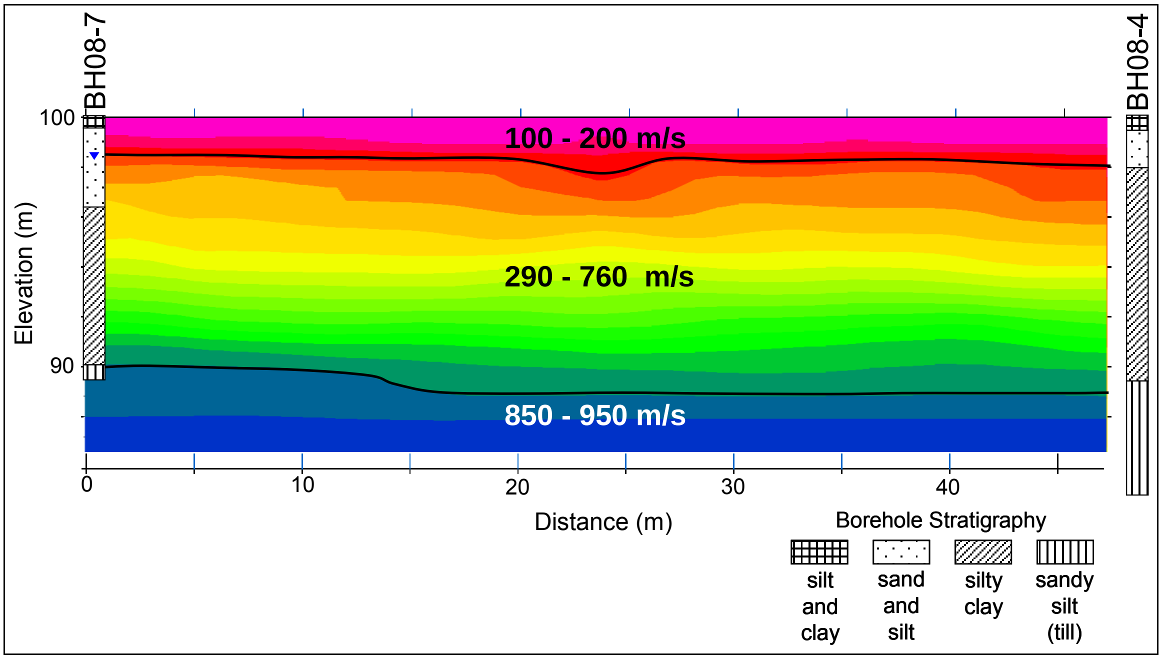

Figure 6.6d: Line 2-2 SR cross-section

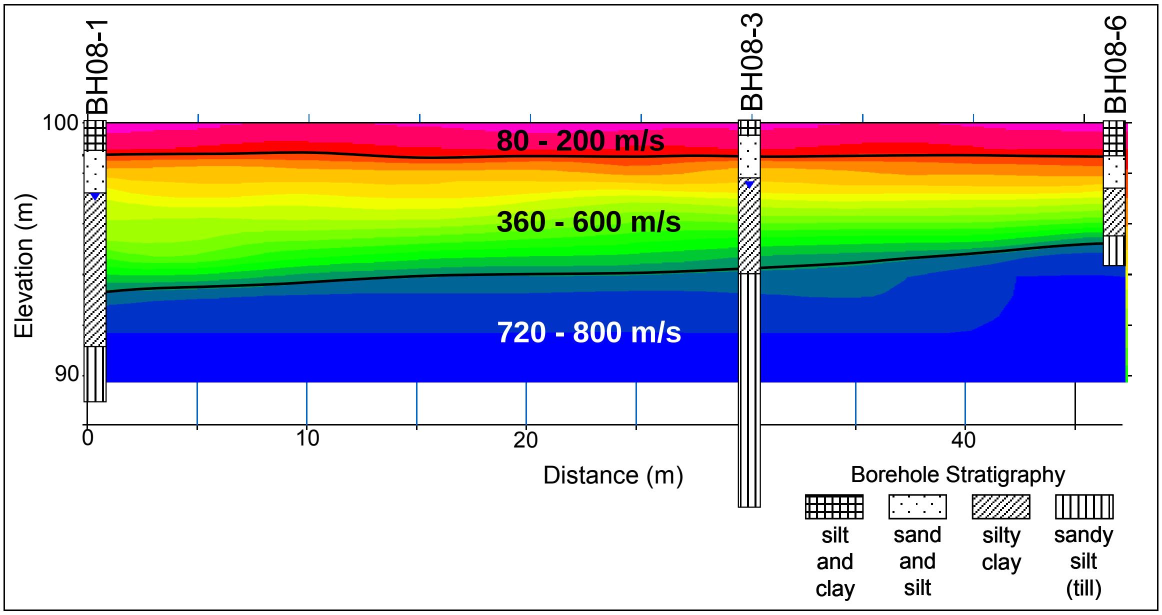

Figure 6.6e: Line 2-3 SR cross-section

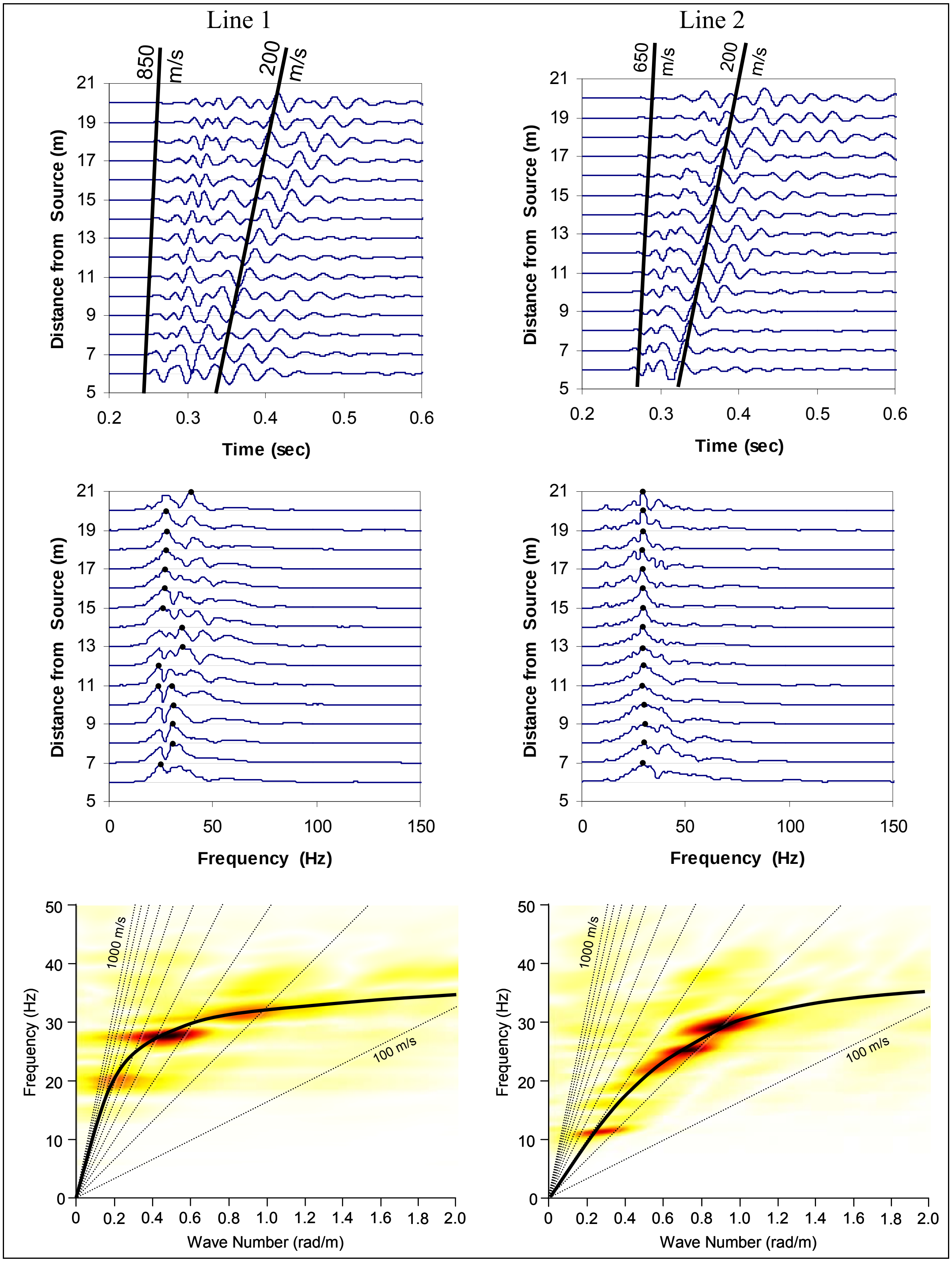

Figure 6.7: Typical time histories, Fourier magnitude spectra, and FK plots from MASW survey for both lines (source offset of 6 m)

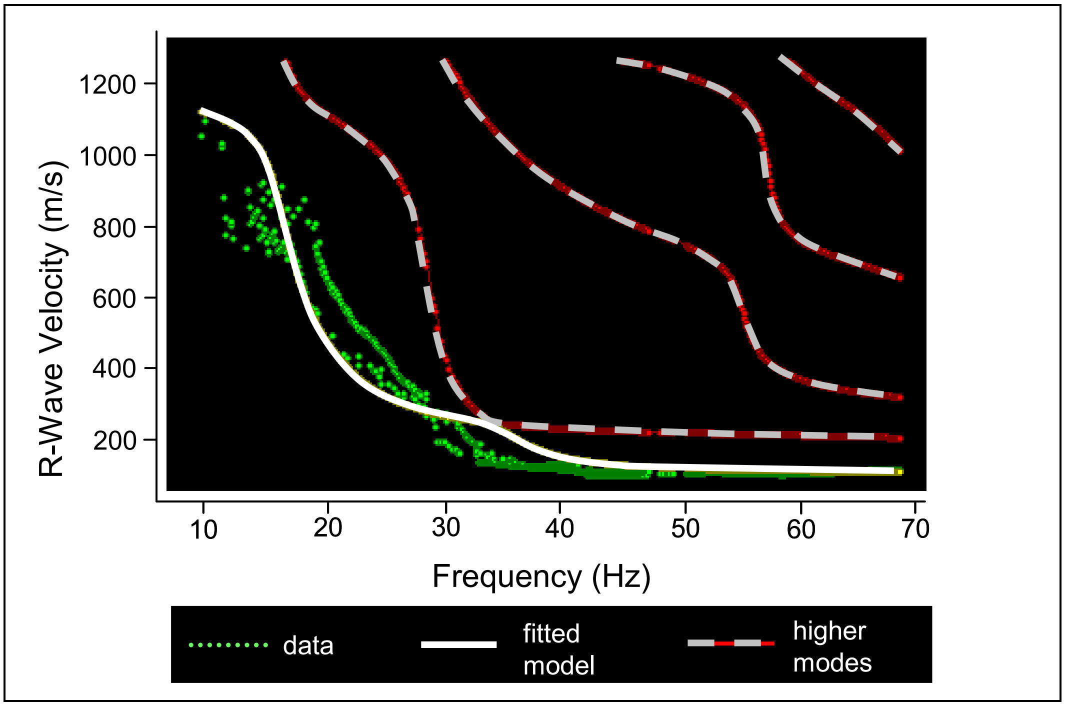

Figure 6.8a: Typical dispersion curve for Line 1 (source offset of 2 m)

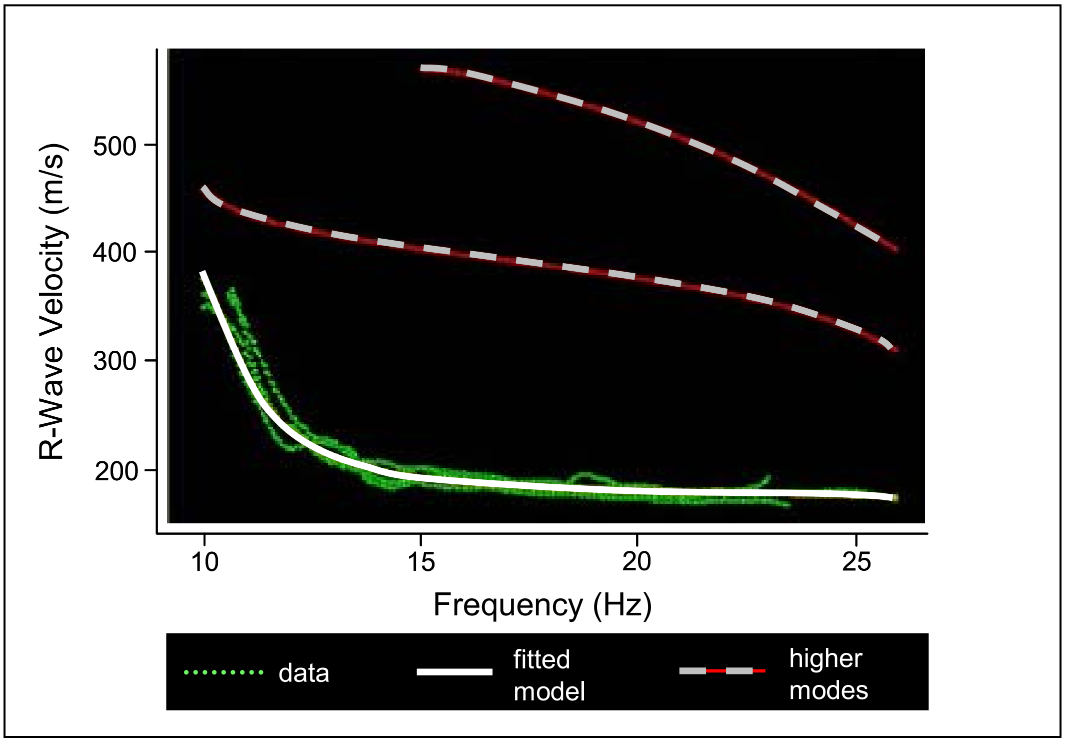

Figure 6.8b: Typical dispersion curve for Line 2 (shots with source offset of 2, 6 and 20 m)

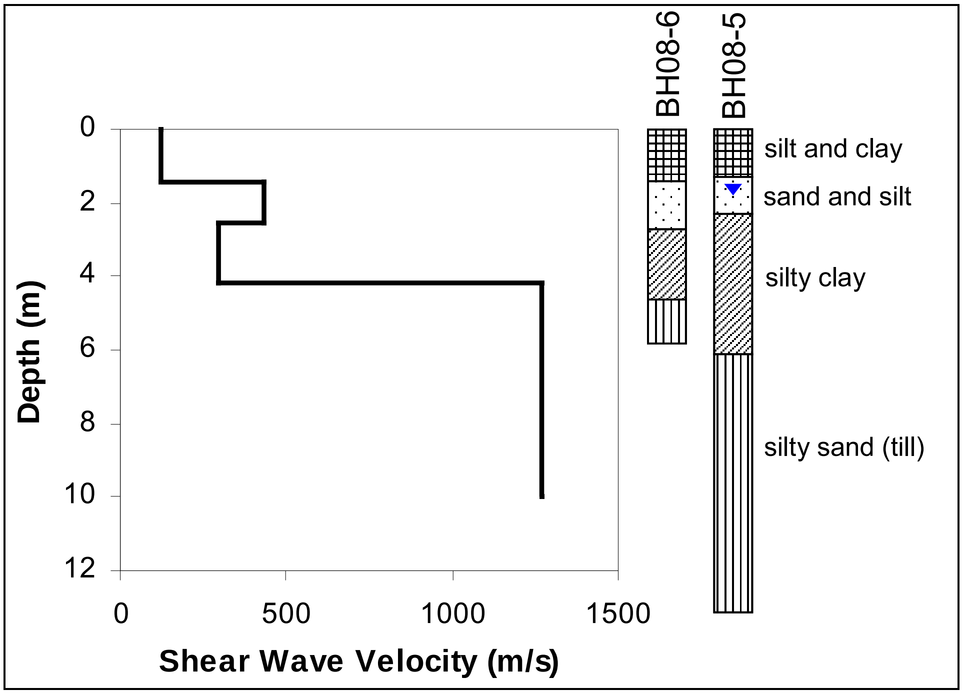

Figure 6.9a: Line 1-1 MASW velocity profile

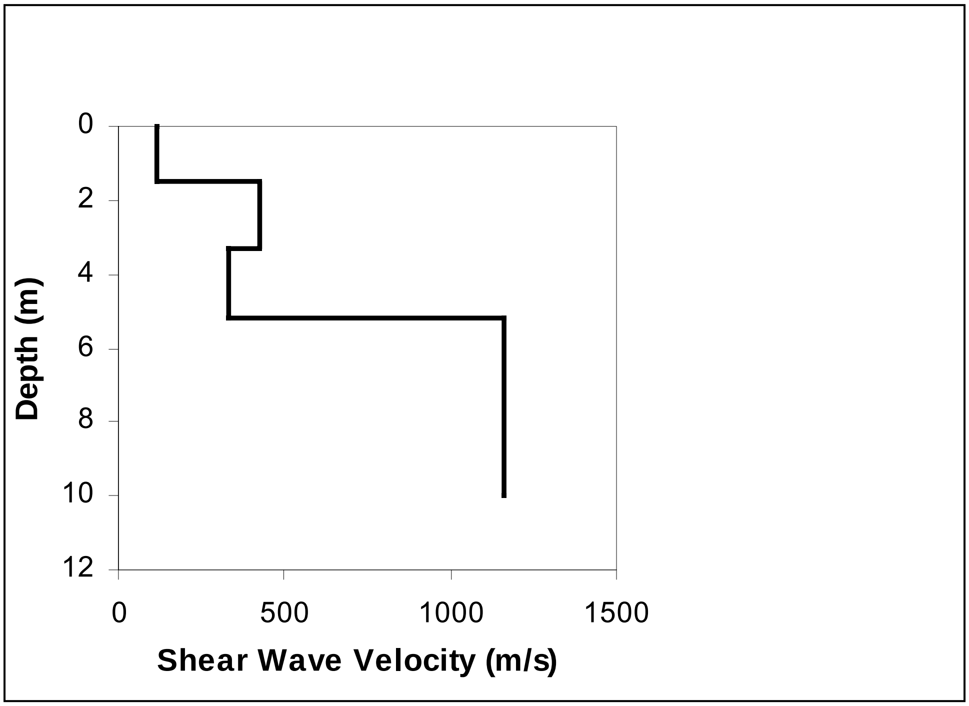

Figure 6.9b: Line 1-2 MASW velocity profile

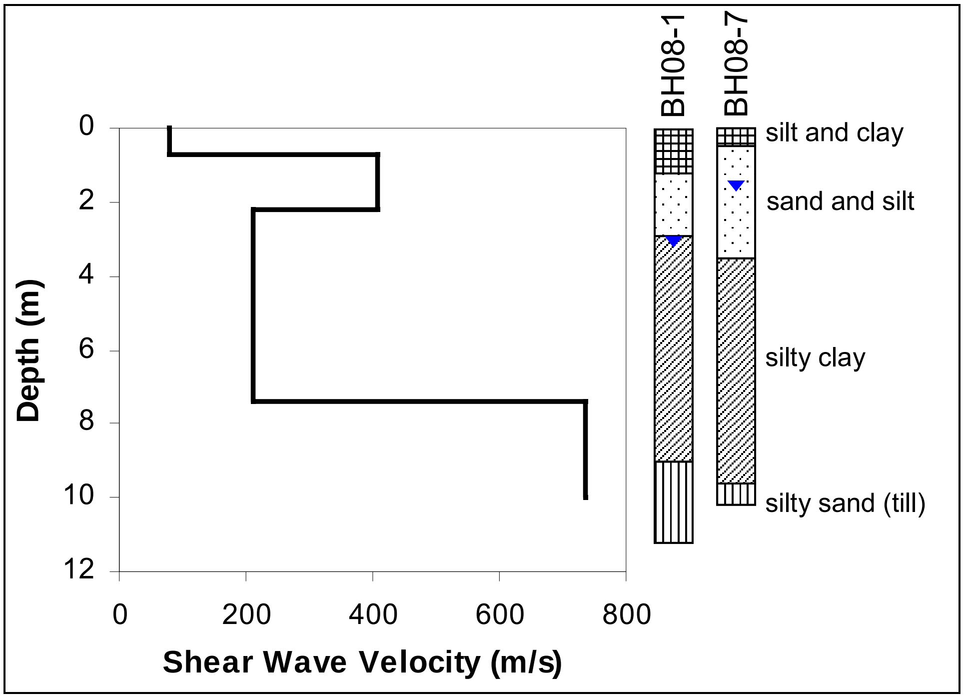

Figure 6.9c: Line 2-1 MASW velocity profile

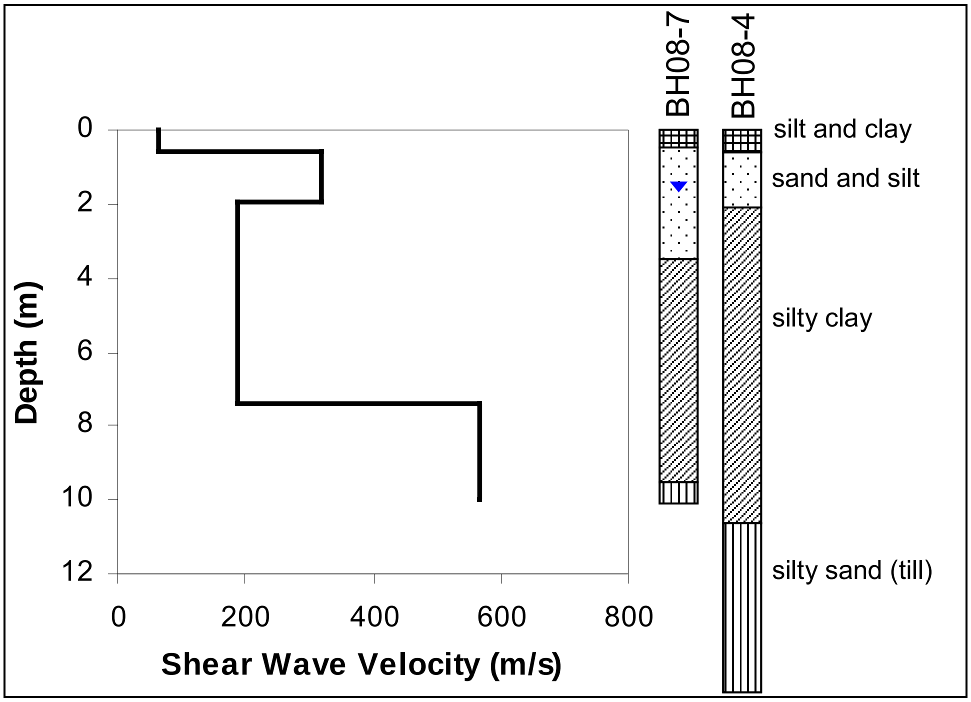

Figure 6.9d: Line 2-2 MASW velocity profile

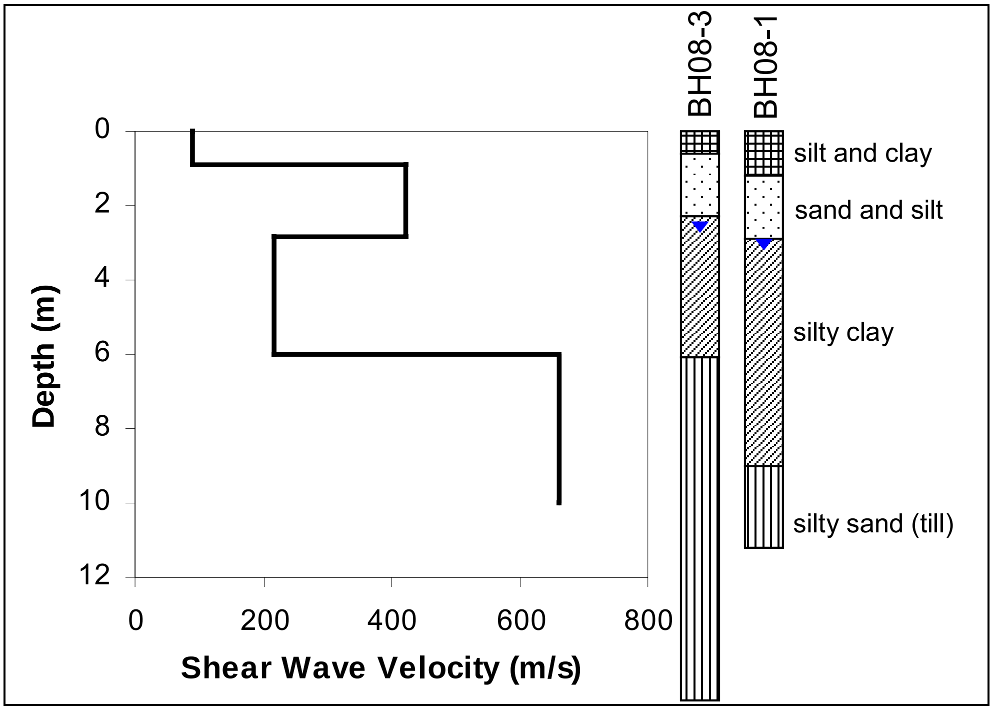

Figure 6.9e: Line 2-3 MASW velocity profile

CHAPTER 7: CONCLUSIONS AND FUTURE WORK

7.1 Conclusions from Ultrasonic Study

This study examines the relationship between the small-strain and large-strain properties of exhumed cast iron water pipes. Non-destructive and destructive testing programs were performed on eight pipes varying in age from 40 to 130 years. Microstructure evaluation showed that three of the pipes were ductile iron and five of the pipes were grey cast iron. Ultrasonic pulse velocity and frequency content area, and tensile and flexural modulus, strength, and elongation were relatively higher in the ductile iron pipes than in the grey cast iron pipes.

The ultrasonic wave velocity measurements on samples from an individual pipe were not well correlated with the corresponding large-strain properties. However, wave velocities were consistently different between ductile and grey cast iron pipes (14% to 18% difference); the ductile iron pipes showed the smaller variation in wave velocities. Thus, the variation of elastic properties for ductile iron was not enough to define a linear correlation because all the measurements were practically concentrated in single cluster of points. It is likely that the changes in microstructure between samples from the same pipe are not significant enough to be detected by the ultrasonic velocity measurements.

This study presents novel analysis of ultrasonic measurements using the Fourier and the wavelet transforms. The Fourier analysis was also unable to show good correlations between low strain and large-strain parameters. Lamb waves are typically not considered in the evaluation of ultrasonic pulse velocities. However, Lamb waves were found to contribute significantly to the frequency content of the ultrasonic signals possibly contributing to the poor correlations. The Daubechies's discrete wavelet transform was used in an attempt to isolate p-wave energy with shorter wavelengths and exclude the high-amplitude Lamb wave energy. The resulting analyses showed slight improvements in the correlations between the wave energy (area of the frequency spectra) and large strain measurements, but in general good correlations were still not observed.

Although previous studies available in the literature show good correlations between ultrasonic velocity and tensile strength in grey cast iron and ductile iron, the specimens used in these studies had regular and consistent geometries where changes in microstructure were carefully controlled through manufacturing processes. Conversely, the specimens from exhumed pipes tested in this study varied in cross-sectional area as a result of minor manufacturing defects and different levels of corrosion. These variations impact the large strain testing results but superficial defects have limited effects on wave velocities and frequency content and may therefore contribute to the low correlations observed throughout this study. Therefore, correlations between wave velocities and large strain properties obtained using carefully manufactured specimens must be used with caution in the condition assessment of aged water pipes especially for grey cast iron pipes.

7.2 Conclusions from Geophysical Study

Three geophysical methods were used to assess their applicability to accurately delineate stratigraphy at a test site: electric resistivity imaging, seismic refraction, and multiple-channel analysis of surface waves. The effectiveness of the geophysical methods was evaluated against subsurface information obtained from drilled boreholes. The boreholes revealed three general layers overlying a glacial till across the site. A stiffness reversal with depth was observed between the second layer from the surface (compact sand) and the layer overlying the till (soft silty clay).

The ERI results were most effective in determining the depth of the till which ranged from 4.6 and 10.7 m across the site. Lab resistivity measurements conducted on samples collected from the field were in agreement with the stratigraphic model inverted from the ERI survey data. However, the resolution of the ERI survey (4-m electrode spacing) was not sufficient to accurately predict the upper strata. Therefore, the use of different electrode spacings is recommended.

The SR results overestimated the depth of the till by up to four m because of the presence of a stiff layer overlying a soft silty clay (i.e. velocity reversal).

The MASW results predicted the depth to till less accurately than the ERI in that the depth to the competent layer was underestimated by up to 3.3 m. Use of a source that generates higher energy in the lower frequency spectrum may help increase the depth resolution for this method. MASW the most effective of the methods tested in detecting the three distinct layers above the till (velocity reversal), even though the accuracy of predicted layer thicknesses varied across the site. Calibration of the geophones used in the MASW survey confirmed accurate measurements in the frequency range of interest. Frequency domain analysis indicated effective penetration depths of the surface waves from about 2 to 10 m.

The complementary use of geophysical techniques was a successful approach in determining the main soil units and the depth to a competent layer (till) at this site. Additional field studies are required in swampy terrain to assess the applicability of these techniques in delineation of the thickness of soft clay layers and the depth to the firm bottom of swamps. While borehole drilling must never be entirely replaced by geophysical techniques in geotechnical site investigations, a combination of borehole drilling supplemented by geophysical investigation may prove to be cost-effective. This approach has the potential to reduce the amount of intrusive investigation, such as the number of boreholes, in swampy terrain and in environmentally sensitive zones.

7.3 Future Work

Testing of additional cast iron pipe sections is recommended to increase the data set for further evaluation of the correlations investigated in the study discussed in this thesis. Only three ductile iron pipes were studied, so correlations for ductile iron would most benefit from additional samples. In future works, machining cast iron test specimens to more consistent geometries, such as removing corrosion and variations in pipe-wall thickness associated with manufacturing defects, is recommended. Removing such defects could potentially reduce the variability in the large-strain testing results and therefore improve correlations with the small strain parameters. In addition, use of higher frequency transducers (5 MHz) is recommended to improve the resolution of the ultrasonic testing. The smaller wavelength energy could potentially capture changes in microstructure between samples from the same pipe and help improve the investigated correlations.

Generation of low frequencies for the MASW testing is a significant limitation observed in the study presented in this thesis and in the literature. Further characterization of different portable seismic sources to improve low frequency content is required. Increasing the overall energy used in the source could potentially help with this problem. For example, a spring loaded weight drop that uses the elastic energy of the spring in addition to gravity could provide a solution. The instruments used for any source would have to remain easily transportable as to not limit the convenience of the MASW testing procedure. Further understanding of the change in frequency and wavelength of seismic energy with depth as it propagates through layered media is recommended. Changes in wavelength with depth are especially important for seismic cone penetration testing as the resolution of such tests can change with changes in wavelength. A technical note addressing this issue is currently being prepared by the author of this thesis.

REFERENCES

Abdel-Megeed, S. M. (1984). Accuracy of correlation coefficient with limited number of points. The Journal of Experimental Education, 52(4), 188 - 191.

Angus, H.T. (1976). Cast Iron: Physical and Engineering Properties. Butterworth & Co. Inc.: Toronto, ON.

ASTM Standard D790 – 07. (2007). Standard Test Methods for Flexural Properties of Unreinforced and Reinforced Plastics and Electrical Insulating Materials. ASTM International, West Conshohocken, PA. DOI: 10.1520/D0790-07. www.astm.org.

ASTM Standard E8/E8M – 08. (2008). Standard Methods for Tension Testing of Metallic Materials. ASTM International, West Conshohocken, PA.
DOI: 10.1520/E0008_E0008M-09. www.astm.org.

Bilgin, O. and Stewart, H. (2009). Pullout resistance characteristics of cast iron pipe. Journal of Transportation Engineering, 135(10), 730 - 735.

Blitz, J. and Simpson, G. (1996). Ultrasonic Methods of Non-destructive Testing. Chapman & Hall: New York, NY.

Bracewell, R. (2007). The Fourier Transform and its Applications. McGraw-Hill: New York, NY.

Ceverny, V., Langer, J. and Psencik, I. 1974. Computation of geometrical spreading of seismic body waves in laterally inhomogeneous media with curved interfaces. Geophysical Journal of the Royal Astronomical Society, 38(1), 9 - 19.

Collins, D. and Alchekh, W. (1995). Ultrasonic non-destructive evaluation of the matrix structure and the graphite shape in cast iron. Journal of Materials Processing Technology, 55(2), 85 - 90.

Conlin, R. M. and Baker, T. J. (1991). Application of fracture mechanics to the failure behavior of buried cast iron mains. Contract Report No. 266, Transport and Road Research Laboratory: London, UK.

Davis, J. R. (ed.). (1996). Cast Irons. ASM International: Materials Park, OH.

Donohoe, S., Long, M., Gavin, K. and O’Connor, P. (2004). The use of multichannel analysis of surface waves in determining G_{max} for soft clay. Geotechnical and Geophysical Site Characterization: Proceedings of the 2nd International Conference, Porto, Portugal, 19-22 September, 551-520.

Fuller, A., Emerson, P. and Sergeant, G. (1990). A report on the effect upon mechanical properties of variation in graphite form in irons having varying amounts of ferrite and pearlite in the matrix structure and the use of nondestructive tests in the assessments of mechanical properties of such irons. Transactions of the American Foundrymen's Society, 88, 21 - 50.

GeoStudy Astier. (2010). SWAN (Surface waves analysis). http://www.geoastier.com.

Geotomo Software. (2009). Res2dinv ver. 3.55 Manual. Geotomo Software, Malaysia. www.geoelectrical.com.

Graff, K. 1991. Wave motion in elastic solids. Dover Publications Inc.: New York, NY.

Hagedoorn, J. 1959. The plus-minus method of interpreting seismic refraction sections. Geophysical Prospecting, 7, 158 - 182.

Hirsch, M., Bentley, L. R. and Dietrich, P. (2008). A comparison of electrical resistivity, ground penetrating radar and seismic refraction results at a river terrace site. Journal of Environmental & Engineering Geophysics, 13(4), 325 - 341.

Karsay, S. I. (1970). Ductile Iron II Engineering Design Properties Applications. Quebec Iron and Titanium Corporation: Sorel, QC.

Keary, P., Brooks, M. and Hill, I. (2002). An Introduction to Geophysical Exploration (3rd ed.). Blackwell Science Ltd: Malden, MA.

Khan, Z., Cascante, G. and El Naggar, M. H. (2010). Measurement of dynamic properties of a cemented sand using ultrasonic waves. Canadian Geotechnical Journal, in print.

Koelble, F. T. (2006). Cast Iron Soil Pipe Fittings Handbook. Cast Iron Soil Pipe Institute: Washington, DC.

Lai, C. G. and Wilmanski, K. (Eds.). (2005). Surface waves in geomechanics: Direct and inverse modeling for soils and rocks. CISM Courses and Lectures No. 481, International Centre for Mechanical Sciences.

Long, M. and Donohue, S. (2007). In situ wave velocity from multichannel analysis of surface waves (MASW) tests at eight Norwegian research sites. Canadian Geotechnical Journal, 44(5), 533 - 544.

Makar, J. M. and Rajani, B. (2000). Gray cast-iron water pipe metallurgy. Journal of Materials in Civil Engineering, 12(3), 245 - 253.

McNeill, J. D. (1980). Electrical conductivity of soils and rocks. Geonics Technical Note TN-5. Geonics Limited: Mississauga, ON.

Menke, W. (1989). Geophysical analysis: Discrete inverse theory. International Geophysics Series. Academic Press: San Diego, CA.

Miller, G. F. and Pursey, H. (1955). On the Partition of Energy between Elastic Waves in a Semi-Infinite Solid. Proceedings of the Royal Society of London. Series A, Mathematical and Physical Sciences, Vol 233, No. 1192, 55 - 69.

Nazarian, S. and Stokoe, K. H.(1984). In situ shear wave velocities from spectral analysis of surface waves, Proc. Of the eight world conf. On earthquake engineering, San Francisco, California, Vol III, July 21 - 28, 31 - 38.

Nettles, S., Jarrett, B. and Cross, E. (2008). Application of surface geophysics for providing a detailed geotechnical assessment of a large resort development site in Anguilla, BWI. 21st Annual Symposium on the Application of Geophysics to Engineering and Environmental Problems (SAGEEP 2008), Marriott Philadelphia Downtown, Philadelphia, Pennsylvania (USA), 6-10 Apr 2008.

Ohide, T., Ohira, G. and Ikawa, K. (1989). Evaluation of mechanical properties of cast iron by ultrasonic velocity. Proceedings Physical Metallurgy of Cast Iron IV, 357 - 382.

Onozawa, M. and Ohira, G. (1989). Evaluation of cast iron structure by ultrasonic frequency analysis. Proceedings of the Fourth International Symposium on the Physical Metallurgy of Cast Iron. Tokyo, Japan, September 4-6, 1989, 363 - 370.

Orlowicz, W., Tupaja, M., Mróza, M. and Guzikb, E. (2010). Evaluation of ductile iron casting material quality using ultrasonic testing. Journal of Materials Processing Technology, 201, 1493 - 1500.

Palmer, D. (1981). The generalized reciprocal method of seismic refraction interpretation. Geophysics, 46(11), 1508 - 1518.

Park, C. B., Miller, R. D. and Xia, J. (1999). Multichannel analysis of surface waves. Geophysics, 64(3), 800 - 808.

Penumada, D. and Park, C. B. (2005). Multichannel Analysis of Surface Wave (MASW) method for geotechnical site investigation. Geotechnical Special Publication, no. 130-142, 957 - 966.

Piggott, S. (1999). Saturation history effects on the electrical properties of Ottawa sand during water-air and eater-LNAPL drainage-inhibition experiments. Master's Thesis. Earth Science Department, University of Waterloo: Waterloo, ON.

Rajani, B. (2000). Investigation of gray cast iron water mains to develop a methodology for estimating service life. Report No. 280, American Water Works Association Research Foundation: Denver, CO.

Redpath, B. B. (1973). Seismic refraction exploration for engineering site investigations. Technical Report E-73-4, U.S. Army Corps of Engineers, Waterways Experiment Station: Vicksburg, MS.

Santamarina, J. C., Rinaldi, V. A., Fratta, D., Klein, K. A., Wang, Y.-H., Cho, G.-C. and Cascante, G. (2005). A survey of elastic and electromagnetic properties of near-surface soils, Near-Surface Geophysics, Ed. D. Buttler, SEG, Tulsa, OK, USA. 71-87.

Seica, M. V. and Packer, J. A. (2004). Mechanical properties and strength of aged cast iron water pipes. Journal of Materials in Civil Engineering, 16(1), 69 - 77.

Sharma, P. (1997). Environmental and Engineering Geophysics. Cambridge University Press: New York, NY.

Skabo, R. and Jackson, R. (1991). Nondestructive testing of water mains for physical integrity. CH2M Hill Technical Report: USA.

Stokoe II, K. H. and Nazarian, S. (1983). Effectiveness of ground improvement from spectral analysis of surface waves. In Proceedings of the 8th European conference on Soil Mechanics and Foundation Engineering: Improvement of Ground, Rathmayer, H. G., and Saari, K. H. O. (eds), Helsinki, Finland, 1 - 94.

Tamburelli, C. and Quaroni, A. (1975). Ultrasonic velocity measurement to inspect malleable iron castings. Non-Destructive Testing, 8(3), 152 - 157.

Tomeh, A. A., Alyateem, S., Malik, H. and Malone, B. (2006). Geophysical surveying and data simulation application to geotechnical investigations – a cost effective approach for developing economical foundation engineering design criteria. GeoCongress 2006: Geotechnical Engineering in the Information Technology Age, vol. 2006.

Victorov, I. A. (1967). Rayleigh and Lamb Waves. Plenum Press: New York, NY.

Walton, C. F. (1971). Gray and Ductile Iron Casting Handbook. Gray and Ductile Iron Founders' Society Inc.: Cleveland, OH.

Yang, Y, Cascante, G., and Polak, M. A. (2009). Depth detection of surface-breaking cracks in concrete plates using fundamental Lamb modes. NDT&E International, 42(6), 501 - 512.

Zonge, K., Wynn, J., and Urquhart, S. (2005). Resistivity, induced polarization, and complex resistivity. Near-Surface Geophysics, Ed. D. Buttler, Society of Exploration Geophysics, Tulsa, OK, USA. 265 - 300.